

DETERMINATION OF THE HELIUM-6 NUCLEAR CHARGE RADIUS USING
HIGH-RESOLUTION LASER SPECTROSCOPY

BY

LI-BANG WANG

B.S., National Taiwan University, 1996

DISSERTATION

Submitted in partial fulfillment of the requirements
for the degree of Doctor of Philosophy in Physics
in the Graduate College of the
University of Illinois at Urbana-Champaign, 2004

Urbana, Illinois

DETERMINATION OF THE HELIUM-6 NUCLEAR CHARGE RADIUS USING HIGH-RESOLUTION LASER SPECTROSCOPY

Li-Bang Wang, Ph.D.
Department of Physics
University of Illinois at Urbana-Champaign, 2004
Roy J. Holt, Advisor

The charge radius of the neutron-rich ${}^6\text{He}$ ($t_{1/2} = 807$ ms) nucleus was determined to a precision of 0.7% in a laser spectroscopic measurement at Argonne National Laboratory. The ${}^6\text{He}$ atoms were produced *via* the ${}^{12}\text{C}({}^7\text{Li}, {}^6\text{He}){}^{13}\text{N}$ reaction at the Argonne Tandem Linac Accelerator System (ATLAS), and were excited to the metastable states by an RF-driven discharge. The spectroscopy was performed on individual ${}^6\text{He}$ atoms confined and cooled in a magneto-optical trap. The isotope shift between ${}^6\text{He}$ and ${}^4\text{He}$ on the $2^3\text{S}_1-3^3\text{P}_2$ transition at 389 nm was measured to be 43194.772 ± 0.056 MHz. Based on this measurement and the atomic theory calculation, the root-mean-square charge radius of ${}^6\text{He}$ was determined to be 2.054 ± 0.014 fm. Combined with the interaction radius from scattering experiments, the neutron-halo structure of the ${}^6\text{He}$ nucleus was confirmed model-independently for the first time. This measurement helps reveal the three-nucleon forces inside the nucleus, and the result agrees well with the *ab initio* quantum Monte Carlo calculations using a modern nuclear potential. The result is also compared with values predicted by various cluster models.

Acknowledgement

The results of my three years of research at Argonne National Laboratory are presented in this dissertation. This project would not have been successful without the dedicated support of many people.

First, I would like to thank Dr. Zheng-Tian Lu, who has been essential to my development as a physicist. I benefited a lot through his guidance with enthusiasm and creativity. He has always been able to explain complicated physical problems using simplified concepts, and helped me make sense of many puzzles.

I gratefully appreciated the support of my advisor, Professor Roy Holt, who provided me the great opportunity to work for the APV experiment at UIUC and the ${}^6\text{He}$ project at Argonne. His sincere attitude and great knowledge in physics makes him an excellent teacher and I have learned a lot of nuclear physics from him.

I was fortunate to work with Dr. Peter Mueller. He was a great resource for me in the laboratory. I am thankful for his enthusiasm and willingness to share his knowledge. The everyday collaboration in the lab has been enjoyable. I also want to express my thanks for the excellent technical support from Tom O'Connor and Kevin Bailey. Without them, the project would have been three times more difficult to complete.

I want to acknowledge all the members of the ${}^6\text{He}$ collaboration, especially the heavy ion group at ATLAS for providing the ${}^6\text{He}$ source and Professor Gordon Drake for the theoretical support. Special thanks also go to Robert Wiringa, Steve Pieper and

Henning Esbensen in the theory group. They have helped clarify many theoretical concepts. I also extend my thanks to former ATTA members, Xu Du and Iain Moore, and the entire MEP group for their constant concerns for the experimental progress and Elaine Schulte for carefully reviewing the manuscript of this thesis.

Finally, I would like to say thank you to my parents for their spiritual support and my fiancée Hsin-Lan, who always stands by me and encourages me. I also want to thank my sisters and all my friends who have enriched my life.

This work was supported by the U.S. Department of Energy, Office of Nuclear Physics, under Contract No. W-31-109-ENG-38.

Table of Contents

Chapter 1 Nuclear Charge Radii and Nuclear Models	1
1.1 Two-Nucleon Potential	2
1.2 Three-Nucleon Forces.....	5
1.3 Quantum Monte Carlo Calculation of Light Nuclei	8
1.4 Neutron-Rich ${}^6\text{He}$ and Cluster Models	10
Chapter 2 Methods for Measuring Nuclear Charge Radii.....	13
2.1 Electron Scattering.....	14
2.2 Nuclear Reaction Cross Section and Elastic Proton Scattering	16
2.3 Muonic Atom X-Ray Spectroscopy.....	18
2.4 Atomic Isotope Shift.....	20
Chapter 3 Atomic Isotope Shift and Nuclear Charge Radii	22
3.1 Mass Shift	23
3.2 Field Shift.....	24
3.3 Atomic Theory of Helium.....	27
Chapter 4 Production of ${}^6\text{He}$	31
4.1 Nuclear Properties of ${}^6\text{He}$	31
4.2 Production of ${}^6\text{He}$	33

Chapter 5 Laser Cooling and Trapping of Metastable Helium	36
5.1 Atomic Beam of Metastable Helium	37
5.2 Vacuum System and Gas Recirculation.....	39
5.3 Transverse Cooling of an Atomic Beam.....	41
5.4 Deceleration of an Atomic Beam.....	43
5.5 Magneto-Optical Trap.....	45
5.6 Detection of Trapped Atoms.....	47
Chapter 6 Laser Spectroscopy of Trapped Atoms.....	50
6.1 Laser Induced Fluorescence Detection	51
6.2 Single Atom Detection.....	52
6.3 Light Shift and Zeeman Shift.....	54
6.4 Motional Effect of Trapped Atoms.....	57
6.5 Determination of the Resonance Line Center	59
Chapter 7 Laser System and Data Acquisition.....	61
7.1 Laser Setup for Trapping and Cooling at 1083 nm.....	62
7.2 Laser Setup for Precision Spectroscopy at 389 nm	66
7.3 Chopping and Switching the Laser Light	70
7.4 Frequency Scan and Data Acquisition	71
Chapter 8 Systematic Error Study	75
8.1 Fine Structure Splitting Measurement of ^4He in the Trap	76
8.2 Fine Structure Splitting Measurement of ^4He in the Atomic Beam.....	80

8.3	Isotope Shift Measurement of ^3He	86
8.4	Systematic Uncertainty Summary.....	89
Chapter 9 Results and Discussion		90
9.1	Single ^6He Atom Detection.....	91
9.2	Analysis of the Resonance Line Shape.....	93
9.3	Determination of ^4He - ^6He Isotope Shift	94
9.4	Point-Proton Radius of ^6He and Comparison with Theories	96
9.5	Darwin-Foldy Correction of the Proton Radius.....	99
9.6	Neutron-Halo Structure.....	103
9.7	Nuclear-Structure Correction.....	104
9.8	Meson-Exchange-Current Correction.....	106
Chapter 10 Conclusion and Outlook		108
10.1	Conclusion.....	109
10.2	Outlook	110
Appendix A Helium Energy Levels		113
Appendix B Laser Cooling and Trapping of Neutral Atoms		115
B.1	Basic Concepts.....	115
B.2	Transverse Cooling.....	117
B.3	Zeeman Slowing	118
B.4	Magneto-Optical Trap.....	120
Appendix C Frequency Doubling Using a Nonlinear Crystal....		122

Appendix D Frequency-Modulation Spectroscopy	124
D.1 Basic Concepts	124
D.2 Iodine Spectroscopy	125
References	128
Vita	135

List of Figures

Figure 1.1: The OPEP and TPEP	3
Figure 1.2: Three-nucleon forces	5
Figure 1.3: GFMC of the binding energy of light nuclei	9
Figure 1.4: Correlation between the two valence neutrons	10
Figure 1.5: Different coordinates for the α -n-n and triton-triton clusters	11
Figure 2.1: Root-mean-square matter radii of He, Li, Na and Be isotopes	17
Figure 2.2: Muonic helium ion energy level	19
Figure 3.1: High precision measurements of helium and their interpretation	30
Figure 4.1: Target design and the detection chamber	34
Figure 4.2: ${}^6\text{He}$ identification	35
Figure 5.1: Schematic of the RF resonator and the LN_2 cooling	37
Figure 5.2: Helium energy level diagram	38
Figure 5.3: Fluorescence signal of the atomic beam with and without LN_2 cooling	38
Figure 5.4: Schematic diagram of the atomic beam line and vacuum system	39
Figure 5.5: Zigzag configuration of the transverse cooling laser light	42
Figure 5.6: Atomic beam fluorescence in the trap chamber	43
Figure 5.7: Magnetic field of the Zeeman slower as a function of position	44
Figure 5.8: Three-dimensional MOT	45
Figure 5.9: MOT magnetic field profile along the vertical and radial direction	46
Figure 5.10: Decay of the trapped atoms due to collisions	49
Figure 6.1: Imaging system for single atom detection	51

Figure 6.2: Single atom signal of ^4He	53
Figure 6.3: Illustration of the light shift.....	55
Figure 6.4: Sequence and timing of the chopping and detection gates.....	56
Figure 6.5: Trap fluorescence for different blue laser power	57
Figure 6.6: Frequency scan from red to blue and blue to red side of the resonance.....	59
Figure 6.7: Decrease of the linewidth by using weak probe laser power	60
Figure 7.1: The 1083 nm laser frequency lock and control system	63
Figure 7.2: Saturation absorption peak in the discharge gas cell.....	64
Figure 7.3: Distribution of the laser power	65
Figure 7.4: The 389 nm laser system	67
Figure 7.5: Iodine spectrum near 777.946 nm	68
Figure 7.6: Relative frequency position of the iodine line and the helium isotopes.....	69
Figure 7.7: Timing of the VCO scanning and photo counting	72
Figure 7.8: Synchronization of the data acquisition	73
Figure 8.1: Results of the fine structure splittings for different laser power	78
Figure 8.2: Results of the fine structure splittings for different MOT currents.....	78
Figure 8.3: Fine structure splitting measurement with a linear fit.....	79
Figure 8.4: Production of the metastable helium beam and the detection scheme	82
Figure 8.5: Line center determination of the helium transition	84
Figure 8.6: Results of the fine structure intervals	85
Figure 8.7: Energy level diagram of ^4He and ^3He	87
Figure 9.1: Fluorescence signal of a single trapped ^6He atom.....	91
Figure 9.2: Trap loading rate vs. MOT laser detuning frequency.....	92
Figure 9.3: The ^4He and ^6He spectra.....	93
Figure 9.4: Determination of the isotope shift	94

Figure 9.5: Contribution to the total charge radius due to the proton size.....	97
Figure 9.6: Comparison of ${}^6\text{He}$ charge radius between experiments and theories	98
Figure 9.7: Difference in the mean-square charge radius between ${}^6\text{He}$ and ${}^4\text{He}$	102
Figure 10.1: Relative frequency position of ${}^4\text{He}$, ${}^6\text{He}$, ${}^8\text{He}$ and iodine transitions.....	111
Figure A.1: Energy level diagram of singlet and triplet states of helium.....	114
Figure B.1: Optical pumping of the slowing light	119
Figure B.2: Energy level diagram in the presence of magnetic field.....	120
Figure B.3: Position and velocity dependence of the trap force.....	121
Figure C.1: Geometry of the doubling ring cavity.....	123
Figure D.1: Schematic diagram of the iodine saturation spectroscopy.....	126
Figure D.2: Line shape of the iodine spectrum.....	127

List of Tables

Table 1.1: Ground state properties of the deuteron.....	5
Table 2.1: Theoretical calculation and experimental results of nuclear charge radii	21
Table 3.1: Contributions for the helium energy level.....	29
Table 4.1: Comparison of half-life and ft value between neutron and ${}^6\text{He}$ decay	33
Table 4.2: Cross section of (${}^7\text{Li}$, ${}^6\text{He}$) reaction for various targets.....	33
Table 5.1: Characteristics of the Zeeman slower.....	44
Table 7.1: Summary of the 1083 nm and 389 nm laser systems	71
Table 8.1: Results of various fine structure interval measurements	80
Table 8.2: Result of the fine structure intervals by this work.....	85
Table 8.3: Comparison of the ${}^{3,4}\text{He}$ isotope shift in the absence of HFS.....	89
Table 8.4: Summary of the systematic uncertainties	89
Table 9.1: Summary of the isotope shift with uncertainties	95
Table 9.2: Summary of uncertainties of the measured ${}^6\text{He}$ charge radius	95
Table 9.3: The ${}^6\text{He}$ nuclear charge radius (in fm).....	98
Table 9.4: Difference in ms nuclear charge radius between ${}^6\text{He}$ and ${}^4\text{He}$	102
Table 9.5: Summary of various parameters for the proton and neutron distribution.....	104

Chapter 1

Nuclear Charge Radii and Nuclear Models

It is well established that the fundamental theory of the strong interaction is quantum chromodynamics (QCD). Thus, quarks and gluons form the correct basis for describing nuclei. However, it is too difficult to perform QCD calculations in the non-perturbative regime, for example, to describe the nuclear structure. Rather, in low- and medium-energy nuclear physics, an effective theory based on nucleon-meson degrees of freedom is used. Models are developed based on the Yukawa interaction between two nucleons, and the differential cross sections for nucleon-nucleon (NN) scattering from the experimental results are used to constrain the parameters in these models.

Because models that ignore quark and gluon degrees of freedom or neglect isobars do not have a correct basis, new forces such as the three-nucleon potential become necessary to describe observed phenomena. The evidence of the three-nucleon forces can be identified using three-nucleon scattering reactions. Due to the differences in the two-nucleon potentials, and the uncertainties in the three-nucleon calculations, it is very difficult to extract the three-nucleon effects. The cleanest signature of the three-nucleon force is the binding energies of light nuclei. The binding energies of light nuclei have been used to constrain parameters of the three-nucleon force, while the radii of those nuclei serve as a complementary check of the models.

Due to the isospin dependence of the three-nucleon forces, the neutron-rich nuclei, for example, ${}^6\text{He}$ and ${}^8\text{He}$ provide the best testing ground for the isospin 3/2 channel of the three-nucleon force, which is absent in the s -shell nuclei. Therefore, the measurement of the ${}^6\text{He}$ charge radius will set stringent constraints on the three-nucleon force, which is crucial for the neutron star calculations.

1.1 Two-Nucleon Potential

Rather than starting from the quark degrees of freedom using QCD, most modern and successful nuclear models describe the strong interactions by meson exchange between the nucleons, which are treated as structureless point particles. The concept of meson exchange was first proposed by Hideki Yukawa [Yukawa, 1935], and the potential generated by the exchange of spinless mesons with mass m has the form:

$$V(r) = \frac{g}{4\pi} \frac{e^{-mr}}{r}, \quad (1.1)$$

where r is the distance between the two nucleons, and g is the coupling constant. Here the natural units, $\hbar = c = 1$, are used. The force is attractive, and the range of the potential can be estimated by the mass of the mediating pions: $r \sim (m_\pi)^{-1} = (140 \text{ MeV})^{-1} = 1.4 \text{ fm}$. A more complete description of the one-pion-exchange potential (OPEP) including the spin and isospin effects can be written as

$$V_{OPEP} = \frac{f^2}{4\pi} \frac{m_\pi}{3} (\boldsymbol{\tau}_1 \cdot \boldsymbol{\tau}_2) \left\{ \boldsymbol{\sigma}_1 \cdot \boldsymbol{\sigma}_2 + S_{12} \left[1 + \frac{3}{m_\pi r} + \frac{3}{(m_\pi r)^2} \right] \right\} \frac{e^{-m_\pi r}}{m_\pi r}, \quad (1.2)$$

where $\boldsymbol{\tau}$ and $\boldsymbol{\sigma}$ are the isospin and spin of the nucleons, and f^2 is the coupling constant. The quantity, $S_{12} = 3(\boldsymbol{\sigma}_1 \cdot \hat{r})(\boldsymbol{\sigma}_2 \cdot \hat{r}) - \boldsymbol{\sigma}_1 \cdot \boldsymbol{\sigma}_2$, is the tensor operator resulting in a non-

central potential. The spin dependence of the nuclear force comes through the spin-spin interaction $\sigma_1 \cdot \sigma_2$, and the tensor operator S_{12} , while the isospin dependence arising from the difference between protons and neutrons is in the $\tau_1 \cdot \tau_2$ term.

A more detailed picture of nuclear forces also includes the interactions at short and intermediate distance. At short distance a repulsive force exists due to the Pauli exclusion principle between the quarks. This is responsible for the density saturation of the nuclear matter, and is usually described phenomenologically. At intermediate distance (~ 1 fm), it is straightforward to include heavier meson exchange, for example ρ -meson ($m_\rho = 770$ MeV, decays into 2π), and ω -meson ($m_\omega = 780$ MeV, decays into 3π). Therefore, OPEP can then be generalized to a One Boson Exchange Potential (OBEP). Another approach is to consider higher order contributions. The Two Pion Exchange Potential (TPEP) is illustrated in Figure 1.1. The range of the TPEP is shorter than that of the OPEP and is of the order $(2m_\pi)^{-1} = 0.7$ fm.

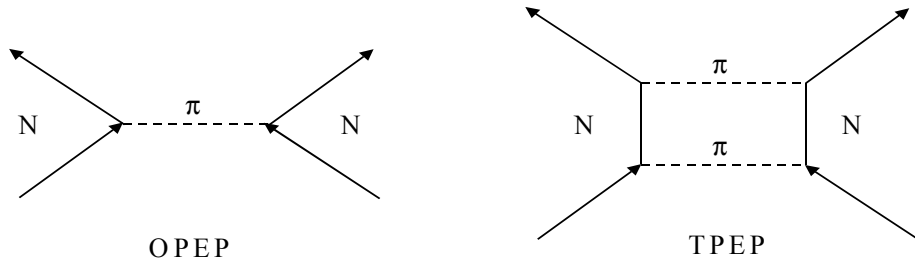


Figure 1.1: The OPEP and TPEP. Other loop diagrams also contribute to the TPEP and are not shown in this diagram.

Various modern two-nucleon potentials have been developed. Examples include Argonne v_{18} [Wiringa, 1995], CD-Bonn [Machleidt, 1996], Reid 93, and Nijmegen II

[Stoks, 1994]. All the models produce the long-range attraction by OPEP. At short and intermediate ranges, however, these models are quite different, ranging from OBEP, TPEP to purely phenomenological treatments. A complete discussion of the modern nuclear potentials has been published by Carlson and Schiavilla [Carlson, 1998]. In the case of Argonne v_{18} (AV18), for example, the potential contains the electromagnetic interactions, the intermediate-range TPEP, and the short-range phenomenological term in addition to the long-range OPEP. The two-nucleon potential can then be written as

$$v_{ij} = v_{ij}^{\gamma} + v_{ij}^{\pi} + v_{ij}^R, \quad (1.3)$$

where v^{γ} represents the electromagnetic interactions including one- and two-photon exchange, vacuum polarization, and magnetic moment interactions with appropriate electric and magnetic form factors of protons and neutrons. The quantity v^{π} is the OPEP given by Eq. 1.2, and includes the charge-dependent (CD) terms to account for the difference in masses between π^{\pm} and π^0 . The final term, v^R , includes the short-range repulsive force and the TPEP. The Woods-Saxon function $W(r) = [1 + e^{(r-r_0)/a}]^{-1}$ is used to represent the hard-core effect with the shape parameters a and r_0 . The TPEP has the form of $\frac{e^{-2m_{\pi}r}}{r^2}$, and represents the attraction force at intermediate range. Furthermore, a cutoff function is used in both OPEP and TPEP so that the two terms vanish at $r = 0$. There are a total of 18 operators with 40 free parameters used to fit thousands of NN scattering data.

The ground state properties of the deuteron are obtained by various models as shown in Table 1.1. The differences between the models are small, and the comparisons

with the experiments are in reasonable agreement. Note the binding energy has already been fit by parameterizing the models.

Table 1.1: Ground state properties of the deuteron as summarized in [Carlson, 1998].

	Experiment	AV18	Nijm II	Reid 93	CD Bonn	units
Point-nucleon radius	1.971(5)	1.967	1.9675	1.9686	1.966	fm
Magnetic moment	0.857406(1)	0.847				μ_N
Quadrupole moment	0.2859(3)	0.270	0.271	0.270	0.270	e-fm ²
D/S state ratio	0.0256(4)	0.0250	0.0252	0.0251	0.0255	

1.2 Three-Nucleon Forces

It was soon realized that with a two-nucleon potential alone, nuclear properties cannot be described correctly in nuclei with $A > 2$. For example, the binding energy of the triton is underestimated in the calculation by Friar *et al.* [Friar, 1993] using AV18, Nijmegen II, and Reid 93 models. Different models give similar results of 7.62(1) MeV, while the experimental result is 8.48 MeV. With the two-nucleon potential alone, the neutron-rich nuclei, ${}^6\text{He}$ and ${}^8\text{He}$ are not bound. In fact all the two-nucleon potentials underbind most of the light nuclei. This failure comes from the fact that the nucleons are actually

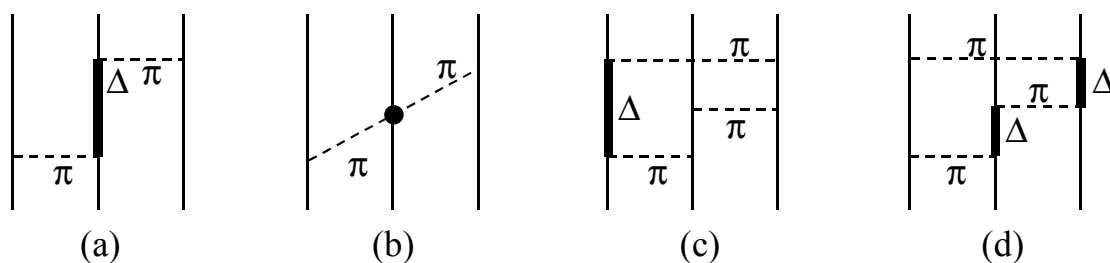


Figure 1.2: Three-nucleon forces. (a) The Fujita-Miyazawa three-body force. Two pions are exchanged between three nucleons, and during the process, one of the nucleons turns into a Δ resonance by P -wave excitation. (b) The S -wave two-pion exchange. (c) and (d) Three-pion exchange with one or two Δ in the intermediate states.

composite systems. When three or more nucleons interact with each other, the effects from the first excited state of the nucleon must be considered. This effect was first proposed by Fujita and Miyazawa [Fujita, 1957]. Figure 1.2(a) shows the exchange of two pions between three nucleons with the excitation of an isobar Δ (first excited state of the nucleon, spin 3/2 and mass 1232 MeV). This interaction is attractive, and provides more binding energy in the nuclei. Several three-nucleon potential models have been proposed, including Urbana [Pudliner, 1995], Illinois [Pieper, 2001a], Tucson-Melbourne [Coon, 2001], and the Brazil models [Robillota, 1986].

In an earlier version of the Urbana-Illinois potential, the Urbana IX (UIX) [Pudliner, 1995], the three-nucleon potential can be written as

$$V_{ijk} = V_{ijk}^{2\pi,P} + V_{ijk}^R, \quad (1.4)$$

where $V_{ijk}^{2\pi,P}$ is the P -wave two-pion exchange (Fujita-Miyazawa) as shown in Figure 1.2(a), and is used to fit the binding energy of triton and ${}^4\text{He}$. The quantity V_{ijk}^R is the short-range phenomenological term to prevent the nuclear matter from being too dense. The combination of AV18 and UIX significantly improves the binding energy of the p -shell nuclei. As the mass number A increases, AV18+UIX still underbinds most of the nuclei. This problem leads to the investigation of the other possible channels shown in Figure 1.2(b,c,d). Furthermore, from the model, the neutron-rich ${}^8\text{He}$ is more underbound than ${}^8\text{Be}$, which indicates a possible isospin dependence of the three-nucleon force. For these reasons, the Illinois model [Pieper, 2001a], was proposed and can be written as

$$V_{ijk} = V_{ijk}^{2\pi,P} + V_{ijk}^{2\pi,S} + V_{ijk}^{3\pi} + V_{ijk}^R, \quad (1.5)$$

where the S -wave two-pion exchange is also included (Figure 1.2(b)). The more important addition is the three-pion exchange with one or two Delta's in the intermediate

states (Figure 1.2(c,d)). The three-pion exchange diagram contains many terms, and can be summarized in terms of the symmetric (S_σ and S_τ) and antisymmetric (A_σ and A_τ) operators on spin and isospin space. The three-pion exchange operator can be written approximately as

$$V_{ijk}^{3\pi} = A_{3\pi} \left(\frac{50}{3} S_\tau S_\sigma + \frac{26}{3} A_\tau A_\sigma \right), \quad (1.6)$$

$$\text{where } S_\tau = 2 + \frac{2}{3} (\tau_i \cdot \tau_j + \tau_j \cdot \tau_k + \tau_k \cdot \tau_i) = \frac{4}{3} T_{total}^2 - 1 \quad (1.7a)$$

$$\text{and } A_\tau = \frac{1}{3} i \tau_i \cdot \tau_j \times \tau_k = -\frac{1}{6} [\tau_i \cdot \tau_j, \tau_j \cdot \tau_k]. \quad (1.7b)$$

In Eq. 1.7a, $\vec{T}_{total} = \frac{1}{2} (\vec{\tau}_i + \vec{\tau}_j + \vec{\tau}_k)$ is the total isospin of the three nucleons. The symmetric operator S_τ is the projector onto the triplet $T_{total} = 3/2$ state, $S_\tau = 4P_{T=3/2}$, and it vanishes when $T_{total} = 1/2$. On the other hand, A_τ is zero in $T_{total} = 3/2$ states since any two parallel vectors produce the zero for the product $\tau_j \times \tau_k$. Because of this isospin dependence, it is possible to extract the strength of the interaction from the experiments although the strength is much weaker than the two-pion exchange terms. For the s -shell nuclei, *e.g.* ${}^3\text{H}$ and ${}^3,4\text{He}$, there are no isospin triplet states. Thus, the properties of these nuclei are sensitive only to the $T = 1/2$ part of the three-nucleon force, *i.e.* the antisymmetric part. For the p -shell nuclei, both $T = 1/2$ and $3/2$ states are present, and the symmetric part of the potential provides the attractive force, while the antisymmetric part is slightly repulsive.

Experiments have been performed on deuteron-nucleon elastic scattering to look for the evidence of the three-nucleon forces [Cadman, 2001] and [Meyer, 2004]. No clear

conclusions have been made, however. Furthermore, the deuteron-nucleon scattering is only sensitive to the $T = 1/2$ part of the potential, and provides no information for the $T = 3/2$ part. Possible experiments including neutron-triton or proton- ^3He scattering may provide the necessary information on the $T = 3/2$ states. However, the interpretation of the scattering results for such complex nuclei are too difficult to clearly identify the signatures of the three-nucleon forces. Thus far, the neutron-rich light nuclei are the best testing ground for the $T = 3/2$ part of the three-nucleon force. The ground-state properties, *e.g.* the binding energy and the radius can set stringent constraints on the three-nucleon force. This motivates the initiation of the present program to measure the nuclear charge radii of the extremely neutron-rich ^6He and ^8He nuclei.

1.3 Quantum Monte Carlo Calculation of Light Nuclei

After the potential model is constructed, the wave function and eigenenergy of the nuclei can then be solved numerically. Several methods have been developed including the Faddeev [Nogga, 2000], correlated hyperspherical harmonics (CHH) [Kievsky, 1994], and variational and Green's function Monte Carlo methods (VMC and GFMC) [Carlson, 1987]. Here, I briefly describe the Monte Carlo methods, and show the results of the light nuclei using AV18 and Illinois potential by the Argonne group.

The variational method is used to obtain an approximate solution of the many-body Schrödinger equation. A trial function is selected with adjustable parameters to minimize the expectation value of the ground state energy:

$$E_{\text{trial}} = \frac{\langle \Psi_{\text{trial}} | H | \Psi_{\text{trial}} \rangle}{\langle \Psi_{\text{trial}} | \Psi_{\text{trial}} \rangle} \geq E_0 , \quad (1.8)$$

where H is the Hamiltonian from the nuclear potential model, and E_0 is the ground state energy. The final wave function which minimizes the eigenenergy can then be written in an expansion of states with specific spin and isospin: $\Psi = \sum_k C_k |k\rangle$, where each of the states is a N -dimensional array with N equal to $2^A \times C_Z^A$. The size of the array and the computing difficulty increase exponentially with A . The result from the VMC is usually used as the starting trial function for the GFMC. The Green's function Monte Carlo is based on the propagation of the wave function under the Hamiltonian:

$$\Psi_0 = \lim_{n\Delta T \rightarrow \infty} [e^{-(H-E_0)\Delta T}]^n \Psi_{\text{trial}}, \quad (1.9)$$

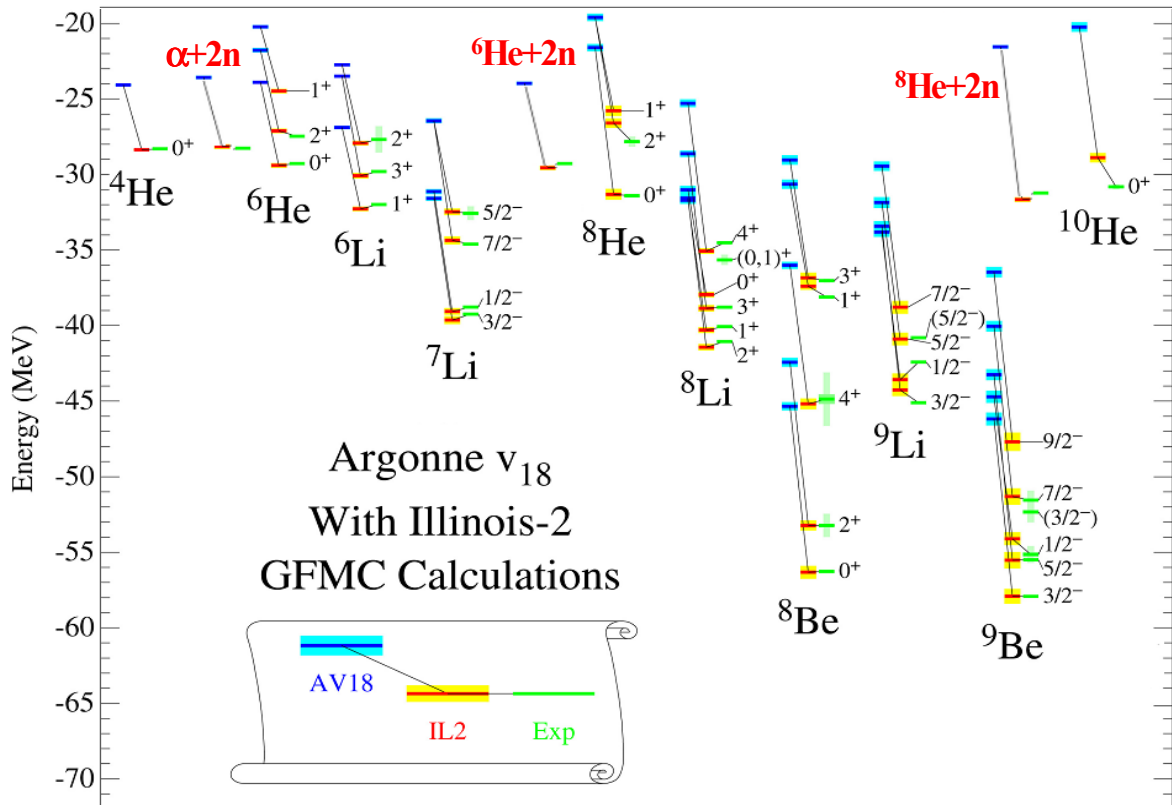


Figure 1.3: GFMC of the binding energy of light nuclei [Pieper, 2001b]. The blue and red bars indicate GFMC using AV18 and AV18+IL2 potential, respectively. The green bar is the experimental result. With the addition of the three-nucleon potential, the calculation significantly agrees better with the experiments.

where ΔT is a small time step, and n is the total number of steps integrated. If $n\Delta T$ is long enough, E_0 is the exact solution of the ground state energy, and Ψ_0 is the ground state wave function. The energy spectrum of the light nuclei is calculated using GFMC as shown in Figure 1.3.

The inclusion of the three-nucleon potential significantly improves the agreement between the calculation and the experiments. One may see from Figure 1.3, with the AV18 potential alone, ${}^6\text{He}$ and ${}^8\text{He}$ are not bound, and ${}^6\text{He}$ may break into $\alpha+2n$. With AV18+IL2, the energy spectra for both ground states and excited states of the light nuclei are predicted very well. The radius of the light nuclei can then be a strong constraint of the theory.

1.4 Neutron-Rich ${}^6\text{He}$ and Cluster Models

Neutron-rich ${}^6\text{He}$ is believed to exhibit two loosely bound neutrons and a tight α -particle core after the experiment by Tanihata *et al.* [Tanihata, 1985]. More details on the nuclear property of ${}^6\text{He}$ will be discussed in section 2.2 and 4.1. Using this simplified picture as shown in Figure 1.4, the ${}^6\text{He}$ can be thought of as a three-body system. The difference in charge radii between ${}^4\text{He}$ and ${}^6\text{He}$ nuclei can then be attributed to the center-of-mass

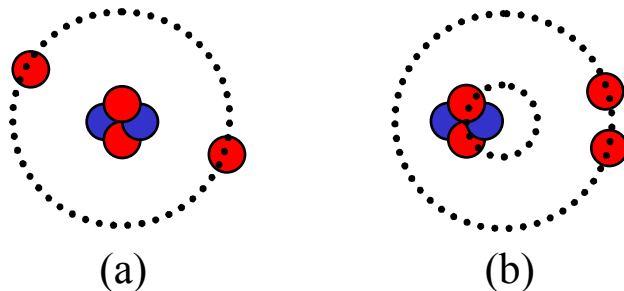


Figure 1.4: Correlation between the two valence neutrons. (a) The charge radius of ${}^6\text{He}$ is the same as that of ${}^4\text{He}$. (b) The charge radius is increased due to the orbital motion.

motion between the α particle and the two valence neutrons. From the geometry (Figure 1.4b), it is straightforward to derive the relation:

$$\langle r_{pt}^2 \rangle_{\text{He6}} = \langle r_{pt}^2 \rangle_{\alpha} + (1/9) \langle R^2 \rangle_{\alpha-2n}, \quad (1.10)$$

where $\langle r_{pt}^2 \rangle_{\text{He6}}$ and $\langle r_{pt}^2 \rangle_{\alpha}$ are the mean-square point-proton radii of ${}^6\text{He}$ and α particle (see Chapter 9 for definition of point-proton radius), and $\langle R^2 \rangle_{\alpha-2n}$ is the mean-square separation between the α core and the C.M. of the two neutrons. If we assume the α core in the ${}^6\text{He}$ nucleus is identical to the ${}^4\text{He}$ nucleus, the increase of the ${}^6\text{He}$ charge radius is then due to the spatial correlation between the two valence neutrons.

In cluster models, ${}^6\text{He}$ is described as a three-body system. Since any two of the three components are unbound, it is also called a “Borromean nucleus” (The name derives from the symbol of the ancient princes of Borromeo. Three rings interlocked in such a way that the removal of any of the rings will cause the remaining two to fall apart). The system is usually described in the normal-mode coordinates [Funada, 1994] as shown in Figure 1.5(a,b,c). The interactions can be from empirical functions, *e.g.* Fermi type or Gaussian potentials and parameterized by n - ${}^4\text{He}$, and n - ${}^6\text{He}$ scattering data and

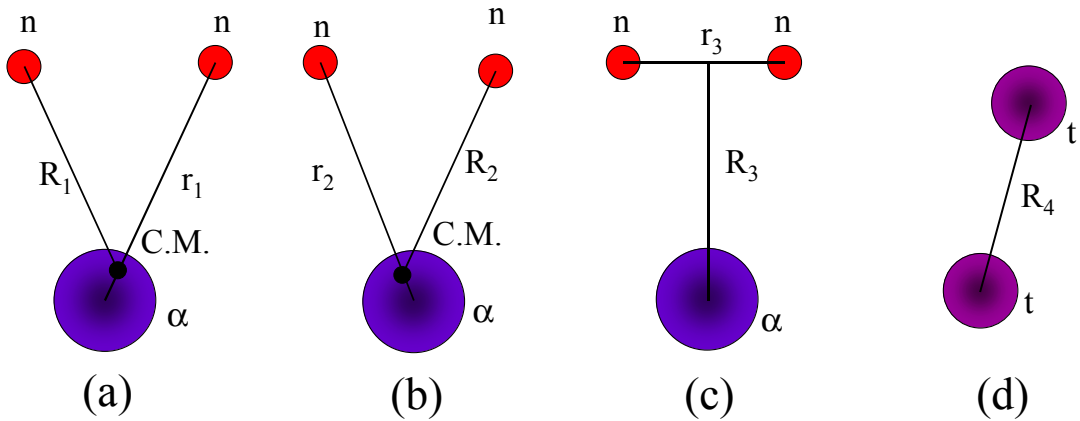


Figure 1.5: Different coordinates for the α -n-n and triton-triton clusters.

also a zero-range n-n interaction [Esbensen, 1997] or by more realistic n-n potential such as Argonne v_{14} in [Funada, 1994]. Some models may also include the triton-triton cluster as shown in Figure 1.5(d) [Wurzer, 1997].

Since the cluster models assume the α core is not modified by the additional two neutrons, a discrepancy between the calculation and reality may be attributed to this inadequate assumption. In fact, the *ab initio* quantum Monte Carlo calculation using AV18+IL2 shows a small but noticeable increase of the proton-proton separation in ${}^6\text{He}$ nucleus compared to that in ${}^4\text{He}$ [Pieper, 2001b].

Chapter 2

Methods for Measuring Nuclear Charge Radii

The methods for measuring the nuclear charge radii are summarized in this chapter. An electromagnetic probe is required for a model-independent interpretation of the root-mean-square charge radius from the experimental data. The most commonly used method is elastic electron scattering. Many electron scattering experiments were performed in the past five decades, and have provided a rich database on most stable or long-lived nuclei. Unfortunately, the electron scattering experiments cannot be applied easily to short-lived targets.

On the other hand, with the capability of producing radioactive nuclear beams in some accelerator facilities, the inverse kinematics scattering on various nuclear targets can be performed, and the interaction radii of those radioactive nuclei can be extracted from the interaction cross section. This process mostly involves strong interactions, and the separation of the contribution from protons and neutrons in the nuclei is model-dependent. Another method is based on the shift of the electronic energy levels caused by the finite size of the nucleus. These include isotope shifts in the optical or X-ray transition, and muonic atom spectroscopy. By measuring the frequency shift in the atomic transitions, information for the nuclear charge radius can be extracted.

2.1 Electron Scattering

The first demonstration of obtaining nuclear size information using particle scattering experiments was Rutherford scattering in 1906. From α scattering on a target, Rutherford concluded the size of the nucleus is less than 10^{-14} m. Unlike α particles, electrons are structureless point-like objects that only interact electromagnetically. Therefore, electron scattering avoids the complexity of the strong interaction between the projectile and the target, and provides clean information about the charge distribution in the nucleus. Considering relativity and the spin of the electrons, the differential cross section by spinless point-like nuclei can be expressed by the Mott scattering formula:

$$\left(\frac{d\sigma}{d\Omega}\right)_{Mott} = \frac{Z^2 e^4 \cos^2(\theta/2)}{4p_0^2 \sin^4(\theta/2) [1 + (2p_0/M)\sin^2(\theta/2)]}, \quad (2.1)$$

where Ze and M are the charge and mass of the nucleus respectively, and p_0 is the momentum of the incoming electron. Since the nucleus is not a point-like particle, the formula is modified by adding the nuclear electric and magnetic form factors, which contain information of the charge and magnetization distributions inside the nucleus. The Rosenbluth formula explicitly expresses the cross section for arbitrary nuclei as

$$\left(\frac{d\sigma}{d\Omega}\right) = \left(\frac{d\sigma}{d\Omega}\right)_{Mott} \left\{ A_0(q^2) + B_0(q^2) \left[\frac{1}{2} + \left(1 + \frac{q^2}{4M^2} \right) \right] \tan^2(\theta/2) \right\}, \quad (2.2)$$

where q^2 is the 4-momentum transfer squared, defined as

$$q^2 \equiv (\vec{p}_f - \vec{p}_i)^2 - (E_f - E_i)^2, \quad (2.3)$$

where \vec{p}_i and E_i are the momentum and energy of the incoming electron, and \vec{p}_f and E_f are that of the outgoing electron after scattering off the nucleus. $A_0(q^2)$ and $B_0(q^2)$,

functions of q^2 , are the form factors associated with the charge and magnetization distribution of the nucleus respectively. For a spin-0 nucleus:

$$A_0(q^2) = \frac{G_E(q^2)}{1 + \frac{q^2}{4M^2}} \quad \text{and} \quad B_0(q^2) = 0, \quad (2.4)$$

where $G_E(q^2)$ is the Sachs charge form factor and is the Fourier transform of the charge distribution, and the factor $1 + \frac{q^2}{4M^2}$ is the kinematical recoil correction. For $q \rightarrow 0$,

$q^2 \approx \vec{q}^2$, where \vec{q} is the three-momentum transfer, one can expand $G_E(q^2)$ in powers of \vec{q} :

$$\begin{aligned} G_E(q^2) &= G_E(\vec{q}^2) = \int \rho(\vec{r}) e^{i\vec{q}\cdot\vec{r}/\hbar} d^3\vec{r} = \int \rho(\vec{r}) [1 + (i\vec{q}\cdot\vec{r}) + \frac{1}{2!}(i\vec{q}\cdot\vec{r})^2 + \dots] d^3\vec{r} \\ &= \int \rho(\vec{r}) d^3\vec{r} - \frac{q^2}{6\hbar^2} \int r^2 \rho(r) d^3\vec{r} + \dots = Ze - Ze \frac{q^2}{6} \frac{\langle r_c^2 \rangle}{\hbar^2} + \dots, \end{aligned} \quad (2.5)$$

where Ze is the total charge of the nucleus, and $\langle r_c^2 \rangle$ is the mean-square charge radius, defined as

$$\langle r_c^2 \rangle = \frac{1}{Ze} \int r^2 \rho(\vec{r}) d^3\vec{r}. \quad (2.6)$$

Conventionally, $G_E(q^2)$ is normalized to the total charge, $G_E(0) = Ze$, and the mean-square charge radius can then be expressed by the charge form factor as

$$\langle r_c^2 \rangle = -6 \frac{dG_E(q^2)}{dq^2} \Big|_{q^2=0}, \quad (\text{using } \hbar = c = 1). \quad (2.7)$$

This method was first performed by Lyman *et al.* [Lyman, 1951], and was applied to most of the stable or long-lived isotopes. For heavy elements, the charge radius is closely proportional to $A^{1/3}$, $\langle r_c^2 \rangle^{1/2} = 1.12 A^{1/3}$ fm, where A is the mass number. This indicates

the density saturation for the nuclear matter. For light elements, the nuclear charge radii of ${}^4\text{He}$ and ${}^3\text{He}$ were measured to be 1.676(8) fm [Sick, 1982], and 1.959(30) fm [Amroun, 1994] respectively.

2.2 Nuclear Reaction Cross Section and Elastic Proton Scattering

The production of short-lived radioactive nuclear beams has enabled the study of unstable nuclei that cannot be measured by electron scattering. The radioactive nuclei are produced in flight by the nuclear reactions from an accelerated stable beam, and are separated by a fragment separator. The produced radioactive nuclei are accelerated again as a secondary beam. The radioactive beam can then be used for scattering experiments on stable targets in inverse kinematics. The interaction cross section of both the elastic and inelastic scattering is related to the matter radii of the target and the projectile, and can be estimated as

$$\sigma_I = \pi (R_{\text{target}} + R_{\text{projectile}})^2. \quad (2.8)$$

Since it is difficult to detect all the scattered nuclei in the full solid angle, the experiment is usually designed to detect the unaffected nuclei in a transmission experiment. By using different combinations of the target and projectile, the information for individual nuclei can be extracted.

In the case of ${}^6\text{He}$, the interaction cross section on different targets, for example, Be, C, and Al, was first measured by Tanihata *et al.* [Tanihata, 1985]. In a series of experiments on helium isotopes, Tanihata discovered the unusually large increase of the interaction cross section from ${}^{3,4}\text{He}$ to ${}^{6,8}\text{He}$, which was interpreted as the large radial

extent of the matter distribution in the neutron-rich ${}^{6,8}\text{He}$. Furthermore, the following relations were also observed:

$$\sigma_I({}^6\text{He}) \approx \sigma_I({}^4\text{He}) + \sigma_{2n}({}^6\text{He})$$

$$\text{and } \sigma_I({}^8\text{He}) \approx \sigma_I({}^4\text{He}) + \sigma_{4n}({}^8\text{He}) \neq \sigma_I({}^6\text{He}) + \sigma_{2n}({}^8\text{He}), \quad (2.9)$$

where σ_{2n} is the two-neutron removal cross section. This indicates the additional neutrons in the ${}^6\text{He}$ and ${}^8\text{He}$ nucleus have a much larger spatial extent than that of the α -particle core. Later, more extensive studies were performed for Li, Be, and B isotopes [Tanihata, 1988], and both ${}^{11}\text{Li}$ and ${}^{14}\text{Be}$ were found to have similar behaviors, as shown in Figure 2.1. These nuclei are believed to have neutron-skin or neutron-halo structures. This discovery significantly changes the common view that the proton and neutron distributions inside the nucleus are proportional.

A more accurate measurement of the ${}^6\text{He}$ and ${}^8\text{He}$ interaction radii was performed

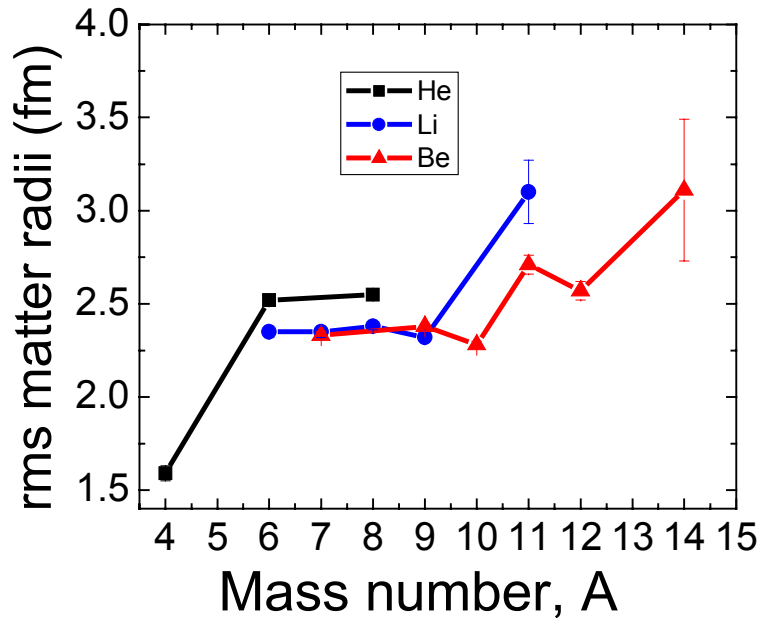


Figure 2.1: Root-mean-square matter radii of He, Li, Na and Be isotopes, [Tanihata, 1988]. The halo structure of ${}^{6,8}\text{He}$, ${}^{11}\text{Li}$, and ${}^{14}\text{Be}$ is suggested.

at GSI using elastic scattering on a proton target [Alkhazov, 1997]. However, both the nuclear reaction experiment and the elastic proton scattering involve mostly strong interactions, and the neutron and proton distributions cannot be separated using a model-independent treatment. Usually a Gaussian distribution of the core nucleon density, and either a Gaussian or a harmonic-oscillator distribution of the valence neutrons are used. The root-mean-square charge and matter radii can then be estimated.

2.3 Muonic Atom X-Ray Spectroscopy

A different approach to determine the charge distribution inside the nucleus is based on the shift of the electronic energy levels due to the finite size of the nucleus. In first order, it can be shown by perturbation theory that the energy shift is

$$\Delta E = \int \Psi(\vec{r})^* [V(\vec{r}) - V_0(\vec{r})] \Psi(\vec{r}) d^3 r, \quad (2.10)$$

where V is the electric potential the electron “feels” due to a nucleus with non-zero size, V_0 is that of a point-like nucleus, and $\Psi(\vec{r})$ is the electron’s wave function. By Gauss’s theorem, $V - V_0$ approaches zero quickly once the electron is outside the nucleus. Therefore, the electron must have a non-vanishing wave function at the origin so that the integration of Eq. 2.10 is non-zero. Furthermore, since the size of the nucleus is at the order of a femto-meter, five orders of magnitude smaller than the electron orbit, this effect is expected to be very small. The small change in the atomic energy levels can be probed using high-resolution spectroscopy, and information about the nuclear charge radii can be obtained by the isotope shift measurements. This will be described in more detail in Chapter 3.

Another method is to use the muonic atoms, taking advantage of the muon's heavier mass. The muon is 207 times more massive than the electron. When a negative muon is captured by the nucleus, it can form a muonic atom. The muon will decay in orbit with a lifetime of 2 μ s. From Eq. 2.10, the energy shift due to the nuclear size is proportional to the probability of finding the electron/muon inside the nucleus:

$$\Delta E \approx |\Psi(0)|^2 \approx \left(\frac{1}{a_0}\right)^3 \quad \text{and} \quad a_0 = \frac{4\pi\epsilon_0\hbar^2}{me^2}. \quad (2.11)$$

The quantity a_0 is the Bohr radius for a hydrogen-like atom, and is inversely proportional to the mass of the orbiting lepton. The energy shift can then be estimated to be a factor of $(m_\mu/m_e)^3$, an increase for a muonic atom over a normal atom. X-ray spectroscopy was performed by Carboni *et al.* [Carboni, 1977], where the muonic helium ion $(\mu^- \text{ } ^4\text{He})^+$ was formed, and partially (4%) excited to the metastable states by collisions with the stopping buffer helium gas at high pressure (40 atm). A spectroscopy laser was tuned across the $2S_{1/2}$ – $2P_{3/2}$ transition, and the X-ray decay from $2P_{3/2}$ – $1S_{1/2}$ was detected as shown in Figure 2.2. For this hydrogen-like system, the $2S_{1/2}$ – $2P_{3/2}$ transition energy can be calculated explicitly to be $E_{2s-2p} = (1813.1 \text{ meV} - 102.0 \langle r_c^2 \rangle \text{ meV/fm}^2) \pm 1 \text{ meV}$ [Borie,

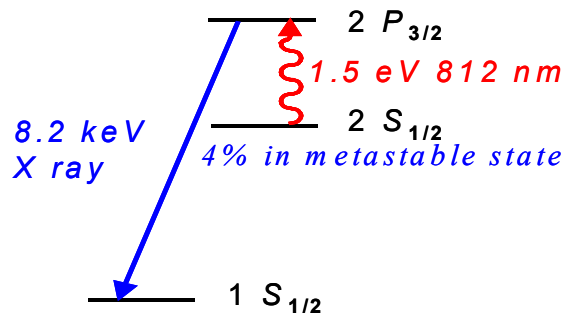


Figure 2.2: Muonic helium ion energy level.

1978]. A determination of the transition wavelength, 811.68(15) nm, indicated the rms charge radius of the ${}^4\text{He}$ nucleus to be 1.673(1) fm.

Unfortunately, this result remains controversial because of subsequent difficulties in observing the metastable muonic ions at high pressure. At 40 atm, the metastable quenching rate due to collisions is much faster than the muon-decay rate. As reported in [Hauser, 1992], no metastable 2S-state muonic ions were detected at helium pressure higher than 6 atm, which suggested the upper bound of the lifetime $\tau_{2S} < 150$ ns. This is contradictory to the result of Carboni *et al.*, in which the 2S-state lifetime was measured to be 1.6 μs . Because of this controversy, the charge radius of ${}^4\text{He}$ measured by electron scattering, 1.676(8) fm [Sick, 1982], is also used for comparison.

2.4 Atomic Isotope Shift

Like the muonic atoms, the electronic energy levels of normal atoms can exhibit similar shift due to the finite size of the nucleus. In a multi-electron atom, this can be performed on the optical transition of the valence electrons, or on the X-ray transition of the inner electrons. In either case, the electron wave function must be known. However, even in the case of the simple two-electron system, the theoretical calculation of the total transition frequency is not precise enough to extract the charge radius because of the vacuum polarization effect. But this effect largely cancels when the difference in transition frequency is compared between isotopes. The measurement of the isotope shift will then give the difference of the mean-square charge radii between isotopes. For example, the charge radius of ${}^4\text{He}$ has been measured by electron scattering and muonic atom spectroscopy very precisely, and given the difference of the charge radii from ${}^4\text{He}$ – ${}^6\text{He}$

isotope shift measurement, the charge radius of ${}^6\text{He}$ can be obtained. This approach forms the basic foundation of this experiment. More detail for the atomic isotope shift method will be presented in the next chapter. The charge radii of light nuclei measured by different methods are summarized in Table 2.1.

Table 2.1: Theoretical calculation and experimental results of rms nuclear charge radii* (in fm).

	Theory ¹	e ⁻ scattering	Elastic p scattering	Nuclear reaction	Atomic method
${}^1\text{H}$		0.895(18) ²			0.883(14) ¹⁰
${}^2\text{H}$	2.14(1)	2.128(11) ³			2.145(6) ¹¹
${}^3\text{H}$	1.77(1)	1.755(86) ⁴			
${}^3\text{He}$	1.97(1)	1.959(30) ⁴			1.9506(14) ¹²
${}^4\text{He}$	1.68(1)	1.676(8) ⁵	1.71(3) ⁷	1.78(4) ⁹	1.673(1) ¹³
${}^6\text{He}$	2.06(1)		2.03(11) ⁷	2.34(3) ⁹	This work
${}^6\text{Li}$	2.54(1)	2.57(10) ⁶	2.59(6) ⁸	2.47(3) ⁹	2.51(10) ¹⁴
${}^7\text{Li}$	2.40(1)	2.41(10) ⁶		2.41(2) ⁹	2.41(10) ¹⁴
${}^7\text{Be}$	2.59(1)			2.51(2) ⁹	
${}^8\text{He}$	2.00(1)		1.69(11) ⁷	2.26(2) ⁹	
${}^8\text{Li}$	2.24(1)			2.40(2) ⁹	2.31(11) ¹⁵
${}^8\text{B}$	2.59(1)			2.59(5) ⁹	

*The point-proton radius from the theory is converted to the charge radius using the formula (see Chapter 9): $\langle r_c^2 \rangle = \langle r_{pt}^2 \rangle + \langle R_p^2 \rangle + N/Z \langle R_n^2 \rangle + \frac{3}{4}(M_p)^{-2}$, $\langle R_p^2 \rangle^{1/2} = 0.895(18)$ fm [Sick, 2003], and $\langle R_n^2 \rangle = -0.120(5)$ fm² [Kopecky, 1995, 1997].

¹[Pieper, 2001b], ²[Sick, 2003], ³[Sick, 1996], ⁴[Amroun, 1994], ⁵[Sick, 1982], ⁶[Bumiller, 1972], ⁷[Alkhazov, 2002], ⁸[Egelhof, 2002], ⁹[Tanihata, 1988], ¹⁰[Melnikov, 2000], ¹¹[Huber, 1998] and use the result from ¹⁰, ¹²[Shiner, 1995], ¹³[Borie, 1978], ¹⁴[Bushaw, 2003], ¹⁵[Ewald, 2004]

⁷The matter radius is used for ${}^4\text{He}$. ⁸The matter radius is used.

^{14,15}The radius of ${}^7\text{Li}$ is taken from electron scattering and ${}^6\text{Li}$ and ${}^8\text{Li}$ are from the isotope shift measurement.

Chapter 3

Atomic Isotope Shift and Nuclear Charge Radii

The effects of the nucleus on atomic energy levels include the finite mass and volume of the nucleus, and the electric or magnetic moment interaction between the nucleus and electrons. The first two effects cause the isotope shifts, and the moments of the nucleus cause the hyperfine structures. The mass shift includes the normal mass shift (NMS) and the specific mass shift (SMS). The former effect arises from the difference in the reduced mass of the electron and can be precisely determined if the nuclear mass is known. The latter involves the correlation of the motion between the electrons, and in general, is very difficult to calculate.

In light elements the isotope shift is dominated by the mass shift because the fractional change of the nuclear mass between isotopes is large, while in heavy elements the volume effect (field shift) is more important. In a typical optical transition of helium, the mass shift between ^4He and ^6He is usually tens of GHz, while the field shift is only about 1 MHz. As a result, high-resolution spectroscopy as well as precise atomic calculation of specific mass shift are required to extract the nuclear charge radius information.

3.1 Mass Shift

The origin of the mass shift can be understood from the Bohr atomic model:

$$E_n^0 = -hR\left(\frac{1}{n^2}\right), \quad (3.1)$$

where E_n^0 is the energy of the state with quantum number n , and $R = \alpha^2 m_e c / 2h$, is the

Rydberg constant. For finite nuclear mass, the electron mass is modified to the reduced

mass, $\mu = m_e \frac{M_A}{m_e + M_A}$, so the energy level becomes

$$E = E^0 \left(1 - \frac{m_e}{m_e + M_A}\right) \approx E^0 \left(1 - \frac{m_e}{M_A}\right), \quad (3.2)$$

where E^0 is the energy with infinite nuclear mass, and M_A is the mass of the nucleus with

mass number A . The change of the total energy $-E^0 \frac{m_e}{M_A}$ can be thought of as the recoil

kinetic energy of the nucleus. For multi-electron atoms, the situation becomes more

complicated because of the relative motion of the electrons associated with the recoil

kinetic energy of the nucleus. The difference in recoil kinetic energy between a nucleus

with finite mass and infinite mass is

$$\Delta K = K_{M_A} - K_{M_\infty} = \frac{p^2}{2M_A} - \frac{p^2}{2M_\infty}, \quad (3.3)$$

where p is the momentum of the nucleus. By the virial theorem, the total energy is equal

to the negative of the kinetic energy, and by momentum conservation, the momentum of

the nucleus is equal to that of the electrons. Thus, the energy shift becomes

$$\Delta E = -\Delta K = -\frac{p^2}{2M_A} = -\frac{m_e}{M_A} \left[\frac{1}{2m_e} \sum_i \vec{p}_i \right]^2 = -\frac{m_e}{M_A} \left[\sum_i \frac{p_i^2}{2m_e} + \sum_{i \neq j} \frac{\vec{p}_i \cdot \vec{p}_j}{2m_e} \right], \quad (3.4)$$

where \vec{p}_i is the momentum of the i th electron. The first term, equal to $-E^0 \frac{m_e}{M_A}$, is just the normal mass shift in Eq. 3.2, and the second term is called the specific mass shift. It depends on the correlation between the electrons, and is a function of the electron's quantum state n, s, l , etc. It is clear in Eq. 3.4 that the NMS and SMS have the same nuclear mass dependence as $(M_A)^{-1}$. Therefore, the mass shift between the different isotopes, A and A' can be written as

$$\delta V_{MS}^{AA'} \propto \frac{1}{M_{A'}} - \frac{1}{M_A} = \frac{M_A - M_{A'}}{M_A M_{A'}} \propto N \frac{M_A - M_{A'}}{M_A M_{A'}} + S \frac{M_A - M_{A'}}{M_A M_{A'}}, \quad (3.5)$$

where N and S are the coefficients for the NMS and SMS respectively. Theoretical calculations of SMS are usually very difficult, and are more precise for hydrogen-like or helium-like atoms.

3.2 Field Shift

The field shift is the isotope shift due to the finite volume effect of the nucleus. When the electrons penetrate into the nucleus, the electrostatic potential no longer behaves like $1/r$ due to the screening effect. The electrostatic force that the electrons experience becomes smaller, and it causes the energy level to rise, (reducing the binding energy). In the most common S–P transitions, the ground S state will increase in energy, while the excited P state energy remains the same due to the electron's zero probability at the origin. As a result, the transition frequency will decrease if the nuclear charge radius gets larger. To quantitatively describe the field shift, we can consider the electrostatic potential between an s -shell electron with a spherically symmetric wave function, and a nucleus with

arbitrary charge distribution, $\rho(\vec{r})$. The electrostatic potential of the system is the integration of the nuclear charge distribution $\rho(\vec{r})$ multiplied by the potential produced by the electron, $V(\vec{r})$:

$$E = \int_{\text{all space}} \rho(\vec{r}) V(\vec{r}) d^3 \vec{r}. \quad (3.6)$$

Since the nuclear size is much smaller than the electron orbit, we can define a radius R_1 , where $\rho(\vec{r}) = 0$ if $|r| > R_1$, and the electron's wave function is constant, $\Psi(0)$, for $|r| < R_1$. Inside the sphere with $|r| < R_1$, the electron density is uniform, therefore it produces a parabolic potential which can be derived by Gauss's theorem to be

$$V(\vec{r}) = -2\pi e |\Psi(0)|^2 \left(R_1^2 - \frac{r^2}{3} \right) \text{ for } |r| < R_1. \quad (3.7)$$

Since $\rho(\vec{r}) = 0$ if $|r| > R_1$, the integration of Eq. 3.6 only needs to be performed inside the sphere with $|r| < R_1$, and it becomes

$$\begin{aligned} E &= \int_{|r| < R_1} \rho(\vec{r}) \left\{ -2\pi e |\Psi(0)|^2 \left(R_1^2 - \frac{r^2}{3} \right) \right\} d^3 \vec{r} \\ &= V(0) \int_{|r| < R_1} \rho(\vec{r}) d^3 \vec{r} + \frac{2\pi e}{3} |\Psi(0)|^2 \int_{|r| < R_1} r^2 \rho(\vec{r}) d^3 \vec{r}, \end{aligned} \quad (3.8)$$

where $V(0) \equiv -2\pi e |\Psi(0)|^2 R_1^2$. By definition, the quantity, $\int_{|r| < R_1} \rho(\vec{r}) d^3 \vec{r} = Ze$, is the total

charge of the nucleus, and $\int_{|r| < R_1} r^2 \rho(\vec{r}) d^3 \vec{r} = Ze \langle r_c^2 \rangle$ is the definition of the mean-square

charge radius multiplied by Ze . As a result, one may write

$$E = ZeV(0) + \frac{2\pi}{3} Ze^2 |\Psi(0)|^2 \langle r_c^2 \rangle. \quad (3.9)$$

The first term represents the interaction between a point-like nucleus and the electron. The second term is the finite-size correction. It is important to note that we do not assume any charge distribution in the nucleus. Therefore, Eq. 3.9 is valid even in the case of deformed nuclei. The only assumption we make is the constant wave function $\Psi(0)$ of the electron inside the nucleus, which is a good approximation for most atoms. In the case of the muonic atom, however, the wave function may change considerably inside the nucleus, and a more complicated analysis must be made.

The field shift of electronic atoms is too small to determine the $\langle r_c^2 \rangle$ directly by measuring the total transition frequency. Although the spectroscopy can be very precise, the QED calculation of the few-electron systems lacks the required precision to extract the charge radius information. However, the change of $\langle r_c^2 \rangle$ in different isotopes can be obtained because most of the theoretical uncertainties cancel between isotopes. The field shift between isotopes is then given by

$$\delta v_{FS}^{AA'} = -\frac{2\pi}{3} Ze^2 \Delta |\Psi(0)|^2 \delta \langle r_c^2 \rangle^{AA'}, \quad (3.10)$$

where $\Delta |\Psi(0)|^2$ is the change of the electron's wave function at the nucleus between the upper and lower states, and $\delta \langle r_c^2 \rangle^{AA'}$ is the change in the nuclear mean-square radius. In order to extract the charge radius information, one needs a precision calculation of SMS as well as the electron's wave function, which are not easy tasks. For a relatively simple system like helium, it is possible to perform QED many-body calculations to reach the precision that the experiment requires.

For most atoms with $Z > 3$, the atomic calculations of the SMS and the electronic factor of the field shift (the electron's wave function at origin) are not precise enough to

extract the nuclear charge radius information. If more than one transition is measured for several pairs of isotopes, however, the SMS and the electronic factor of the field shift can be determined. This method is known as the King Plot [King, 1984]. The isotope shift in two different transitions between isotopes A and A' can be derived using the following relations from Eq. 3.5 and Eq. 3.10:

$$\begin{aligned}\delta\nu_1^{AA'} &= C_1 \frac{M_A - M_{A'}}{M_A M_{A'}} + F_1 \delta \langle r_c^2 \rangle^{AA'}, \\ \delta\nu_2^{AA'} &= C_2 \frac{M_A - M_{A'}}{M_A M_{A'}} + F_2 \delta \langle r_c^2 \rangle^{AA'},\end{aligned}\tag{3.11}$$

where C_1 and C_2 are the mass shift coefficients for transition 1 and 2, and F is the electronic factor. The relation between $\delta\nu_1^{AA'}$ and $\delta\nu_2^{AA'}$ can be derived using Eq. 3.11 as

$$\xi \delta\nu_2^{AA'} = \frac{F_2}{F_1} (\xi \delta\nu_1^{AA'}) + C_2 - C_1 \frac{F_2}{F_1}, \text{ where } \xi \equiv \frac{M_A M_{A'}}{M_A - M_{A'}}\tag{3.12}$$

By plotting the modified isotope shift $\xi \delta\nu_1^{AA'}$ against $\xi \delta\nu_2^{AA'}$ among several pairs of isotopes, a straight line is formed with the slope F_2/F_1 and intercept $C_2 - C_1(F_2/F_1)$. If the specific mass shift and the electronic factor of the field shift are known for transition 1, then they may be deduced for transition 2.

3.3 Atomic Theory of Helium

The exact solution of the Schrödinger equation of the atomic system only exists in the hydrogen atom. For helium, the non-relativistic Schrödinger equation of the three-body system can be written as

$$\left[\frac{1}{2M_A} P_N^2 + \frac{1}{2m_e} \sum_{i=1}^2 P_i^2 + V(R_N, R_i) \right] \Psi = E \Psi,\tag{3.13}$$

where P and R are the momentum and position operators respectively of the nucleus and the i th electron. Since the choice of the origin is arbitrary, it is easier to define the coordinate using the reference frame of the nucleus. As a result, $r_i = R_i - R_N$, $P_N = 0$, $R_N = 0$, and after proper normalization of the coefficients and using the reduced mass of the electron μ , the equation becomes

$$\left[-\frac{1}{2}\nabla_1^2 - \frac{1}{2}\nabla_2^2 - \frac{\mu}{M_A}\nabla_1 \cdot \nabla_2 - \frac{Z}{r_1} - \frac{Z}{r_2} + \frac{1}{r_{12}} \right] \Psi(r_1, r_2) = E\Psi(r_1, r_2). \quad (3.14)$$

The two cross terms, $\nabla_1 \cdot \nabla_2$ and $1/r_{12}$, are the sources of complication in the calculations. The first one related to the momentum correlation of the two electrons is called mass polarization, which results in the specific mass shift as mentioned in section 3.1. Since it scales as μ/M_A , it can be treated as a small perturbation. The second one, $1/r_{12}$, is the Coulomb repulsion, which is large in the case of helium (~ 1 eV). As a result, the Hartree-Fock (HF) approximation cannot be applied. Furthermore, due to the high precision requirement of the experiments (< 100 kHz), the HF technique is far from the required precision.

The high precision calculation by G.W.F. Drake [Drake, 1999] is based on the variational principle. For any normalized trial wave function Ψ_{trial} , the corresponding eigenenergy E_{trial} must satisfy

$$E_{\text{trial}} = \langle \Psi_{\text{trial}} | H | \Psi_{\text{trial}} \rangle \geq E_0, \quad (3.15)$$

where E_0 is the real ground state energy. The approach is to write Ψ_{trial} as a series expansion of some appropriately chosen bases with adjustable parameters, and then minimize the expectation value by systematically adjusting the parameters. To get the solution for the excited states, one can construct another trial function from the subset of

the functional space, which is orthogonal to the ground state wave function. The upper bound of the eigenenergy E_1 must also exist, and the wave function of the first excited state can be obtained.

Some corrections must be made after the non-relativistic variational calculations. These include relativistic corrections, anomalous magnetic moment corrections, QED corrections, relativistic mass corrections, and other high-order corrections. The difference between the theory and the experimental result will then be attributed to the nuclear volume effect. Table 3.1 lists the contributions and their orders of magnitude.

Table 3.1: Contributions for the helium energy level. $Z = 2$, $\mu/M = 1.37 \times 10^{-4}$, $\alpha^2 = 0.532 \times 10^{-4}$, from [Drake, 1999]

Contribution	Magnitude	Value
Non-relativistic energy	Z^2	4
Relativistic correction	$Z^4 \alpha^2$	9×10^{-4}
Anomalous magnetic moment	$Z^4 \alpha^3$	7×10^{-4}
Mass polarization (SMS)	$Z^2 (\mu/M)$	5×10^{-4}
Second-order mass polarization	$Z^2 (\mu/M)^2$	8×10^{-8}
Finite mass correction (NMS)	$Z^4 \alpha^2 (\mu/M)$	1×10^{-7}
QED correction (Lamb shift)	$Z^4 \alpha^3 \ln \alpha$	6×10^{-3}
Finite Nuclear Size	$Z^4 (\langle r_c^2 \rangle / a_0^2)$	2×10^{-9}

With the exception of the QED effect, most of the corrections can be determined very precisely (< 10 kHz). The Lamb shift, which arises from the vacuum polarization, is the effect that causes the level splitting between the 2S and 2P states in hydrogen. By measuring the total transition frequency, the Lamb shift can be determined. Alternatively, if one measures the isotope shift for the same transition, the uncertainty from the QED calculation largely cancels, and it gives the difference of the nuclear charge radius between isotopes. If one measures the fine structure splittings, not only the QED

correction cancels but also the nuclear charge radius effect is negligible. The high precision measurement of the fine structure splittings of helium is thus a powerful method to determine the fine structure constant α (1 kHz \rightarrow 10 ppb) [Drake, 1999]. The relation between those measurements is illustrated in Figure 3.1. By the isotope shift measurements, the charge radii of H–D and ^3He – ^4He have been determined to a very high precision [Huber, 1998], [Shiner, 1995].

In the isotope shift calculation of ^4He – ^6He , the major uncertainty is actually from the nuclear mass of ^6He (uncertainty $\sim 0.8 \text{ keV}/c^2$) [Audi, 1995]. With this information and the precise atomic theory of helium performed by G.W.F. Drake [Drake, 2004a], the mass shift and the field shift are

$$\text{IS}(2^3\text{S}_1-2^3\text{P}_2) = 34473.625(13) \text{ MHz} + 1.210(\langle r_c^2 \rangle_{\text{He4}} - \langle r_c^2 \rangle_{\text{He6}}) \text{ MHz}/\text{fm}^2. \quad (3.16a)$$

$$\text{IS}(2^3\text{S}_1-3^3\text{P}_2) = 43196.202(16) \text{ MHz} + 1.008(\langle r_c^2 \rangle_{\text{He4}} - \langle r_c^2 \rangle_{\text{He6}}) \text{ MHz}/\text{fm}^2. \quad (3.16b)$$

In this experiment, we probe the 2^3S_1 – 3^3P_2 transition. Taking the ^4He charge radius 1.676(8) fm from electron scattering result, and the ^6He charge radius ~ 2 fm from theoretical calculations, a 100 kHz uncertainty in the isotope shift measurement will result in $\sim 1\%$ uncertainty in determining the ^6He nuclear charge radius.

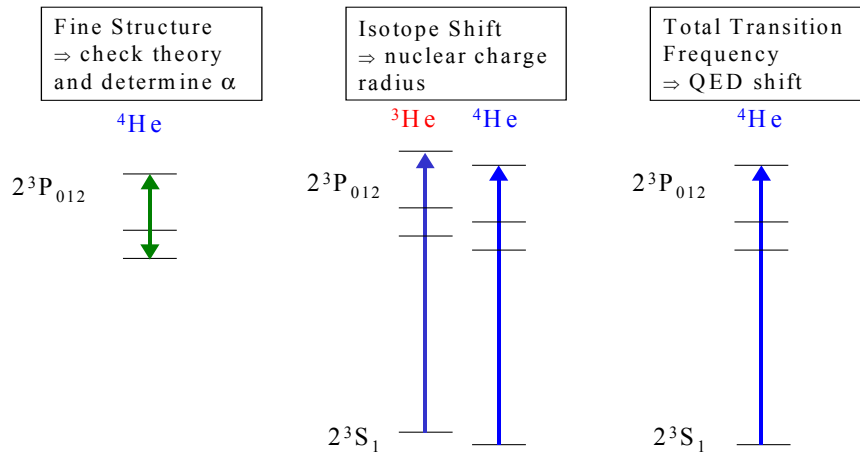


Figure 3.1: High precision measurements of helium and their interpretation.

Chapter 4

Production of ${}^6\text{He}$

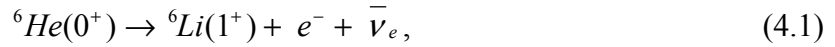
The ${}^6\text{He}$ used in this experiment was produced *via* the ${}^{12}\text{C}({}^7\text{Li}, {}^6\text{He}){}^{13}\text{N}$ reaction at the Argonne Tandem Linac Accelerator System (ATLAS) at Argonne National Laboratory. To perform the isotope shift measurement, the ${}^6\text{He}$ must be in the form of thermal atoms. Therefore, the carbon target, which is porous graphite, also acts as a neutralizer and stopper. The ${}^6\text{He}$ atoms diffused out of the target and were compressed by several turbo pumps along a transport pipe to either the discharge source chamber or to a collection chamber for β decay detection. From the decay half-life (807 ms), and the β energy spectrum, the ${}^6\text{He}$ was identified, and the production rate was estimated to be about $3 \times 10^6/\text{s}$ at the ${}^7\text{Li}$ beam current of 70 pA (particle nanoAmps). This production rate was sufficient for the spectroscopic measurement.

4.1 Nuclear Properties of ${}^6\text{He}$

The ${}^6\text{He}$ nucleus is a loosely bound system with the two-neutron separation energy of 0.97 MeV. The spin and parity of the ground state is $J^\pi = 0^+$, and the isospin is $T = 1$. It is bound, but unstable against β decay. The half-life is 806.7 ± 1.5 ms [Ajzenberg-Selove, 1984], and the main decay branch is β decay to the ground state of ${}^6\text{Li}$ ($J^\pi = 1^+$). A very small branching ratio ($\sim 10^{-6}$) of a deuteron and an α particle emission was also reported

[Riisager, 1990]. The mass of ${}^4\text{He}$ was measured to a precision of 0.3 ppb ($\delta M/M = 1 \text{ eV}/3.7 \text{ GeV}$), and the mass of ${}^6\text{He}$ was determined to be better than 0.2 ppm ($\delta M/M = 0.8 \text{ keV}/5.6 \text{ GeV}$) [Audi, 1995], which allows the calculation of the mass shift between ${}^4\text{He}$ and ${}^6\text{He}$ to a precision of better than 20 kHz in both the $2^3\text{S}_1-2^3\text{P}_J$ and $2^3\text{S}_1-3^3\text{P}_J$ atomic transitions.

The β decay of ${}^6\text{He}$:



has a Q value of 3.5 MeV, which is the maximum kinetic energy allowed for the emitted electron and the antineutrino. By measuring the end point of the β decay spectrum, the production of ${}^6\text{He}$ can be identified. Because the nuclear spin is changed by one unit in the decay process, the electron and antineutrino together must carry away one unit of angular momentum. This is the Gamow-Teller decay in which the spin of the electron and antineutrino are parallel. The rate of the β decay can be expressed in terms of the matrix element and the phase space of the final states:

$$\Gamma = \frac{1}{\tau} \propto |M_{if}|^2 f(Z_d, E_0), \quad (4.2)$$

where M_{if} is the matrix element connecting the initial and final states. The function f is the integral of all the possible energy states of the emitted electron and antineutrino up to the Q value of the reaction E_0 , and is modified by the Coulomb interaction from the daughter nucleus with charge Z_d . Table 4.1 shows a comparison of the decay between ${}^6\text{He}$ and a free neutron. The ft value is the product of the half-life $t_{1/2}$ and the f function, and is a direct indication of the strength of the matrix element.

From Table 4.1, the ft value of ${}^6\text{He}$ is similar to that of the free neutron, and so is the magnitude of the matrix element. Therefore, the overlap between the initial and final state wave functions of ${}^6\text{He}(\beta^-){}^6\text{Li}$ reaction is considerably large. The lifetime of ${}^6\text{He}$ is shorter than that of a free neutron because of the larger Q value.

Table 4.1: Comparison of half-life and ft value between neutron and ${}^6\text{He}$ decay.

	Half-life (s)	Q value (MeV)	$f(Z_d, E_0), E_0$ in MeV	$\log(ft)$ value
${}^6\text{He}$	0.807	3.5	$f(3, 3.5) = 1007$	2.9
Free neutron	887	1.3	$f(1, 1.3) = 1.6$	3.1

4.2 Production of ${}^6\text{He}$

The ${}^6\text{He}$ was produced *via* the nuclear stripping reaction (${}^7\text{Li}, {}^6\text{He}$) in which one proton from the ${}^7\text{Li}$ was stripped off by the target and ${}^6\text{He}$ was formed. The choice of the target depends on the target density and the interaction cross section. The production rate is the product of the following parameters. Rate = $I \cdot \rho \cdot d \cdot \sigma$, where I is the beam current, ρ is the nucleus number density, d is the penetration depth, and σ is the reaction cross section. Table 4.2 shows the cross sections in millibarn (1 barn = 10^{-24} cm²) for different targets with a ${}^7\text{Li}$ beam at 50 MeV.

Table 4.2: Cross section of (${}^7\text{Li}, {}^6\text{He}$) reaction for various targets.

Target	${}^9\text{Be}$	${}^{12}\text{C}$	${}^{13}\text{C}$	${}^2\text{H}$
$\sigma(\text{mb})$	0.60	0.21	0.16	0.75

The ${}^{12}\text{C}$ target (porous graphite) was used in this experiment because of its reasonable cross section, ease of use, and relatively short release time of the implanted helium atoms. The release time depends on the diffusion coefficient of helium in the

material. From a study of the diffusion time of implanted helium in Si and SiO₂ [Jung, 1994], the diffusion coefficient D is of the order of 10^{-8} m²/s at 800°C, and is related to the fraction of released helium and the original implanted helium by the formula:

$$D = \varepsilon^2 \frac{\pi d^2}{16\tau} \propto e^{-E_0/kT}, \quad (4.3)$$

where ε is the efficiency of release, d is the depth, τ is the time delay for release, and E_0 is the activation energy related to the material properties. Although the diffusion coefficient for graphite has not been reported, an efficiency $\varepsilon = 20\%$ was found by using the coefficient from SiO₂ and $d = 1$ mm, $\tau = 1$ sec. Because of the temperature dependence of the diffusion coefficient, it was found that the target should be heated to more than 700°C. The design of the target is shown in Figure 4.1. The cone shape of the target was used to reduce the implantation depth and shorten the diffusion time of the implanted ⁶He.

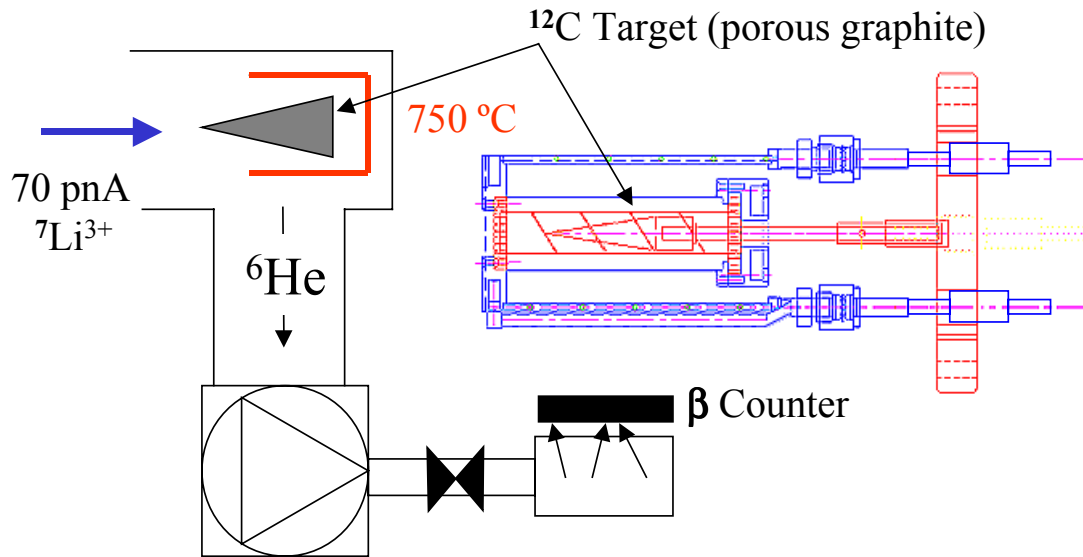


Figure 4.1: Target design and the detection chamber.

The ${}^6\text{He}$ produced was then transported by several turbo pumps to a collection chamber. When the flow of the ${}^6\text{He}$ reached a steady state, the control valve of the collection chamber was then closed, and the β decay of the ${}^6\text{He}$ was detected by a plastic scintillator coupled to a photomultiplier tube. The ${}^6\text{He}$ decay and energy spectrum of the β particles is shown in Figure 4.2 [Mueller, 2003]. The count rate was modified by the dead time correction, and the energy spectrum was calibrated by a ${}^{207}\text{Bi}$ source. It was found that the total process including the nuclear reaction, ${}^6\text{He}$ diffusion out of the target, and transportation to the collection chamber took about one second. This was measured by pulsing the ${}^7\text{Li}$ beam, and taking the β counts as a function of time after the ${}^7\text{Li}$ was switched off. At a ${}^7\text{Li}$ beam current of 70 pA, the ${}^6\text{He}$ was extracted at a rate of about 3×10^6 atoms/s.

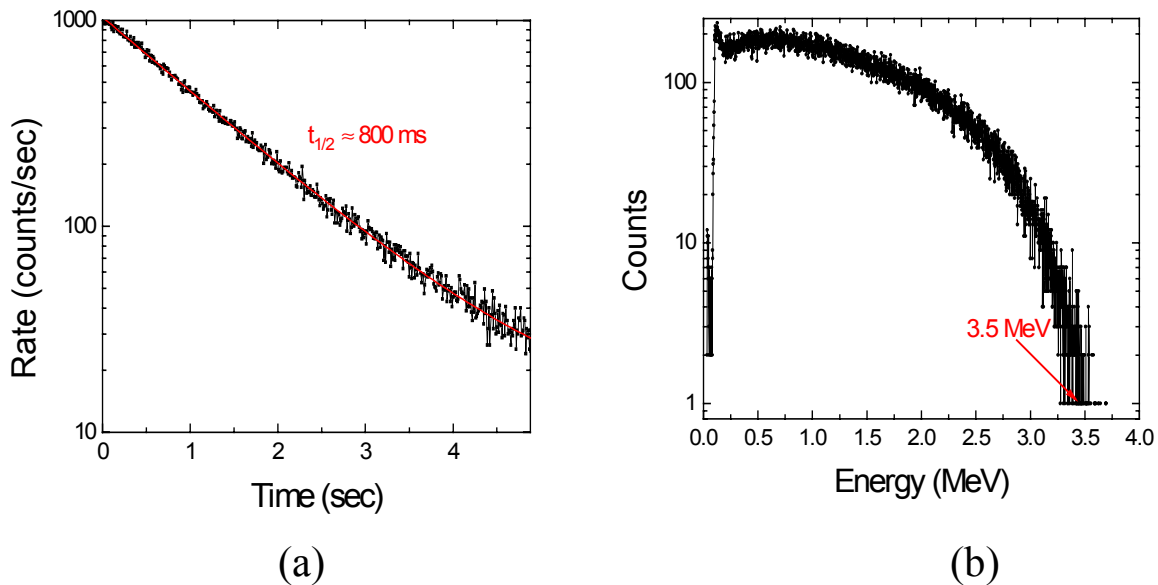


Figure 4.2: ${}^6\text{He}$ identification. (a) shows the measured decay half-life and (b) shows the end point of the β decay energy spectrum. Both measurements agree with the ${}^6\text{He}$ properties.

Chapter 5

Laser Cooling and Trapping of Metastable Helium

In this experiment, we measured the isotope shift between ^4He and ^6He in a magneto-optical trap (MOT). The unique features of the MOT provide extremely high sensitivity. Helium at room temperature has a thermal velocity of approximately 1000 m/s, which is too high to be directly captured by the MOT. Therefore, laser cooling is necessary before the atoms enter the trapping area. The Zeeman slowing technique and two-dimensional transverse cooling were used to produce an intense slow atomic beam.

All the cooling and trapping techniques rely on the spontaneous emission force, and only work for the cycling transitions of atoms. For Helium, the energy required to excite the atoms from the ground state to the first excited state ($1^1\text{S}_0-2^1\text{P}_1$) is too large (58.4 nm) for continuous narrow bandwidth laser excitation. Therefore, for practical cooling and trapping, the triplet metastable state (2^3S_1) is used, and can be excited to 2^3P or 3^3P states using commercial laser systems. The metastable helium is produced by electron collision in an RF-driven discharge. A small fraction ($\sim 10^{-5}$) of ground state helium is excited to the metastable state. Because the optical transition between triplet and singlet states is forbidden, the metastable triplet helium has a very long lifetime of 2.3 hours.

5.1 Atomic Beam of Metastable Helium

In this experiment, the metastable helium was produced by an RF-driven discharge [Chen 2001]. An RF resonator was made of a copper coil and a brass shield and was driven by an RF amplifier operating at 80 MHz. The ceramic discharge tube was 10 cm long and 1 cm in diameter. The atoms flowing through the tube, as shown in Figure 5.1, absorbed the RF power and formed discharge plasma. By collisions with the energetic electrons in the plasma, a small fraction of the helium atoms were excited to the metastable states (energy levels shown in Figure 5.2).

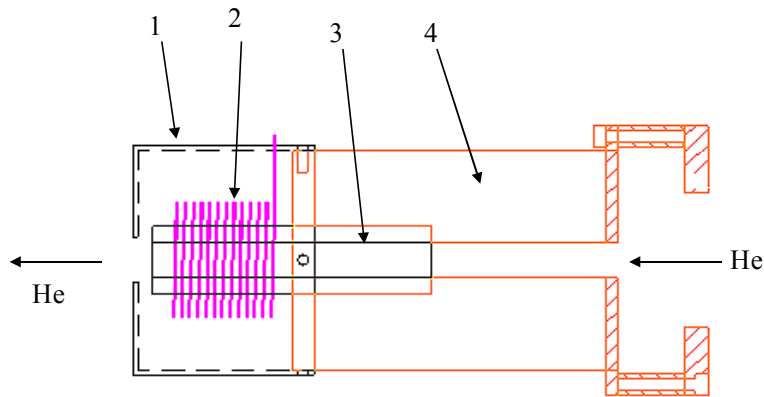


Figure 5.1: Schematic of the RF resonator and the LN₂ cooling. (1) brass shield, (2) copper wire, (3) ceramic tube, (4) stainless steel canister.

The gas pressure of the discharge must be optimized. If the pressure is too low, the electron density in the plasma is also low and the collision probability decreases. If the pressure is high, collisions with the background gas will easily quench the metastable helium. It was found that the mixture of another noble gas with lower ionization energy, Kr or Xe, increased the metastable population by more than an order of magnitude. Nevertheless, too much admixture will quench the metastable helium as well. In typical

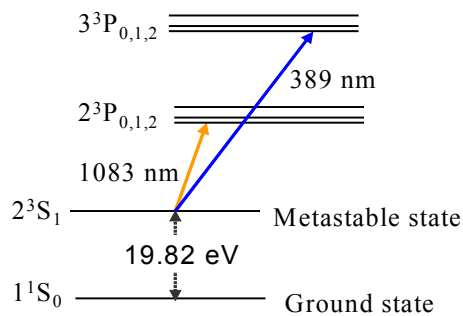


Figure 5.2: Helium energy level diagram.

running conditions, 0.5 mTorr Kr and 1 mTorr He were mixed into the source chamber, where a fraction of approximately 10^{-5} ground state helium was excited to the metastable state.

The metastable helium was then injected supersonically into the vacuum chamber. The atomic beam was diagnosed 60 cm downstream by shining a transverse laser beam with frequency tuned to the $2^3S_1-2^3P_2$ transition, and detecting the fluorescence by a

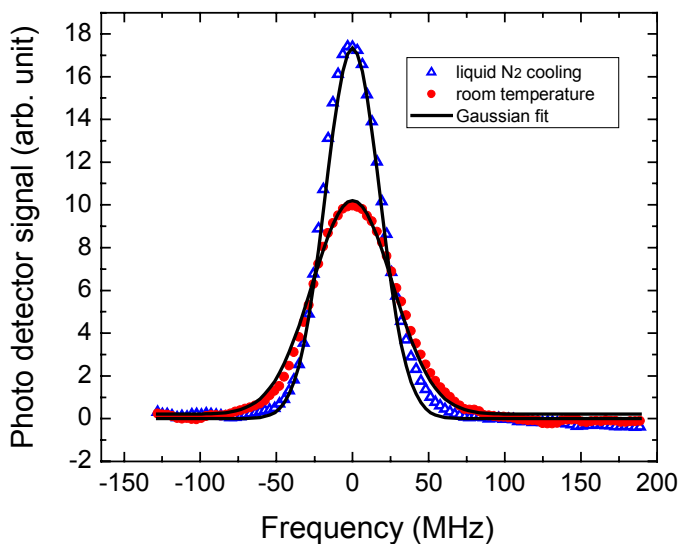


Figure 5.3: Fluorescence signal of the atomic beam with and without LN₂ cooling.

photodetector. Figure 5.3 shows the detected signal when the laser is scanned over the resonance. The divergence of the atomic beam was estimated to be 50 mrad by measuring the frequency width of the signal. The RF discharge source was also cooled by liquid nitrogen to reduce the thermal velocity of the atoms. Before the atoms entered the discharge region, they made thermal contact with the wall, which was cooled by liquid nitrogen and it decreased the most probable velocity of the atoms from 1200 m/s to 850 m/s. An angular flux density of approximately 3×10^{12} atoms/(s·sr) was produced.

5.2 Vacuum System and Gas Recirculation

The metastable helium is fragile to any collisions with background gas. Therefore, a high vacuum condition was required. Figure 5.4 shows the atomic beam line and the vacuum system. When there was no gas loading, the transverse cooling chamber and the trap

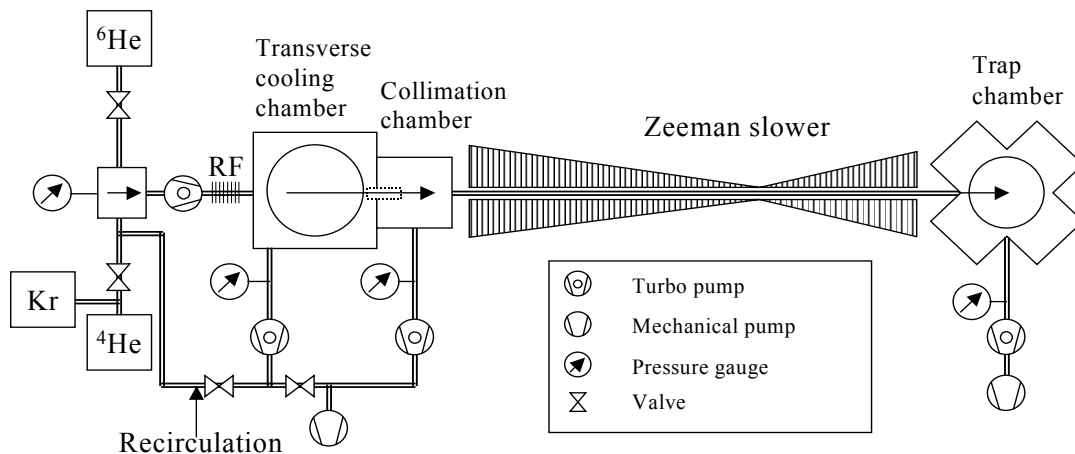


Figure 5.4: Schematic diagram of the atomic beam line and vacuum system.

chamber were both pumped down to less than 10^{-8} Torr by oil-free magnetically coupled turbo pumps. When there was gas loading, the pressure in the transverse cooling chamber was around $10^{-6} \sim 10^{-5}$ Torr, and the trap chamber is $10^{-7} \sim 10^{-8}$ Torr, depending on the gas consumption. Between the transverse cooling chamber and the trap chamber, an atomic beam collimator was installed. A 10-cm long aluminum tube with 1 cm diameter was used to block the diverging atoms, and only the central axial atomic beam could pass. This ensured the high vacuum in the trap chamber. The largest contamination of the system was from the discharge tube, in which dissociated water formed hydrogen. This contamination could be largely removed when the source was cooled with liquid nitrogen, and most of the water molecules were frozen. A getter pump was also attached to the source chamber, in which the chemically active getter material and all the contaminants formed solid, low-vapor-pressure compounds except noble gases. A residual gas analyzer was installed in the collimation chamber to monitor the gas species in the system.

Because the conductance between the transverse cooling chamber and the collimation chamber is small, most of the gases were pumped away by the turbo pump in the transverse cooling chamber, and thus were wasted. The number of atoms available was extremely small for the ${}^6\text{He}$ experiment. In order to make the most use of the precious ${}^6\text{He}$ atoms, a gas recirculation system was installed. As shown in Figure 5.4, when in recirculation mode, the outlet of the first turbo pump in the transverse cooling chamber was not connected to the mechanical pump. Instead, it went back to the source chamber. Because the ${}^6\text{He}$ has a very short half-life of 0.8 sec, an additional turbo pump was installed so that the atoms could be pumped back to the source chamber as fast as

possible. The limiting factor of this recirculation process is determined by the low conductance (~ 2 liter/s) of the discharge tube. The volume between the compression turbo pump and the discharge tube is about 0.2 liter. As a result, it took 0.1 sec for the ${}^6\text{He}$ to complete a return cycle. This implies a factor of eight increase of the system efficiency. When in recirculation mode, however, the getter pump becomes the main pumping power of the system, and the purity of the loading gas becomes even more critical. In the two ${}^6\text{He}$ experimental runs in April and May 2004, no increase of the ${}^6\text{He}$ loading rate was observed. This may be due to the gas impurity or insufficient pumping. Therefore, the gas recirculation was not used.

5.3 Transverse Cooling of an Atomic Beam

The divergence of the atomic beam was estimated to be 50 mrad. Therefore, the diameter of the atomic beam will be approximately 20 cm at the trap chamber, and the brightness of the atomic beam decreases significantly. The capture range of the trap is limited by the laser beam size, which is usually 2.5 cm in diameter. Therefore, the divergence of the atomic beam will cause a severe problem as far as the trapping efficiency is concerned. To increase the brightness of the atomic beam, two-dimensional transverse cooling was applied to reduce the divergence. The principle of the transverse cooling is based on the spontaneous emission force from the laser-atom interaction, and is described in detail in Appendix B.

In the real experiment, the transverse velocity of the atoms depends on the Maxwell distribution, and the nozzle geometry of the discharge source. When the atoms are transversely cooled, the velocity changes. The differences in the atoms' velocities

mean that a constant laser detuning frequency will not excite all the velocity groups of atoms. This problem can be solved by continuously changing the incident angle of the laser light to compensate for the change of the Doppler shift of the atoms. A zigzag configuration was used to provide the spatially changing incident angle as shown in Figure 5.5. At the beginning of the cooling, the atoms with an initial capture angle ($\theta_c = -\Delta_L / kv_L + \phi$) will “feel” the maximum deceleration, where $\Delta_L/2\pi$ is the laser detuning frequency, ϕ is the incident angle and v_L is the longitudinal velocity of the atom. As the atom’s transverse velocity slows down due to the optical molasses, the incident angle of the next coming laser light also decreases, and keeps the atoms resonant with the laser light.

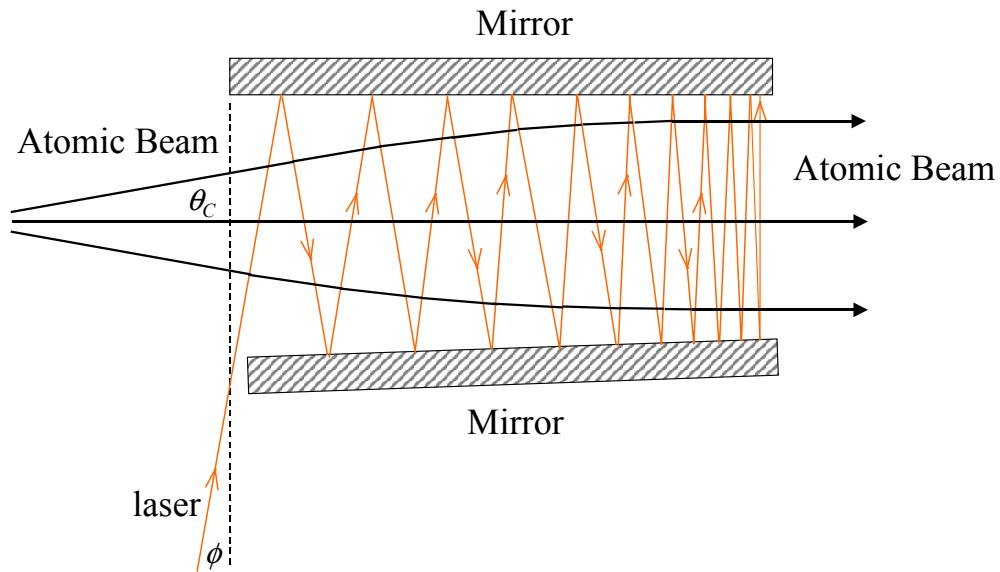


Figure 5.5: Zigzag configuration of the transverse cooling laser light.

In this experiment, the pair of mirrors was gold-coated, with an area of $10 \text{ cm} \times 2.5 \text{ cm}$. The laser beam was 2 cm in diameter, and interacted with the atomic beam

immediately after the discharge source. The detuning of the laser frequency was about 0 to -0.5Γ . Figure 5.6 shows the increase of the atomic beam brightness in the trap chamber by detecting the fluorescence induced by a laser beam tuned to the $2^3S_1-3^3P_2$ transition at 389 nm. The transverse cooling increased the trap loading rate by approximately a factor of eight.

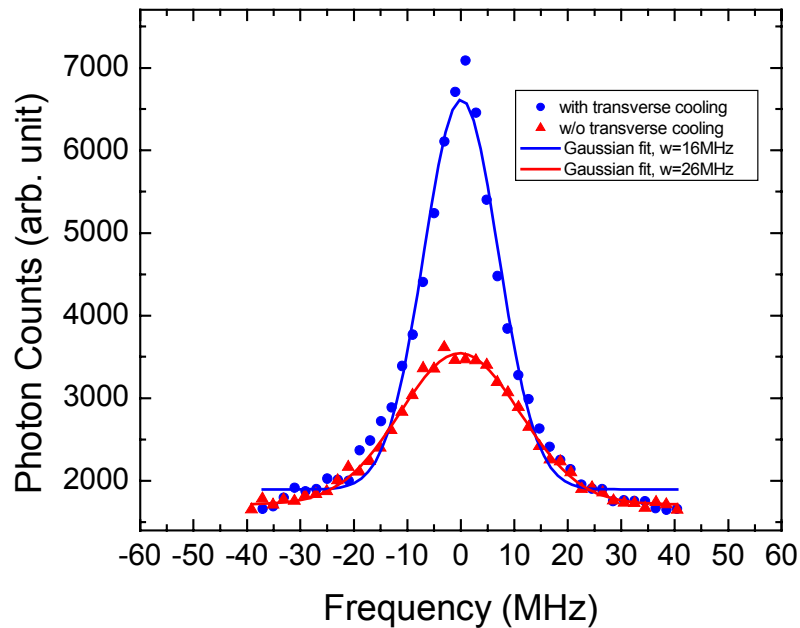


Figure 5.6: Atomic beam fluorescence in the trap chamber. The width is reduced from 26 MHz to 16 MHz after transverse cooling.

5.4 Deceleration of an Atomic Beam

The atoms must be slow enough to be captured in the MOT. For a typical MOT, the capture velocity is less than 50 m/s, and only several ppm of the ^4He atoms at room temperature can be captured and trapped. Therefore, a slow (< 50 m/s) metastable helium beam must be produced.

The deceleration of the atomic beam was achieved by laser cooling on the cycling $2^3S_1-2^3P_2$ transition at 1083 nm with Zeeman slowing technique (see Appendix B). The Zeeman slower, two water-cooled solenoids that consisted of many layers of wires of varying lengths, provided the necessary magnetic field so that the Zeeman shift could compensate the changing Doppler shift when the atoms slowed down. The laser was therefore always on resonance with the moving atoms, and provided the maximum deceleration. The parameters of the Zeeman slower are shown in Table. 5.1. The designed and mapped magnetic field is shown in Figure 5.7.

Table 5.1: Characteristics of the Zeeman slower.

	Solenoid 1	Solenoid 2
Length (cm)	122	40
Number of layers	30	30
Current (A)	1.26	-0.98
Maximum B field (Gauss)	295	-314
Laser detuning, $\Delta_L/2\pi$ (MHz)	-440	-440
Capture velocity, v_i (m/s)	925	
Final velocity, v_f (m/s)		20

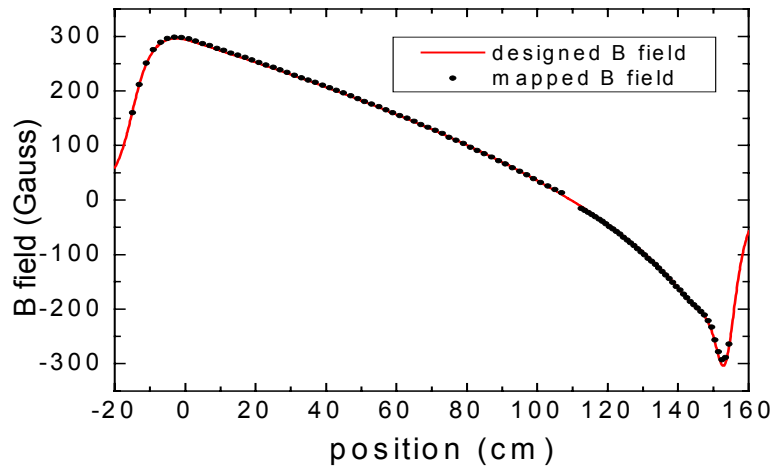


Figure 5.7: Magnetic field of the Zeeman slower as a function of position along the atomic beam axis.

For switching between ^4He and ^6He , the current settings and the laser detuning are not changed assuming the same capture velocity is used in both cases. For the same laser intensity, however, the slowing distance is longer in the case of ^6He than ^4He due to the larger mass of ^6He . To keep the Zeeman slower physically unchanged, higher laser intensity is needed for ^6He . While $I = 1.5 I_s$ is used for ^4He , $I = 9 I_s$ is needed for ^6He . Here I_s is the saturation intensity as defined in Appendix B.

5.5 Magneto-Optical Trap

The magneto-optical trap (MOT) [Raab, 1987] is the most widely used trap, which utilizes both the laser light, and magnetic field. The basic idea is that the inhomogeneous magnetic field together with the laser light provides the spatial confinement, and the viscous force from the radiation pressure damps the atoms to lower temperature. The MOT consists of a magnetic quadrupole to provide the field gradient at the center of the trap, and three pairs of counter-propagating laser beams in a $\sigma^+ - \sigma^-$ configuration as shown in Figure 5.8.

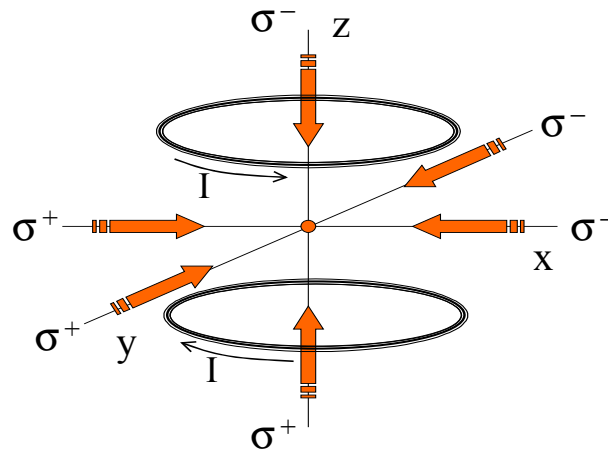


Figure 5.8: Three-dimensional MOT. The quadrupole field is produced by the anti-Helmholtz coils.

In this experiment, the constant B field gradient was produced by a pair of anti-Helmholtz coils made of copper tubing, and cooled by water. The magnetic field of the coils with current I , identical radius r , and separated by distance d can be written using the following formula, and the field used in this experiment is plotted in Figure 5.9.

$$B_{vertical}(z) = \left(\frac{\mu_0 I}{2r}\right) \left\{ \left[\frac{r^2}{\left(z - \frac{d}{2}\right)^2 + r^2} \right]^{3/2} - \left[\frac{r^2}{\left(z + \frac{d}{2}\right)^2 + r^2} \right]^{3/2} \right\} \quad (5.1)$$

$$B_{radial}(x) = \left(\frac{\mu_0 I d r}{4\pi}\right) \int_0^{2\pi} \sin(\theta) \left[r^2 + x^2 + \frac{d^2}{4} - 2xr \sin(\theta) \right]^{-3/2} d\theta.$$

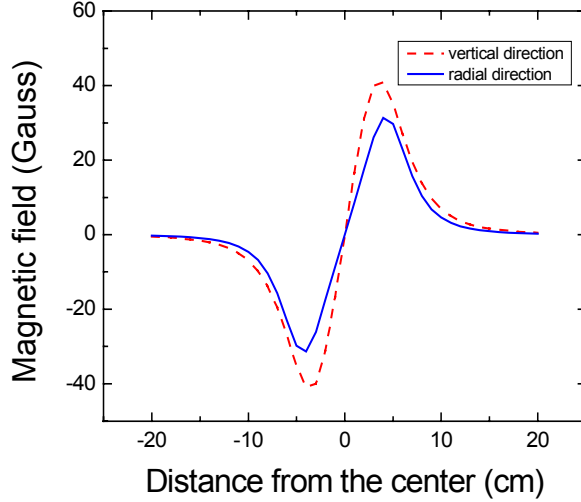


Figure 5.9: MOT magnetic field profile along the vertical and radial direction at current $I = 40$ A.

At the center of the trap, the B field must be zero, and two trim coils were used for fine adjustment of the B field, and control of the trap position. In addition, one compensation coil at the end of the atomic beam line was used to compensate the strong B field produced by the Zeeman slower. The trapping laser beam was approximately 2.5

cm in diameter, and had an intensity of 11 mW/cm^2 , ($70 I_s$). The detuning of the trapping light was -20 MHz (-12Γ) relative to the $2^3S_1-2^3P_2$ transition.

5.6 Detection of Trapped Atoms

When probed by a resonant light, the fluorescence of the trapped atoms can be detected by a CCD camera. To quantitatively measure the number of atoms in the trap, we used a photodiode detector with a current-to-voltage gain of 10^8 . The voltage output is thus proportional to the number of atoms:

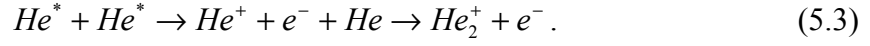
$$V_{out} = \left[\frac{\Gamma s}{2(1+s)} \right] \times \left[\frac{\Omega}{4\pi} \varepsilon \right] \times [\eta e] \times N_{atoms} \times \frac{\Gamma_{laser}}{\Gamma_{trap}}, \quad (5.2)$$

$\downarrow \qquad \downarrow \qquad \downarrow \qquad \downarrow$
 scattering rate efficiency gain fraction of atoms probed

where the scattering rate is the photon emission rate per atom. The detection efficiency includes the solid angle Ω and the photon-diode quantum efficiency ε . The quantity η is the current to voltage gain, and e is the electric charge. Since the width of the spectroscopic feature (several MHz) is usually larger than the laser linewidth ($< 1 \text{ MHz}$), the laser only probes a fraction of the atoms. As a result, the ratio of the two widths must be included.

The number of atoms in the trap is determined by the loading rate and trap loss rate. When the trap is small, the loss rate is mainly due to the collisions between the trapped atoms and the background thermal atoms. Because the trap depth is shallow, the elastic collision with hot atoms will knock the cooled atoms out of the trap. Besides, the metastable helium atoms carry an internal energy of 19 eV , and will ionize the background atoms when they make inelastic collisions. Another mechanism that causes

the loss of trapped atoms is the interaction between the metastable atoms. The Penning ionization is the main process:



Combining the two effects, the number of trapped atoms is governed by the following equation:

$$\frac{dN}{dt} = L - \alpha N - \beta N^2 , \quad (5.4)$$

where L is the loading rate, and α, β are the coefficients of the two loss mechanisms. In a steady state when the number of trapped atoms reaches the maximum and presumably the trap is small so that the collisional loss rate between two trapped atoms is negligible, then the loading rate becomes $L = \alpha N$. The value of α can be determined by stopping the helium loading (*e.g.* blocking the slowing light), and measuring the trap decay. Figure 5.10 shows the typical decay curve of the trap. From a fit to the exponential decay time constant τ , one may determine the collision coefficient $\alpha = 1/\tau$ and the loading rate $L = \alpha N$ where N is the steady-state number of atoms. The maximum ^4He loading rate achieved in this experiment was about 10^9 atoms/s.

Combining the trap loading rate and the gas consumption rate, which was deduced from the pressure and the pumping speed of the system, one could then derive the overall trapping efficiency. The operation condition for best efficiency was different from that for a trap with the largest number of atoms, and was achieved when the helium pressure was very low at the source chamber, where the discharge was only maintained by krypton. The efficiency was about 2×10^{-8} . If we assume the same trapping efficiency

for ^4He and ^6He , we may expect to detect 200 ^6He atoms per hour if the ^6He extraction rate is 3×10^6 atoms/s.

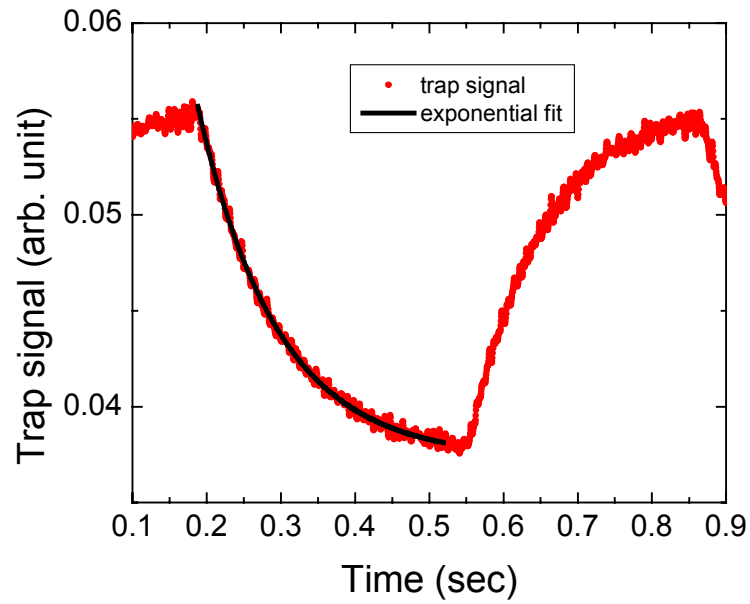


Figure 5.10: Decay of the trapped atoms due to collisions. The lifetime was determined from these data to be approximately 110 ms.

Chapter 6

Laser Spectroscopy of Trapped Atoms

The advantage of using trapped atoms for precision spectroscopy is two-fold. First, the atoms in the trap are cold, and the Doppler width is largely reduced. Second, the long observation time of the trap increases the signal-to-noise ratio significantly, and enables us to detect rare species.

For helium spectroscopy, the laser induced fluorescence detection is a sensitive method. With careful suppression of the scattering light, and shielding of the room light, the trap method is capable of detecting a single atom, and thus a powerful tool for rare isotope detection. In this experiment, the trapping used the $2^3S_1-2^3P_2$ cycling transition at 1083 nm, while the spectroscopy was performed on the $2^3S_1-3^3P_2$ transition at 389 nm to take advantage of the high sensitivity of detecting blue photons.

The long observation time of the trapped atom enabled us to obtain high photon statistics from a single atom. However, the long probing time and repeated scatter of photons inevitably disturbed the atom's velocity distribution. It resulted in a heating and cooling process, which caused asymmetry of the line shape. For a light atom like helium, the absorption of a single photon will change the atom's velocity and cause a Doppler shift of hundreds of kHz. This effect on the determination of the line center and the probing strategy to eliminate this systematic effect are discussed in this chapter.

6.1 Laser Induced Fluorescence Detection

The fluorescence detection method provides a higher signal to background than the absorption method, however, at the cost of small collection efficiency of the fluorescence light. A lens is installed inside the vacuum as close to the trap center as possible until it interfered with the trapping light. About 2% of the solid angle was collected. For a large ^4He trap, the fluorescence was then focused onto a photodiode detector, in which the photocurrent is converted to the voltage output by a resistor R . The dominant noise is the Johnson noise from electron's thermal movement, which scales as $(Rk_B T)^{1/2}$, where k_B is the Boltzman constant, and T is the temperature. Since the gain is proportional to the coupling resistance R , the larger resistance will lead to a better signal to noise ratio. Typically, a resistor of 10^8 ohm was used. The photodiode, (UDT, 10DP/SB) is sensitive to both 1083 nm and 389 nm with quantum efficiency of about 15%. When the number of atoms in the trap is small, the room light and the scattering light become a sizeable background noise. A light-tight box, an aperture, and a blue filter were used to decrease the background scattering light and the room light as shown in Figure 6.1. To further reduce the scattering light, the trap chamber was painted black inside by a vacuum-compatible material (AZ Technology, MLS-85SB).

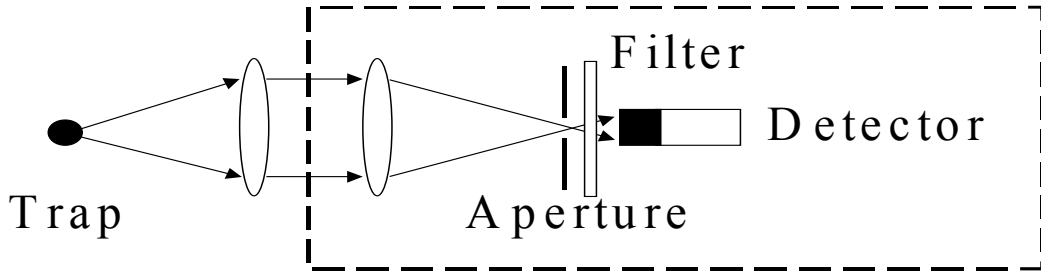


Figure 6.1: Imaging system for single atom detection. The detector is inside a light-tight box.

6.2 Single Atom Detection

The loading rate of ${}^6\text{He}$ into the trap was about $10^{-2}/\text{s}$, and the trap lifetime was less than one second. As a result, the ${}^6\text{He}$ atoms would not accumulate, and there was usually at most one atom captured in the trap. To detect a single atom, we take advantage of the atom trap trace analysis (ATTA) technique [Chen, 1999], which was developed by our group, and proved to be virtually background-free. A photomultiplier tube (Electron Tubes P10PC) with single photon counting capability was used to detect the fluorescence from a single atom. The PMT has a built-in high voltage supply, pulse amplifier and discriminator. The quantum efficiency at 389 nm is 25%, and drops very quickly to almost zero at 1083 nm. This feature enables us to perform precision spectroscopy at 389 nm without background noise from the trapping light. A detected photon was converted to a TTL signal with pulse-width of 10 ns. The output TTL signal was then sent into a pulse generator, (LeCroy Dual Gate Generator Model 222) which had a blanking function to block the pulse generation. When the blank input was high, the output of pulse was inhibited. The width of the output pulse was adjusted to be typically tens of μs . The blanking function enabled us to read the data synchronously with the gate of the blank input. This is important when we chop the trapping light and shutter the atomic beam, which will be described in the next section.

The shaped photon pulses were then sent to a PCI counter board, (National Instrument PCI 6602), which directly counted the number of pulses in a specific period of time, and the photon counting rate could be determined. Without any light exposure, the PMT had a dark count rate of about 20 cps (counts per second). The room light and the scattering of the blue light due to multiple reflections off the vacuum windows

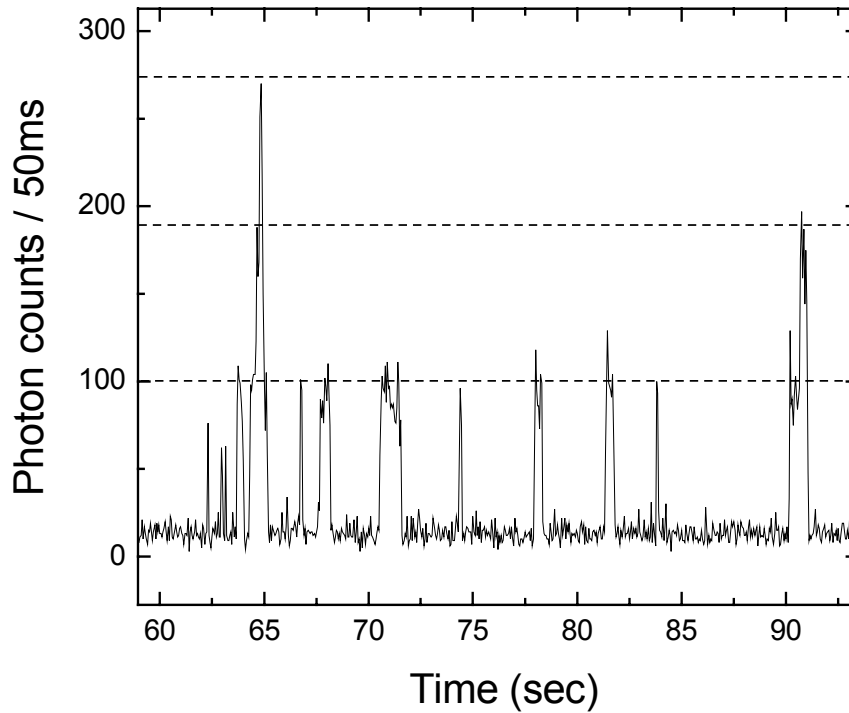


Figure 6.2: Single atom signal of ^4He . The photon count of a single atom is more than 1.5 kHz.

contributed 200 ~ 300 cps after careful shielding by installing light baffles. When one atom was trapped, a pair of counter-propagating laser beams tuned to the resonant frequency at 389 nm induced fluorescence, and thus the photon count rate increased. Figure 6.2 shows a typical ^4He single atom signal. The loading of one, two and three atoms into the trap can be clearly identified. The average lifetime of the ^4He atoms in the trap was approximately 0.6 sec, which was limited by the background gas collision. The signal of one single atom was approximately 80 photon counts in 50 ms integration time. The background was about 15 counts and the fluctuation of the background was mainly statistical. Therefore, a signal to noise ratio of about 20 was achieved. To achieve a single

atom signal of ^4He , one must reduce the helium loading rate by decreasing the helium gas flow. The main gas species in the source chamber and trap chamber was krypton, which was used to maintain the discharge. Therefore, the lifetime of the trap was mainly determined by background gas collisions because two-body collisions between two metastable atoms were absent for a single atom. To increase the lifetime of the trap, a shutter was installed at the beginning of the Zeeman slower. The shutter (UNI BLITZ D122), controlled by a TTL signal, could be opened or closed within 1 ms. When it was closed, it blocked the atomic beam and increased the lifetime of the trapped atoms. The TTL control signal of the shutter originated from the photon burst signal. An integrator circuit integrated the photon pulses from the PMT output, and converted it into a voltage output. One could define the existence of the single atom in the trap by properly setting the threshold of the integrator output. When the integrator output was larger than the threshold, it indicated one atom was detected, and the shutter was immediately closed. As a result, the lifetime of the atom in the trap could be as long as one second.

6.3 Light Shift and Zeeman Shift

The resonant light that drives the atomic transitions actually shifts the atomic energy levels. Because of the presence of the laser light field, the original atomic levels are no longer the eigenstates of the new Hamiltonian. As a result, a shift of atomic energy levels will occur. The transitions we use for trapping ($2^3\text{S}_1-2^3\text{P}_2$) and spectroscopy ($2^3\text{S}_1-3^3\text{P}_2$) share a common ground state. Because the trapping light was red-detuned, it caused the “light shift” for the common ground state, and thus affected the $2^3\text{S}_1-3^3\text{P}_2$ transition for

the spectroscopic measurement. When the trapping laser is red-detuned $-\Delta_L$, the shift of the ground state energy can be expressed as

$$\Delta E_g = (-\Delta_L + \sqrt{\Omega^2 + \Delta_L^2})\hbar / 2, \text{ where } \Omega^2 = s\Gamma^2 / 2 \text{ is the Rabi frequency.} \quad (6.1)$$

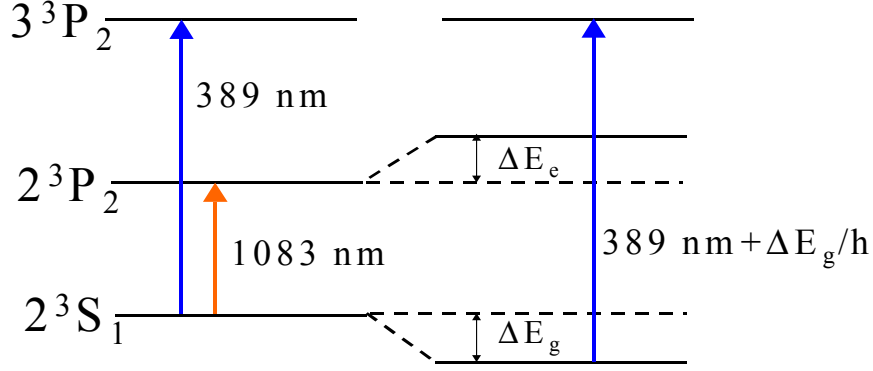


Figure 6.3: Illustration of the light shift. The quantity, ΔE is the energy shift for both the ground and excited states.

For the three-dimensional counter-propagating trapping light with -20 MHz detuning and $70 I_s$ intensity, the shift could be as much as 5 MHz. This shift is difficult to calibrate and subtract in a controlled manner because the intensity of the trapping laser is not uniform when it forms a standing wave. Since the light shift depends on the detuning of the trapping light, we also required precise frequency control of the trapping laser in addition to the spectroscopy laser. Another light shift arises from the slowing light. Although it is far detuned, it can still cause a shift of the order of 50 kHz.

One way to eliminate the uncertainty from the light shift is to shut off the trapping light and slowing light when performing spectroscopic measurement. The trapping light was chopped at 100 kHz with $1:4$ probing and re-trapping duty cycles by a fast switching AOM. When the trapping light was off, the atoms would expand with an initial velocity

of about 1 m/s, (the temperature of the atoms in the MOT is about 1 mK). The trapping light was turned back on quickly so that the atom did not travel too far, and could be trapped again. If the chopping speed is of the order of several kHz, the travel distance is less than 1 mm, and the atoms can be trapped again with almost 100% efficiency. No reduced trap lifetime was found due to the chopping of the trapping light. The detection gate was on only when the trapping light was off. The reason for fast chopping up to 100 kHz is to eliminate the atom's motional effect due to the probing process, and will be described in detail in the next section. The trapping and detection sequences are shown in Figure 6.4. In addition, the slowing light was turned off when the atom was detected in the trap. This was triggered by the atom identification integrator as mentioned in section 6.2. A liquid crystal changed the polarization of the slowing light before it passed a polarization beam splitter cube.

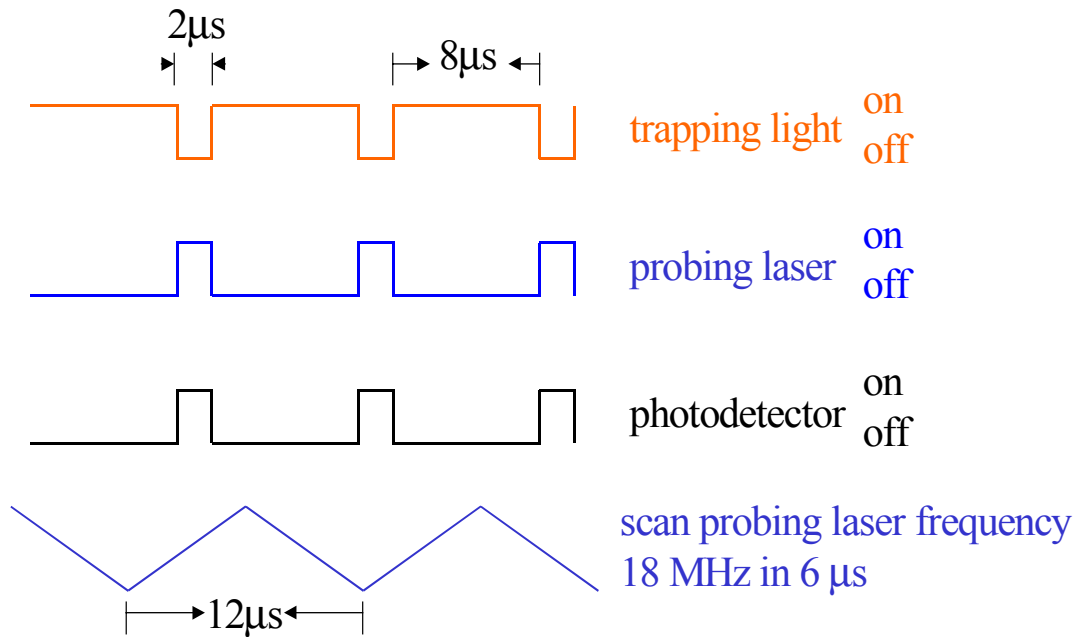


Figure 6.4: Sequence and timing of the chopping and detection gates.

6.4 Motional Effect of Trapped Atoms

When performing spectroscopy on trapped atoms, one immediately encounters a problem that the probing process actually changes the velocity distribution of the atoms. When the probe laser is red-detuned, it helps cool the atoms; when it is blue-detuned, it provides heating. The cooling and heating process will cause asymmetries of the line shape, and the determination of the line center becomes difficult. Since a single photon kick will cause velocity change of the ^4He atom by as much as 0.25 m/s, which corresponds to a Doppler shift of 660 kHz, it will cause a sizeable effect on the isotope shift measurement because ^6He has different mass, and the recoil due to the photon kick is different (440 kHz for ^6He).

Figure 6.5 shows a slow frequency scan across the ^4He resonance. When the probe power is high (about saturation intensity), the asymmetry of the line shape can shift the line center by as much as 5 MHz. One simple solution to solve the problem is to use a

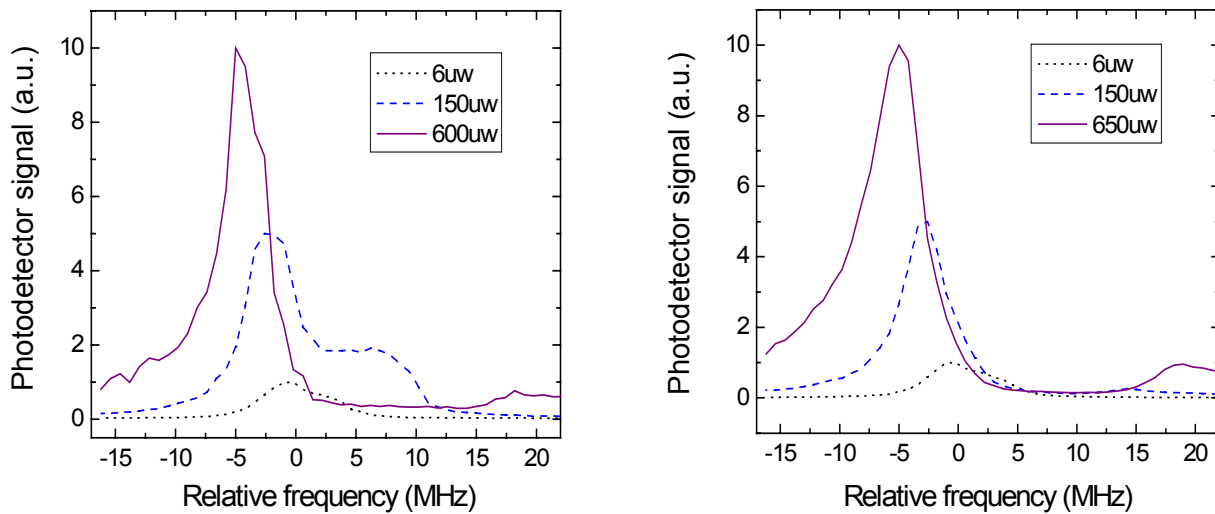


Figure 6.5: Trap fluorescence by slowly scanning the blue laser frequency for different blue laser power. Left: trap laser light detuning $\Delta_L/2\pi = -20$ MHz, intensity $I = 70 I_s$. Right: $\Delta_L/2\pi = -3$ MHz, intensity $I = 5 I_s$.

very weak probe light, so that the disturbance from the probing process is largely reduced. However, this will also decrease the photon scattering rate of the atom, and we will not collect enough photon statistics for the ${}^6\text{He}$ measurement.

To solve the problem, various probing and cooling periods, duty cycle, and scanning speed of the laser frequency were investigated. The probing time should be as short as possible, so that an atom usually scattered less than one photon in that period. After the probing period, the atom was cooled by the trapping light to get back to the initial thermal distribution. As shown in Figure 6.4, the probing and cooling time were 2 μs and 8 μs , respectively. To make the cooling more efficient in the 8 μs period, the detuning frequency of the trapping light was changed from -20 MHz to -3 MHz, and the intensity was decreased from $70 I_s$ to $5 I_s$ once the atom was detected in the trap. In addition, the scanning speed of the probe laser frequency should be fast compared to the time scale of the atom's motional effect. As a result, only the internal degree of freedom was excited while the external motion of the atom was not changed. Typically, 18 MHz was scanned linearly in 6 μs , and the scanning ramp generated by a function generator was in random phase with the trapping light chopper.

Furthermore, in order to minimize the motional effect, two counter-propagating probe beams were employed so that the force from the two probe beams cancelled. The balance and alignment of the two probe laser beams were critical in order to totally remove the atom's motional effect, and were achieved by gentle focusing of the reflection laser beam until the position of the resonance line center had no power dependence (see Chapter 8 for discussion about systematic effects). Figure 6.6 shows a typical scan with a few ${}^4\text{He}$ atoms in the trap. The line shape was symmetric with a linewidth of about 7

MHz (FWHM), and no systematic effect between the frequency scanning up and scanning down was observed.

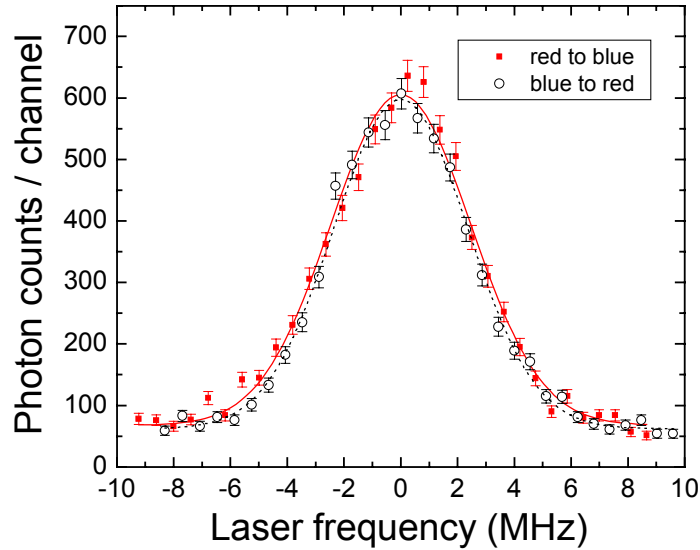


Figure 6.6: Frequency scan from red to blue and blue to red side of the resonance. No asymmetry was observed.

6.5 Determination of the Resonance Line Center

In the MOT, the atoms are cooled below 1 mK, which corresponds to a Doppler width smaller than 8.7 MHz for ^4He . Without further cooling, the Doppler effect is still the dominant source of the line broadening, compared with the natural linewidth of 1.5 MHz, and laser linewidth smaller than 0.5 MHz. To more precisely determine the velocity distribution of the trap, a very weak ($I \sim 0.01 I_s$) probe laser was used on a few hundreds of atoms in the trap, so that the power broadening and the heating effect due to the probing process were negligible. As shown in Figure 6.7, the Gaussian linewidth (FWHM) in the low laser intensity case was 4.8 MHz. Therefore, the temperature of the

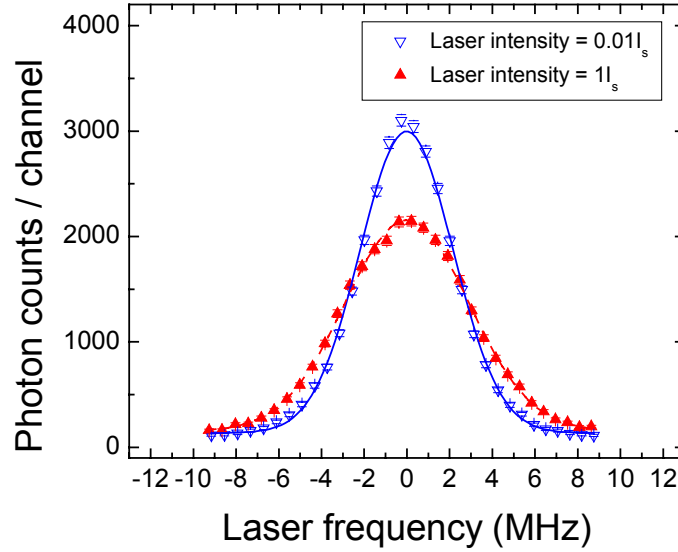


Figure 6.7: The linewidth decreases from 7 MHz to 4.8 MHz by using very weak probe laser power.

trap was estimated to be $300 \mu\text{K}$, a factor of seven larger than the Doppler cooling limit. When the intensity of the probe laser was high, the linewidth increased to 7 MHz, which was mainly due to the heating of the trapped atoms and some small contribution from the power broadening effect.

In the real fitting process, the difference between the Gaussian and the Voigt profile was small ($\sim 1 \text{ kHz}$). The broadening of the line shape does not move the position of the line center because of the symmetric line shape. The precision one can achieve in determining the line center depends on the linewidth, which is $\delta\omega = \Delta\omega/(S/N)$, where $\delta\omega$ is the uncertainty in determining the line center, $\Delta\omega$ is the width of the peak, and S/N is the signal to noise ratio. If the width is 6 MHz, and the $S/N = 5$ for a single atom, one will require ~ 150 atoms to make a 100 kHz measurement, which is the typical case in this experiment.

Chapter 7

Laser System and Data Acquisition

For both trapping and spectroscopy, a tunable laser light source with narrow linewidth is required. In this experiment, external-cavity diode lasers were used in producing both the 1083 nm and 389 nm laser light. The 1083 nm laser light from the diode laser was amplified by a fiber amplifier in order to produce the necessary laser power for trapping, slowing and transverse cooling. The 389 nm light was generated by frequency doubling of the 778 nm light. This enabled us to perform the frequency control and stabilization in the near-IR region, which was easily accessed by using a diode laser.

Each transition employed two lasers. One served as a frequency reference, and the frequency was locked to atomic transitions. The second laser was used for the experiment, and its optical beat frequency to the first laser was monitored by a fast photodetector. Because the beat frequency could be measured very precisely (uncertainty < 1 kHz), the ultimate limitation of the frequency control was the lock quality of the reference laser. For the 1083 nm laser setup, the reference laser was locked to the $2^3S_1-2^3P_2$ transition in a discharge helium gas cell. For the 389 nm laser setup, the frequency control was performed at the fundamental wavelength 778 nm by locking the reference laser to an iodine molecule transition. The details of the laser setup and frequency control are discussed in this chapter.

7.1 Laser Setup for Trapping and Cooling at 1083 nm

Semiconductor diode lasers have been widely used for atomic physics research since the early 1990's. Because of its narrow linewidth, easy tunability, compact design and low cost, it is a great tool for visible and near-IR spectroscopy where laser diodes for these wavelengths are commercially available. The details of the design of the external cavity, grating feedback and the temperature control are well described in [Weiman, 1991], and will not be discussed here. All the diode lasers in this experiment use the Littrow configuration.

The laser diodes at 1083 nm were from Toptica, Model LD-1083-0075 with maximum output power of 80 mW. Two diode lasers at 1083 nm were used. The first one (DL1) was locked to a transmission peak of a high-finesse Fabry-Perot interferometer (FPI). The frequency of DL1 was modulated at 20 kHz by current control. The transmission signal of the FPI was detected by a photodiode detector and sent to a lock-in amplifier. The schematic of the laser setup is shown in Figure 7.1. The error signal produced by the lock-in amplifier was sent to a proportional and integral (PI) amplifier circuit and then served as a feedback to control the laser frequency. The proportional part was sent to the current input of the laser diode as a fast feedback. The integral part was applied to the PZT to control the grating as a slower feedback. The bandwidth of this servo-loop was about 1 kHz. The length of the FPI was stabilized to a saturation absorption peak in a helium gas. Figure 7.2(a) shows the frequency scan over the ^4He resonance. The saturation absorption signal was sent to another lock-in amplifier, and the output of the lock-in amplifier following similar PI circuit was used as a feedback to the

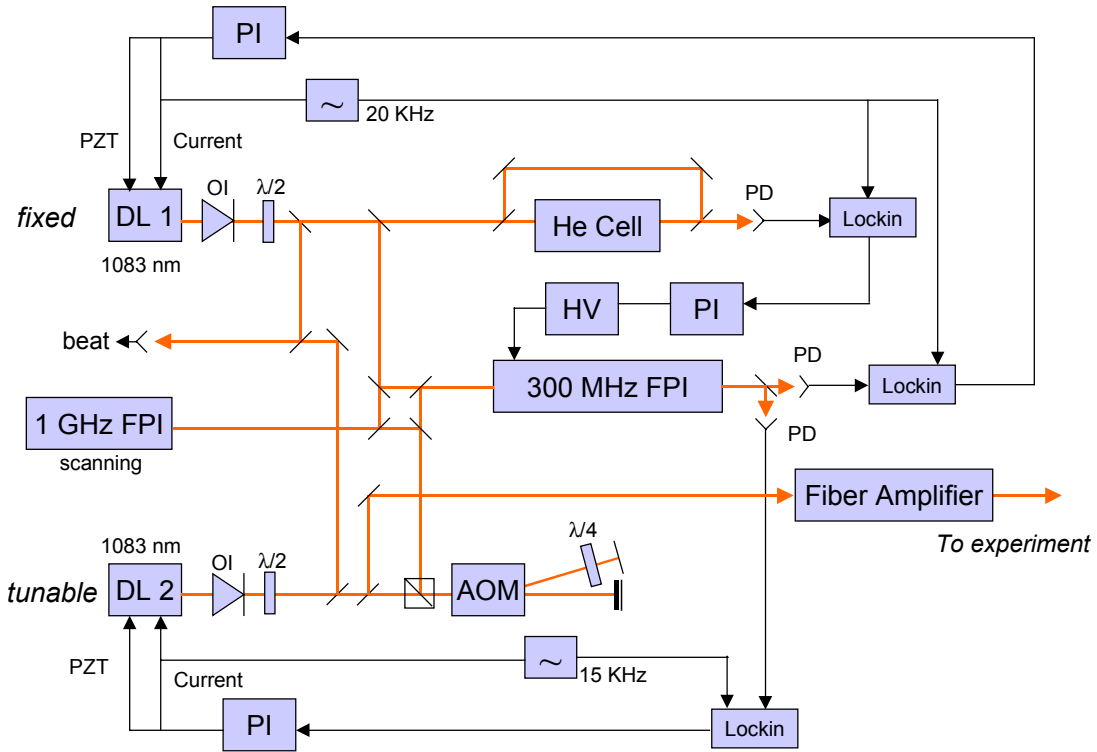


Figure 7.1: The 1083 nm laser frequency lock and control system. DL1 and DL2: diode lasers; FPI: Fabry-Perot interferometer; HV: high voltage power supply; PD: photodiode detector; PI: proportional and integral feedback circuit; OI: optical isolator; AOM: acousto-optical modulator; $\lambda/2$ and $\lambda/4$: half and quarter wave plates.

applied voltage of a ceramic PZT to control the length of the FPI. Figure 7.2(b) shows the feedback signal from the lock-in amplifier. The bandwidth of this loop was about 100 Hz.

The second 1083 nm diode laser (DL2) was frequency shifted by a doubly-passed acousto-optic modulator (AOM), and then locked to the same FPI as DL1. By changing the AOM RF frequency, DL2 then became tunable. The zero-order output of DL2 after the AOM was used for the experiment. In order to determine the absolute frequency difference between DL1 and DL2, partial beams from both DL1 and DL2 were combined and sent into a fast (6 GHz) photodiode detector. By measuring the beat frequency using

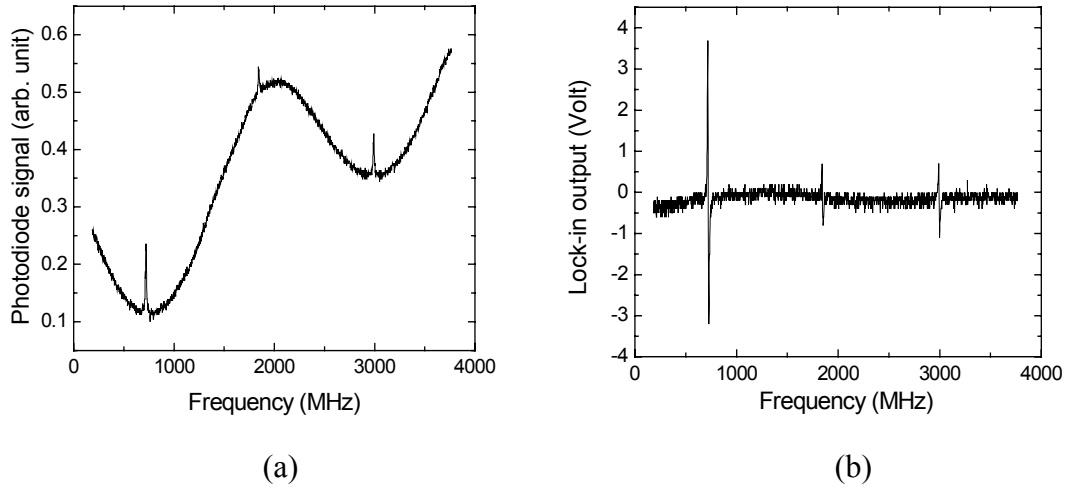


Figure 7.2: (a) Saturation absorption peak in the discharge gas cell. The peaks are the $2^3S_1-2^3P_{1,2}$ transitions and the cross-over. (b) The corresponding error signal from the lock-in amplifier.

a frequency counter or a spectrum analyzer, the frequency difference between DL1 and DL2 can be measured precisely.

The partial beam of DL2 was also sent into a Yb-doped fiber amplifier (Keopsys, YFA-10FA) to produce enough laser power for this experiment. The input power of the fiber amplifier from the seed laser DL2 was about 1 mW, which was enough to saturate the amplifier. The amplifier works in constant-output mode, so the output power is independent of the input level, which is convenient for our experiment. Furthermore, the output of the amplifier is fiber-coupled in order to minimize beam steering when we switch between the isotopes. The output from the fiber is a Gaussian beam with a waist of about one mm. The output fiber is not polarization preserving. Two wave plates ($\lambda/4$ and $\lambda/2$) were placed right after the amplifier output to maintain the polarization, which might slightly change from day to day due to the temperature fluctuation and the stress on the fiber. The output of the fiber amplifier was then distributed and frequency shifted for

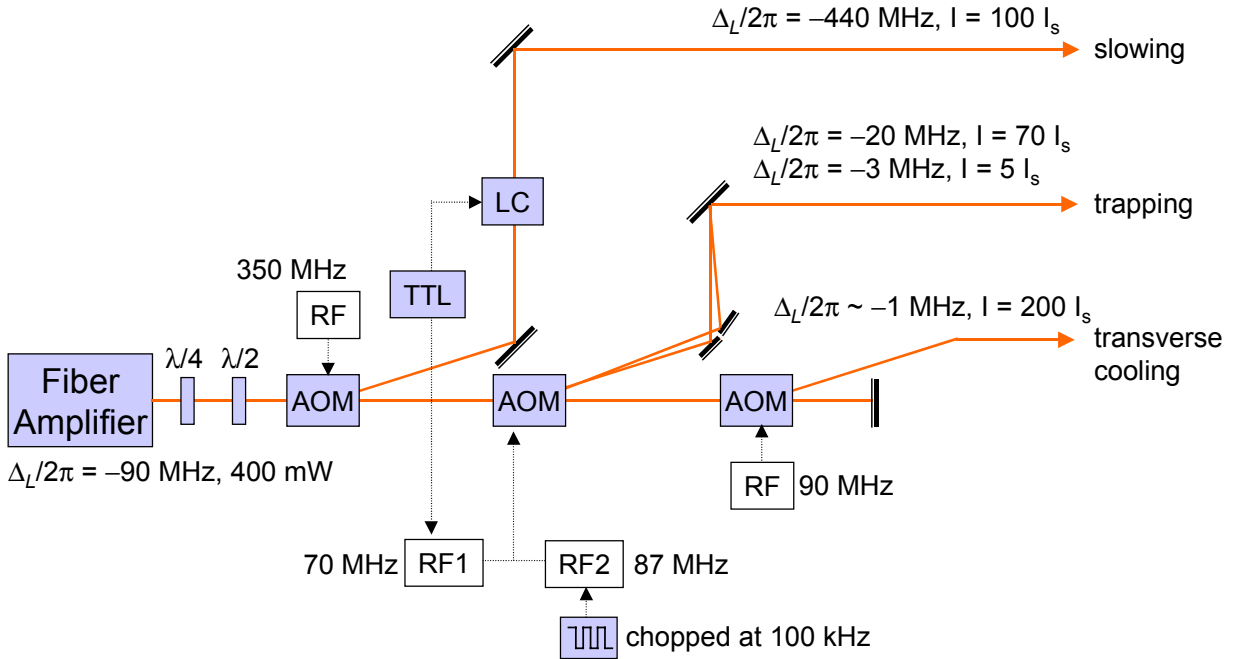


Figure 7.3: Distribution of the laser power for trapping, slowing, and transverse cooling. RF: radio frequency generator and amplifier; TTL: signal from atom identification circuit; LC: liquid crystal; $\lambda/4$ and $\lambda/2$: quarter and half wave plates.

slowing, trapping, and transverse cooling by beam splitters and three AOMs as shown in Figure 7.3.

As mentioned in Chapter 6, the trapping light was chopped at 100 kHz to avoid the light shift for the spectroscopic measurement. This was achieved by a fast RF switch (Mini-Circuits ZYSW-2-50DR), which was controlled by a 100 kHz TTL signal from a function generator. As a result, the trapping light could be turned on and off within 100 ns. In addition, in the spectroscopy mode, the trapping light for the “hot trap” ($\Delta_L/2\pi = -20$ MHz, $I = 70 I_s$) was turned off within 5 μ s by the TTL signal from the atom identifying electronics (see Chapter 6) using another RF switch (Mini-Circuits ZMSW-1211).

7.2 Laser Setup for Precision Spectroscopy at 389 nm

Diode lasers below 400 nm are becoming commercially available, but the availability is very limited. Therefore, we decided to find another solution to provide the blue light at 389 nm. We chose to double the frequency of 778 nm light using a nonlinear crystal to produce the 389 nm blue radiation. The advantage is that the precision frequency control can be performed in the near-IR, where semiconductor lasers are available at low cost. The method of generating the frequency-doubled light is described in Appendix C.

The frequency control of the 778 nm lasers is of critical importance in this experiment. Due to mass production of the CD writer in which the diode laser works at 780 nm, high power laser diodes are available at low cost. We used a Sharp laser (Model GH078JA2C), which has a maximum output power of 120 mW. The frequency control was similar to that of the 1083 nm lasers. Two diode lasers were used: one served as the frequency reference while the other one was tunable. The frequency difference was monitored by measuring the beat frequency between the two lasers. The schematic of the laser system is shown in Figure 7.4. DL1 (the frequency standard) and the DL2 (tunable) were both frequency-stabilized to a Fabry-Perot interferometer (FPI). In order to increase the bandwidth of the feedback loop, the Pound-Drever-Hall locking technique was used [Drever, 1983]. Partial beams of DL1 and DL2 were sent into two separate electro-optical modulators (EOM), modulated at 15 MHz and 20 MHz, respectively. After the EOM, DL1 and the first-order diffraction output of DL2 after a doubly-passed AOM were coupled to the same FPI with a free spectra range of 600 MHz, and a finesse of 200. The reflected light of both DL1 and DL2 from the FPI was detected using a fast photodiode (bandwidth > 300 MHz). The signal from the photodiode detector was then demodulated

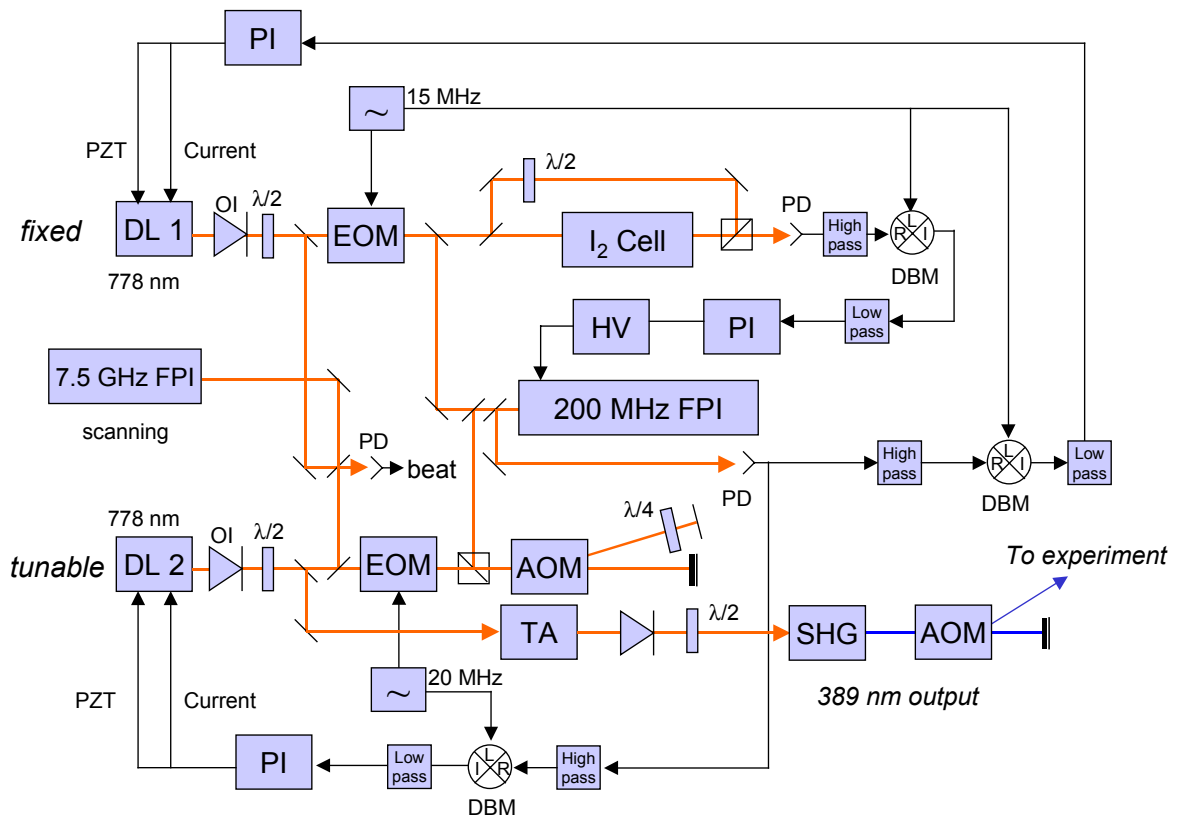


Figure 7.4: The 389 nm laser system. DL1 and DL2: diode lasers; TA: tapered amplifier; DBM: doubly-balanced mixer; OI: optical isolator; PI: feedback circuit; PD: photodiode detector; AOM: acousto-optical modulator; EOM: electro-optical modulator; SHG: second harmonic generation; $\lambda/2$ and $\lambda/4$: half and quarter wave plates.

using RF mixers and served as the error signal to feedback both the PZT voltage and the current of DL1 and DL2 using the PI circuit. The working principle of EOM and the frequency modulation technique are described in more detail in Appendix D. The bandwidth of this servo loop was limited by the PI circuit and was about 50 kHz.

Partial beams of DL1 and DL2 were overlapped into another fast photodiode detector (bandwidth ~ 25 GHz). The beat frequency was read by a microwave counter, which was calibrated by a temperature-controlled crystal oscillator with a frequency

uncertainty of less than 10 ppb. The beat frequency between the two lasers is of extreme importance in this experiment because it directly affects the isotope shift measurement. When both DL1 and DL2 were locked to the FPI, the short-term fluctuation of the center frequency of the beat was less than $10 \text{ kHz}\cdot\text{s}^{1/2}$.

The long-term stability was achieved by locking the length of the FPI to an absorption line of the iodine molecule. The iodine spectrum is very useful because of the numerous rotational and vibrational energy levels, and it conveniently serves as the frequency reference in the visible and near IR range. Figure 7.5 shows the frequency scan over groups of resonances near 777.946 nm . The linewidth of the individual peak is about

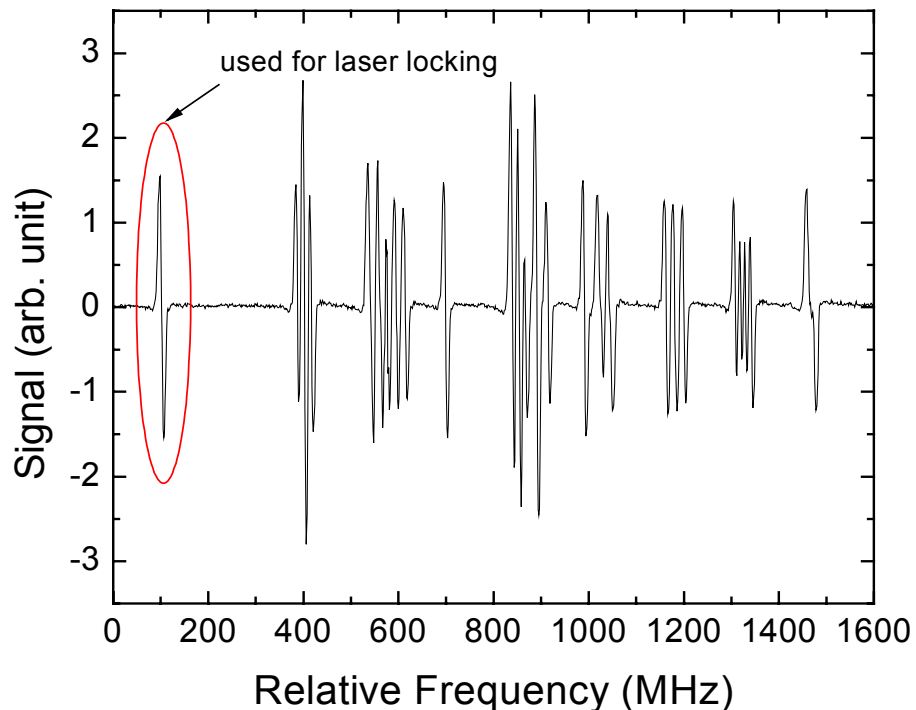


Figure 7.5: Iodine spectrum near 777.946 nm . The width of the absorption feature is 7 MHz .

7 MHz, and a signal-to-noise ratio of about 400 was achieved in 100-ms integration time. The single peak was used for the frequency reference, and the frequency separation between this reference (after frequency doubling) and the transition frequencies of the helium isotopes of interest are shown in Figure 7.6.

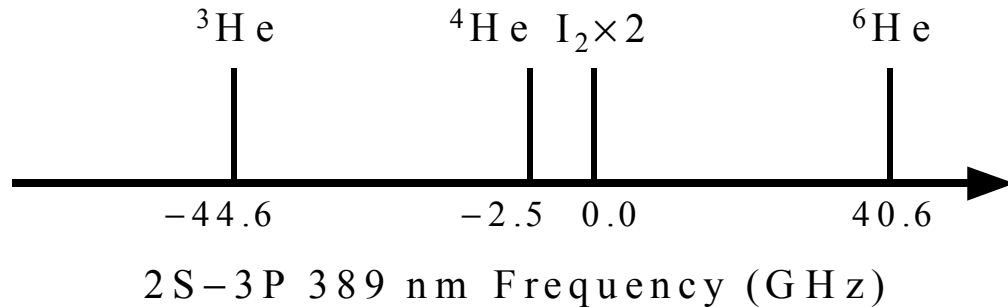


Figure 7.6: Relative frequency position of the iodine line and the helium isotopes.

By tuning the AOM frequency, DL2 became tunable. This frequency scanning process, however, was too slow because it involved feedback to the PZT of DL2 and the doubling ring cavity. For the spectroscopy, the frequency was scanned at 85 kHz. This was achieved by adding another AOM after the doubling ring cavity. Light from the first-order diffraction from the AOM was used for the spectroscopy. The frequency scan was achieved by applying a ramp voltage to the voltage-controlled oscillator (VCO) to produce the required RF wave to drive the AOM used for the blue light. After the VCO was calibrated, the voltage of the ramp could then be converted to frequency. Additional systematic effects that resulted from this frequency scanning method were the change in diffraction efficiency of the AOM for blue light due to different RF frequency and slight beam steering. The former caused uneven background and was minimized by having the center of the resonance peak at the same position of the scan for different isotopes. This

was achieved by several iterations of tuning the AOM used for the IR light so that the resonance peak was close to the middle of the scan. The steering of the laser beam was reduced by focusing the laser beam on the AOM crystal and expanding the beam size to about 3 mm in diameter so that the laser would never miss the atom confined in the trap. The systematic effects from both the trap effect and the probing process will be discussed in the next chapter.

7.3 Chopping and Switching the Laser Light

The infrared trapping light and the blue probing light were both chopped at 100 kHz by RF switches using the same synchronized TTL pulse. The purpose of the fast chopping is described in section 6.4 and the timing sequence of chopping and detection is illustrated in Figure 6.4. The trapping light and probing light were both monitored by fast photodiode detectors to ensure the proper timing. The condition was set so that photons were collected when the trapping light was essentially off. It has been demonstrated that the trapping light could be shut off to an extinction ratio of better than 10^{-3} . Therefore, the possible effect on the isotope shift due to the leakage of the trapping light was less than 1 kHz.

Table 7.1 summarizes the chopping and switching of both the 389 nm and 1083 nm laser in detection and spectroscopy modes. Most of the time, the system was in the detection mode. When an atom was identified by the photon integration circuit, the system was switched to the spectroscopy mode in which the atomic beam shutter was closed, the frequency scan was performed, and data were acquired for one second. Then the system was switched back to the detection mode again.

Table 5.1: Summary of the 1083 nm and 389 nm laser systems in both detection and spectroscopy modes.

	Detection mode	Spectroscopy mode
1083 nm (hot trap)	NOT chopped $I = 70 I_s(2S-2P)$, $\Delta_L/2\pi = -20$ MHz	OFF
1083 nm (cold trap)	Chopped at 100 kHz $I = 5 I_s(2S-2P)$, $\Delta_L/2\pi = -3$ MHz	Chopped at 100 kHz $I = 5 I_s(2S-2P)$, $\Delta_L/2\pi = -3$ MHz
1083 nm (slowing)	$I = 100 I_s(2S-2P)$, $\Delta_L/2\pi = -440$ MHz	OFF
389 nm	NOT chopped $I \sim 1 I_s(2S-3P)$, $\Delta_L/2\pi \sim 5$ MHz, on resonant for hot-trap with light shift	Chopped at 100 kHz $I \sim 1 I_s(2S-3P)$, frequency scanning

7.4 Frequency Scan and Data Acquisition

The scan of the blue laser frequency was made by a singly-passed AOM with fast scanning of the RF frequency. The AOM was driven by a VCO and an RF amplifier. Because of the good linearity between the control voltage and the output RF frequency of the VCO, the scan of the frequency was performed by changing the control voltage using a ramp from a function generator (SRS DS345). It was scanned linearly from 5 to 9 volts, which corresponded to 87 to 105 MHz in RF frequency. Due to a small non-linearity in the voltage-frequency conversion of the VCO, it was calibrated with the frequency counter by changing the DC voltage of the VCO stepwise, and was fitted using a cubic polynomial to get the conversion. The fluctuation of the VCO temperature may slightly change the output RF frequency. Therefore, it was calibrated right before and after the

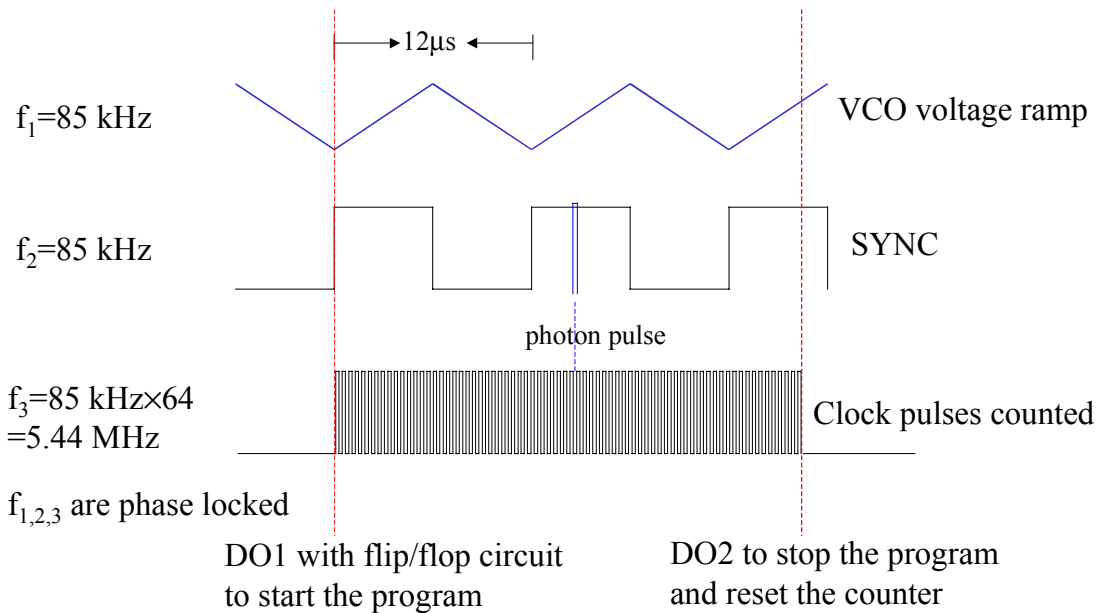


Figure 7.7: Timing of the VCO scanning and photo counting. DO1 and DO2 are the digital outputs from the computer to start and stop the data acquisition.

experiment. Since the resonance line center was always kept at approximately 7 volts of the VCO voltage, the uncertainty from the VCO calibration was very small ($< 1 \text{ kHz}$).

The photon counting and the frequency-scanning ramp must be synchronized to obtain resonant information. The photon detected by the PMT was converted to a TTL pulse by the internal discriminator. The TTL photon pulses were sent to a coincidence pulse generator that was blanked by the trapping light chopping gate. Then the output of the pulse generator was sent to the counter board in the computer for photon counting. Therefore, only when the trapping light was in the off mode could the pulse generator produce the photon pulses. The timing of the scanning ramp and the photon counting is illustrated in Figure 7.7. Three function generators were phase locked by the external trigger function of the generators. One produced the voltage ramp for the VCO, the

second was the synchronized TTL (SYNC) of that ramp, and the third one produced the clock pulses whose frequency was 64 times faster than the ramp. A digital output (DO1) from the computer started the data acquisition at the rising edge of the SYNC. The counter board, National Instrument (NI PCI6602), was used for counting the clock pulses, and the photon pulse triggered the readout of the accumulated counts of the clock pulses. Therefore, each photon pulse detected was associated with the timing information by the number of clock pulses counted. The photons were then sorted according to their arrival time relative to the rising edge of each SYNC. In other words, it was the number of clock pulses counted modulo 64. In order to terminate the data acquisition, another digital output (DO2) stopped and reset the counter. Since each run of the ${}^6\text{He}$ experiment lasted for one to two hours, the accumulated clock pulses often exceeded the maximum counts that the counter could register resulting in overflows. For a 32-bit counter, the maximum number of counts is 2^{32} , whereupon, it resets and starts from one. Since 2^{32} is a multiple of 64 (64 is the number of clock pulses in one SYNC cycle), the sorting method (mod 64) for the photons still works after overflow of the counter. Due to the high linearity of the ramp voltage versus time, the timing information of the photons can then

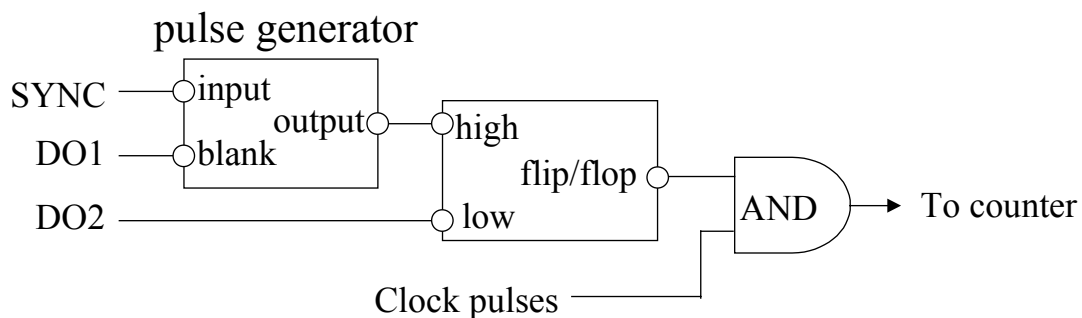


Figure 7.8: Synchronization of the data acquisition. DO1 and DO2: digital outputs to start and stop data acquisition; AND: logic AND gate; SYNC: synchronized TTL of the VCO ramp.

be converted to a VCO voltage, which contains the frequency information of the probing light. It is essential that the scanning of the VCO voltage and the data acquisition are synchronized. This was made possible by the logic circuit using flip-flop as shown in Figure 7.8. Finally, the voltage of the ramp was converted to the VCO frequency using the calibration with a cubic polynomial fit. The frequency was scanned over 18 MHz. Therefore the frequency resolution is $18 \text{ MHz}/32 = 0.56 \text{ MHz/channel}$ (32 channels for scan-up, 32 for scan-down).

A delay time of about $2 \mu\text{s}$ was observed between the change of the ramp voltage and the response of the diffracted blue light's frequency. This was attributed to the traveling time of the RF wave inside the AOM crystal from the PZT (used to produce the acoustic wave) to the focusing spot of the laser light. Other effect might be due to the signal propagation time in the BNC cables. This delay time was constant and stable. Therefore, it cancelled when we compared the difference of the measurements between isotopes. A drift of the phase lock was observed, and the phase sometimes changed by more than five degrees in one day. This happened randomly, was difficult to diagnose, and could cause errors since the measurements relied on the phase information. By averaging the results between frequency scan-up and scan-down, the effect from phase lock cancelled completely. When there was a slip of the timing pulse or a drift between the SYNC and the ramp, the scan-up and scan-down had the opposite effect on the frequency. Therefore, all the measurements used the average of the two, and this possible systematic error was cancelled.

Chapter 8

Systematic Error Study

Systematic effects can limit the precision one can achieve in measuring the isotope shift. These effects include frequency fluctuation of the reference laser, power and pointing direction change of the probe laser, residual magnetic field, and the difference in the motional effect between the isotopes. Some of the effects are normal fluctuations, and have equal influence on different isotopes. In general, this kind of uncertainty can be minimized by frequently switching between measurements of the isotopes. If the effect is associated with some property of the isotopes, *e.g.* the mass or the hyperfine structure, which differs between the isotopes, it may cause a frequency shift that mimics the isotope shift.

The fine structure splittings of the $3^3P_{0,1,2}$ levels of ^4He were measured using the trap method. By a careful balance of the laser power between the two counter-propagating probe beams, no laser power dependence of the resonance line center was observed at the 50 kHz level. The current of the MOT coil was changed by as much as 40%, and no Zeeman shift was observed at the 50 kHz level. However, the measured fine structure intervals disagree with the results in the literature [Yang, 1986] by 300 kHz. This led to a new experiment to measure the fine structure intervals in an atomic beam as an independent systematic check. The discrepancy was then resolved. The isotope shift

between ^4He and ^3He was also measured. The hyperfine structure (HFS) of ^3He complicates the determination of the isotope shift. Using the theoretical value of the HFS, the result agrees with the previous, but less precise, measurement.

8.1 Fine Structure Splitting Measurement of ^4He in the Trap

As mentioned in section 3.3, the measurement of the fine structure intervals of ^4He , $2^3\text{P}_{0,1,2}$ and $3^3\text{P}_{0,1,2}$, provides an important testing ground for the atomic theory and is a powerful method to determine the fine structure constant α . The splittings of the lower levels, $2^3\text{P}_{0,1,2}$, were measured to a precision of 1 kHz by laser excitation in an atomic beam [Castilleja, 2000; Minardi, 1999] and by microwave technique [George, 2001]. On the other hand, the $3^3\text{P}_{0,1,2}$ intervals were only measured to a precision of about 20 kHz by a level crossing technique [Yang, 1986].

To check the systematic effects of the spectroscopic measurement in the trap, we continuously loaded the trap with a small atomic cloud consisting of tens of ^4He atoms. The number density of the atomic cloud was so low that the atom-atom interaction was negligible. The signal to noise was much better than the single atom spectroscopy, and it enabled us to quickly diagnose the systematic effects. The laser power was changed from $1.5 I_s$ to $0.05 I_s$, and it was found that the balance of the laser intensity between the two counter-propagating probe beams was critical. If the two beams are not perfectly aligned, the atom may absorb and scatter more photons from one of the laser beams. This results in a motional effect. This is described in section 6.4 where a slow chopping and scanning system was used. Although we used a fast (100 kHz) chopping system, this effect still must be studied. Otherwise a shift of several hundred kHz was present when the intensity

of the probe laser was high ($\sim 1 I_s$). To align the retro-reflected beam, a CCD camera took the image of a large ^4He trap (millions of atoms). The blue laser was detuned far from resonance by more than 20 MHz so that it only illuminated the atoms, but exerted little force on them. The retro-reflected beam was tuned for the brightest trap spot, and the position of the trap was recorded. The frequency of the blue laser was then tuned to the resonance. Usually the imperfect balance between the two laser beams would push the atomic cloud, and as a result, the position of the trap changed. The strategy was to adjust the retro-reflected beam to move the trap back to the old position where the shape of the trap was reasonably spherical. For fine adjustment of the intensity of the two laser beams, one of the lens pair used to expand and collimate the laser beam was mounted on a translation stage, and provided a gentle focusing of the retro-reflected beam to compensate the transmission loss of the mirror and vacuum windows. The position of the lens was moved step by step until no blue power dependence was observed on the frequency of the resonance line center.

Figure 8.1 shows no observable blue power dependence for three measured fine structure intervals, defined as ν_{12} , ν_{01} , and ν_{02} . The value shown here is the difference between this measurement and the result by Yang *et al.* [Yang, 1986], with the correction in [Yan, 1994]. It showed an obvious disagreement of about 200 ~ 300 kHz for ν_{12} and ν_{10} , but reasonable agreement for ν_{02} . To search for possible systematic effects, the current of the MOT coil was changed to search for changes in the Zeeman shift. Because the probe laser was linearly polarized and the atom automatically sought the zero-field position in the MOT, the Zeeman shift was expected to be very small. Figure 8.2 shows

that no magnetic field effect was observed. To our knowledge, no other effect could cause the shift as much as 300 kHz.

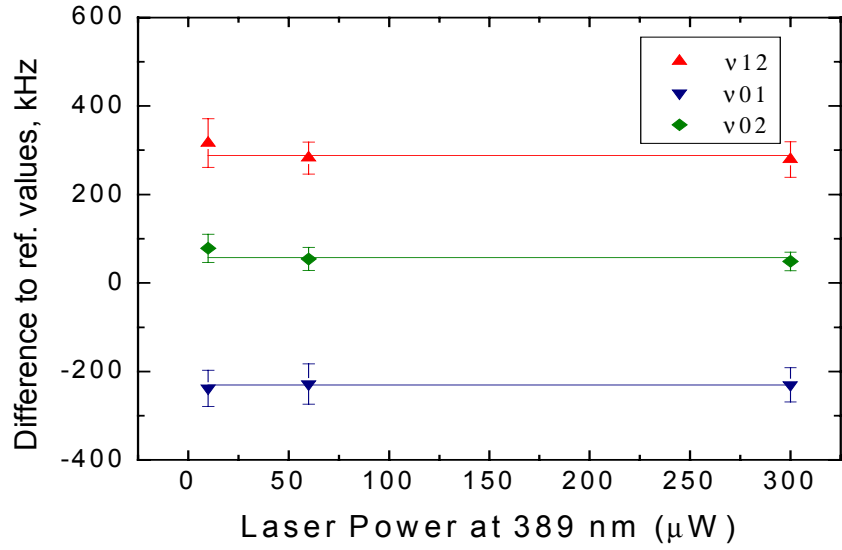


Figure 8.1: Results of the fine structure splittings compared to [Yan, 1994] for different laser power.

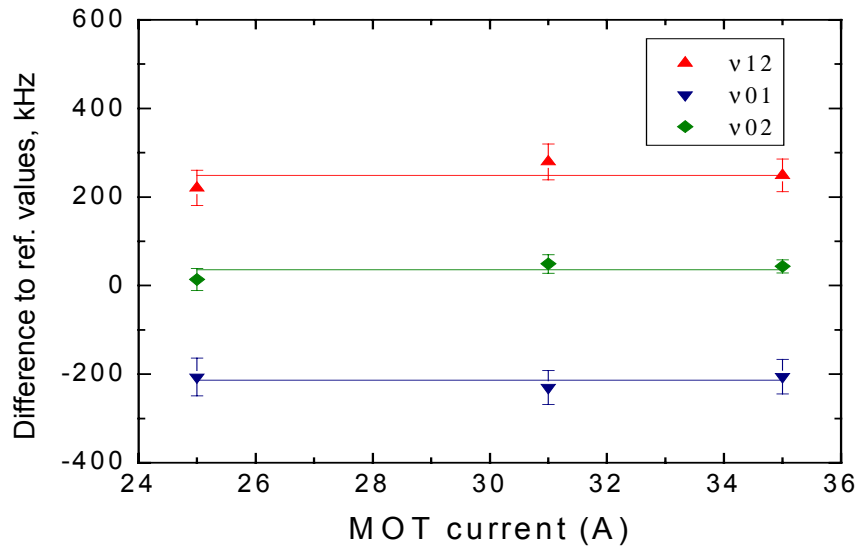


Figure 8.2: Results of the fine structure splittings compared to [Yan, 1994] for different MOT currents.

Because the alignment of the probe laser is critical, it was checked carefully before each ${}^6\text{He}$ run. Figure 8.3 shows the data of the fine structure interval of ν_{12} taken one day before the ${}^6\text{He}$ run in April and May 2004. Each data point is an average of three identical measurements. The error bar on each data point is the standard deviation of the three identical measurements. These deviations may arise from normal statistical uncertainties, the fluctuation of the iodine lock and the stability of the DL2 lock to the FPI. Data were recorded when the trap conditions were changed: laser power was varied from $0.05 I_s$ to $1.5 I_s$ and MOT current, from 25 A to 38 A. No dependence was found at the 50 kHz level. The large reduced chi-square (~ 3) was attributed to the systematic error of the trap effect. This systematic was derived from the standard deviation of a total of 10 data points where the statistical uncertainties were excluded:

$$\sigma_{sys}^2 = \sigma_{total}^2 - (\bar{\sigma}_i / \sqrt{3})^2. \quad (8.1)$$

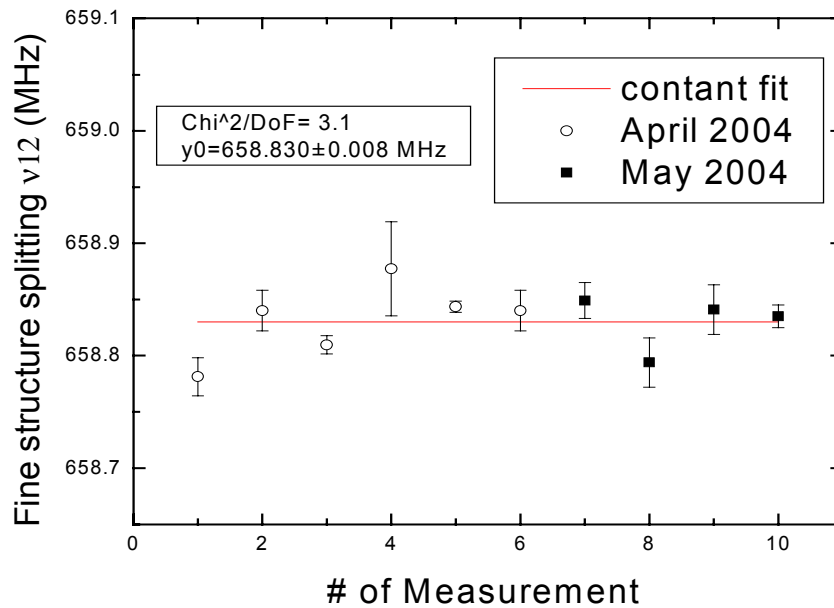


Figure 8.3: Fine structure splitting measurement with a linear fit.

The results are shown in Table 8.1 in comparison with the former measurements. A discrepancy of more than 200 kHz was found, and this discrepancy was mainly due to the position of the 3^3P_1 line. The previous results were all based on the level crossing between the Zeeman sublevels under high magnetic field. The fine structure splittings could then be extracted at the zero-field position. The homogeneity and the precision of the magnetic field were achieved and measured at the ppm level by the NMR probe. To test the accuracy of our trap method, a third measurement with different technique is strongly desired. A setup to measure the fine structure intervals in the atomic beam was constructed to independently check the systematic effect of our system.

Table 6.1: Results of various fine structure interval measurements. The errors in the parentheses in this work are statistical and systematic respectively.

	v12 (MHz)	v01 (MHz)	v02 (MHz)
Wieder and Lamb [Wieder, 1957]	658.550(150)	8113.780(220)	8772.330(370)
Kramer and Pipkin [Kramer, 1978]	658.634(271)	8113.920(290)	8772.552(40)
Yang and Metcalf* [Yang, 1986]	658.561(36)	8113.965(38)	8772.526(13)
This work (trap)	658.830(8)(31)	8113.742(5)(40)	8772.573(7)(56)

*With the correction of the g factor by Yan and Drake [Yan, 1994]

8.2 Fine Structure Splitting Measurement of ^4He in the Atomic Beam

To resolve the discrepancy between the trap method and the level crossing method, we sought a third measurement with comparable accuracy. The Doppler-free saturation spectroscopy in a vapor cell is straightforward, and can provide great signal to noise

using a lock-in technique. By this method, the helium spectroscopy on the 3^3P levels has been performed by Adams *et al.* [Adams, 1992] and Marin *et al.* [Marin, 1995]. The former measured the total $2^3\text{S}-3^3\text{P}$ transition frequency to determine the Lamb shift. The latter determined the $^3\text{He}-^4\text{He}$ isotope shift, and the hyperfine structures of ^3He . However, no 3^3P fine structure splittings of ^4He have ever been reported by this method. We then set up a saturation spectroscopy experiment with the conventional linear-linear pump and probe scheme. Two problems were the pressure shift and the Zeeman shift. The pressure shift could be measured by changing the helium pressure in the cell, and extracting the result linearly to the zero-pressure point. In [Adams, 1992] and [Marin, 1995], the extrapolation gave an uncertainty of the zero-pressure frequency to be 100 ~ 200 kHz. In reality, due to the temperature fluctuation and the non-repeatability of the discharge condition, a precision at the 10 kHz level would be very challenging and difficult. As to the Zeeman shift, the blue laser was linearly polarized to be better than 99%. However, due to optical pumping, the difference between the $\Delta m = 1$, and $\Delta m = -1$ transitions could be larger than 20%. Therefore, magnetic field shielding was required.

Due to these difficulties, we chose to perform the spectroscopy in a collimated atomic beam, which is immune to most of the systematic uncertainties. The setup is shown in Figure 8.4. The metastable atomic beam produced by the LN_2 -cooled RF discharge source was collimated by applying two-dimensional transverse cooling light at 1083 nm. After a flight path of 180 cm, the atomic beam intersected perpendicularly with a pair of anti-parallel laser beams to excite the $2^3\text{S}_1-3^3\text{P}_{0,1,2}$ transitions. The induced fluorescence passed a blue filter and was focused onto a PMT by a detection scheme similar to that used for trap detection. The overall photon detection efficiency was about

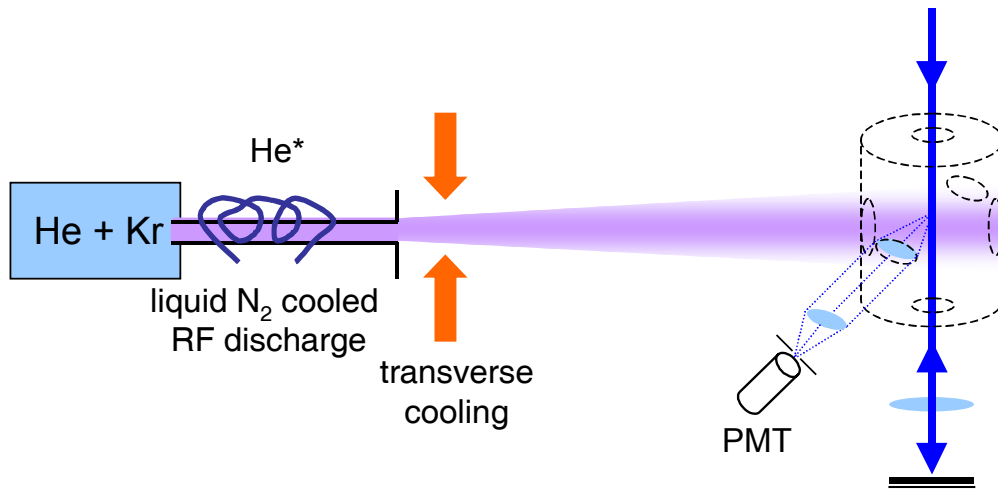


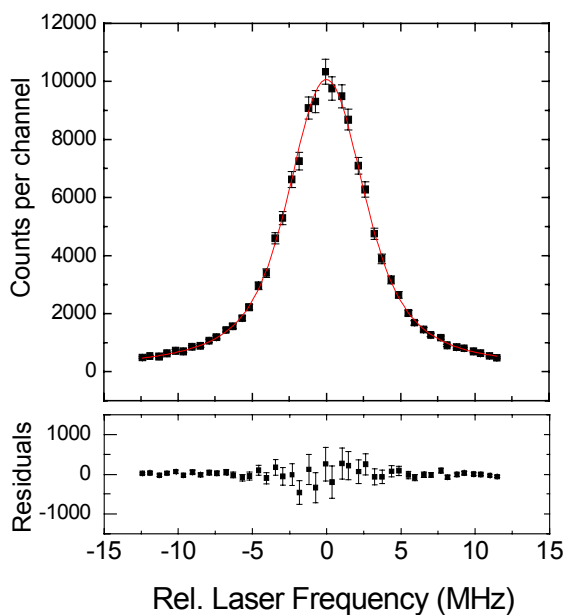
Figure 8.4: Production of the metastable helium beam and the detection scheme.

0.1%. The interaction region was enclosed by a magnetic shield with an attenuation factor of 800 to minimize the Zeeman shift from the Earth's field.

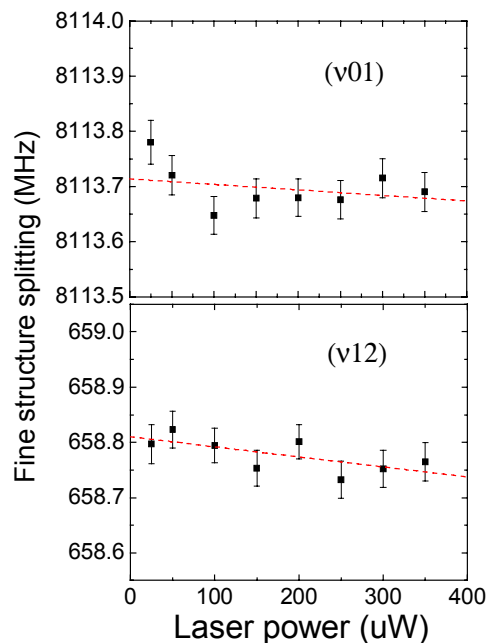
The laser system was identical to the one used for the trap spectroscopy. To ensure the minimum beam steering, the frequency scan was performed by changing the RF frequency of the IR AOM used for the DL2 lock to the FPI instead of the blue AOM. Therefore, the direction of the blue laser was determined by the doubling ring cavity, and did not change when we switched between the three transition lines. The blue laser beam was spatially filtered by focusing it through a 50- μm pinhole, and subsequently expanded to a diameter of about one cm. The transmission of the blue laser through the pinhole also monitored the beam direction, and the stability was better than 2.5×10^{-3} mrad. A “cat's eye” retro-reflector was used to ensure the retro-reflected beam overlap perfectly with the incoming beam. This largely cancelled possible Doppler shifts due to the beam steering when switching between different transitions. To make sure the laser beam was perpendicular to the atomic beam, we compared the resonance center position obtained

using two laser beams to the one obtained when the retro-reflected beam was blocked. Several iterations of tuning the beam direction were performed until the two results matched. This procedure is critical for the isotope shift measurement because different isotopes have different velocities. However, in the case of the fine structure measurement, if the laser beam and the atomic beam are not perfectly perpendicular, it only broadens the line, and the effect on the determination of the splittings is negligible.

The blue laser frequency was scanned over a range of about ± 15 MHz around the center. The photon counts from the PMT and the beat frequency between DL1 and DL2 were recorded as data. Figure 8.5(a) shows a typical scan and the residual of the resonance curve. The fit of the data using a Voigt profile produced the Gaussian and the Lorentzian width of about equally 3 ~ 4 MHz. The errors of the photon counts were not purely statistical, but also included a 3 ~ 5% contribution from the power fluctuation, which was added to the error of each data point so that the reduced chi-square of the Voigt fit was approximately unity. The largest systematic effect was the momentum transfer from the laser light to the atoms. During the travel time of the atom through the interaction region (~ 10 μ s), the atom could scatter more than one photon, and change its velocity. Therefore, the experiment must be performed in a very low laser intensity regime to ensure that only one photon is scattered per atom. To investigate this effect, the laser power was changed from 25 to 350 μ W (0.9% to 13% of the saturation intensity), and the fine structure splitting was measured as a function of laser power. There was indeed a small but noticeable power dependence as shown in Figure 8.5(b). The experimental values for the fine structure intervals were obtained by extrapolating linearly to zero laser power.



(a)



(b)

Figure 8.5: Line center determination of the helium transition. (a) The resonance with fit of the line shape. (b) The power dependence of the line center was observed. The fine structure splittings were obtained by extrapolating linearly to zero laser power.

Some possible systematic uncertainties were also investigated. The residual magnetic field within the interaction region was measured to be less than 3 mGauss. To estimate the effect from the Zeeman shift, the magnetic shield was removed, and a magnetic field up to 8 Gauss was applied. An asymmetry of the Zeeman levels of up to 20% was observed. From this information and the Zeeman shift of 1.4 MHz/Gauss, it could be inferred that the residual Zeeman shift on the line center at 3 mGauss was less than 0.8 kHz. The light shift and pressure shift were also both well below the 1 kHz level. The only important systematic effect was from the steering of the laser beam. The maximum uncertainty of 2.5×10^{-3} mrad, and 10% asymmetry between the two anti-parallel laser beams produced 5 kHz Doppler shift for the helium beam cooled to a LN₂

temperature. The final results are shown in Table 8.2. In the mean time, a theoretical calculation was performed by our collaborator, G.W.F. Drake. The experimental result and theory show excellent agreement (Figure 8.6). This not only resolves the discrepancy between our measurement and the former results, but also adds confidence to the trap method and the atomic theory calculations.

Table 8.2: Results of the fine structure intervals by this work.

	v12 (MHz)	v01 (MHz)	v02 (MHz)
This work (trap)	658.830(32)	8113.742(40)	8772.573(56)
This work (atomic beam) [Mueller, 2004]	658.810(18)	8113.714(28)	8772.524(33)
Theory, G.W.F. Drake [Mueller, 2004]	658.801(6)	8113.730(6)	8772.531(6)

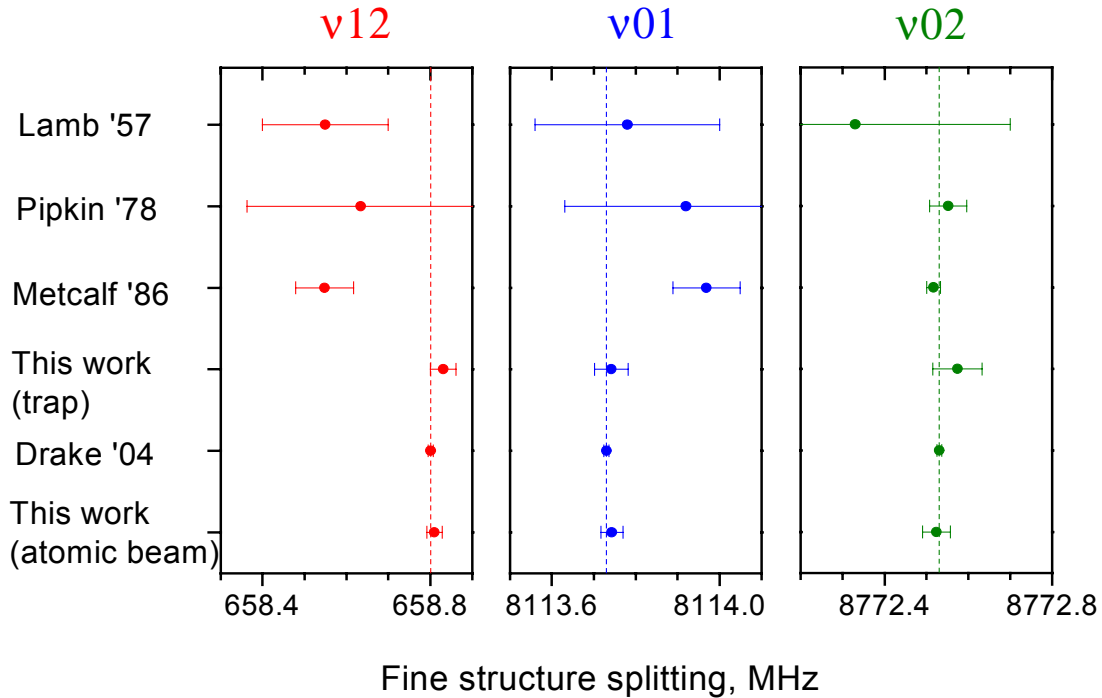


Figure 8.6: Results of the fine structure intervals compared to the theory and former measurements. The dotted lines indicate the theoretical values.

8.3 Isotope Shift Measurement of ^3He

^3He is a stable isotope and its isotopic abundance in the atmosphere has been measured to be 1.4 ppm [Mamyrin, 1970]. The measurement of the isotope shift between ^3He and ^4He provides the best test of the systematic effects. However, the hyperfine structure of ^3He complicates the determination of the isotope shift because the effects from the nuclear moment interactions must be subtracted. Furthermore, the previous isotope shift measurement for the $2\text{S}-3\text{P}$ transition of ^3He only achieved a precision of about 150 KHz [Marin, 1995], and lacks the required precision to test our systematic effects.

Our helium sample was from the commercial gas bottle, and was actually extracted from natural gas. The ^3He isotopic abundance was calibrated to be 0.28 ppm [Wang, 2003]. For the largest ^4He trap that we have achieved, the number of atoms in the trap was as large as 50 million. Therefore, if we assume a similar trapping efficiency for ^3He and ^4He , and take the ^3He abundance of 0.28 ppm from the calibration, there will be tens of ^3He atoms in the trap. Therefore, a purified ^3He sample is not necessary. (Due to the hyperfine structure and the larger velocity of ^3He , the trapping efficiency is actually smaller than that of ^4He .) Figure 8.7 shows the energy level diagram of ^3He and ^4He . The ^3He levels, $2^3\text{S}_{1, F=3/2}-3^3\text{P}_{2, F=5/2}$ were used for the cycling transition. The hyperfine shifts must be subtracted for both the upper and lower levels. The lower state splitting was measured by Rosner and Pipkin [Rosner, 1970] to a very high precision. Using this information, all the hyperfine splittings of the upper states were calculated by G.W.F. Drake, and presented in [Marin, 1995] to a precision of about 100 kHz. Therefore, the isotope shift in the absence of a hyperfine shift, Δ_1 , can be derived by Δ_2 , the quantity we have measured including hyperfine shift, using $\Delta_1 = \Delta_2 + (2246.587 - 2162.767)$ MHz,

where 2246.587 MHz is the hyperfine shift of the lower level, and 2162.767 MHz is that of the upper level. The experiment was similar to the ^4He fine structure measurement in the trap. Trap conditions including the laser power and MOT current were varied, and the fluctuations due to these variations are taken as the systematic uncertainties. The photon recoil effect must be taken into account to obtain the isotope shift. This effect comes from

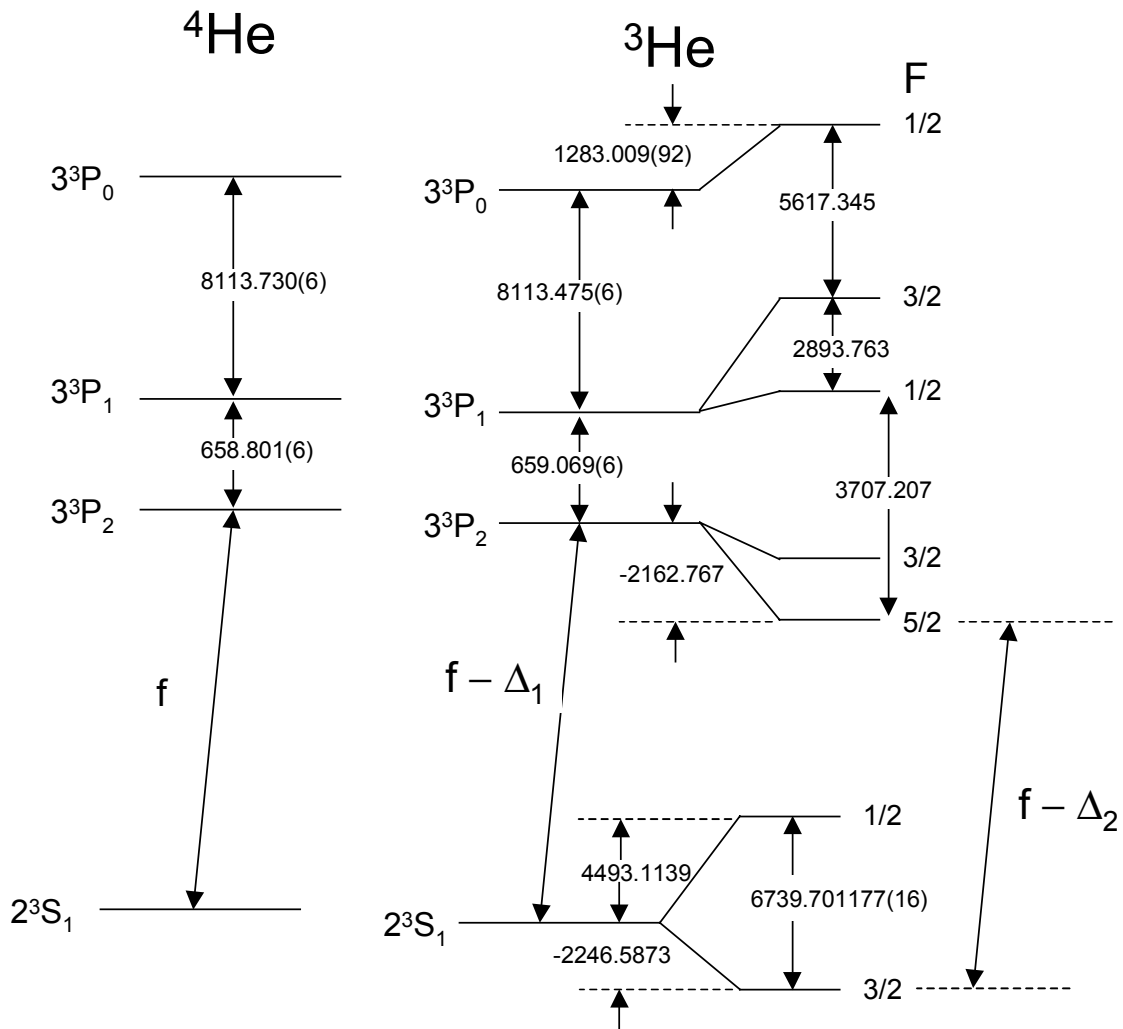


Figure 8.7: Energy level diagram of ^4He and ^3He . The numbers are theoretical calculation from G.W.F. Drake except the HFS of the ^3He ground states.

the fact that the energy of the photon impinging on the atom actually includes both the level splitting and the kinetic energy of the atom to conserve momentum:

$$E_\gamma = E_{\text{int}} + P_\gamma^2/2M_{\text{atom}}, \quad (8.2)$$

where E_γ is the energy of the photon, E_{int} is the real splitting, and P_γ is the momentum of the photon. Therefore, the recoil correction almost cancels and is negligible for the ^4He fine structure measurement. But due to the mass dependence of the recoil effect, it causes a significant 108 kHz correction for the isotope shift measurement of ^3He - ^4He . Based on 28 measurements, the isotope shift between $2^3\text{S}_{1, F=3/2}$ - $3^3\text{P}_{2, F=5/2}$ of ^3He and 2^3S_1 - 3^3P_2 of ^4He was determined to be $\Delta_2 = 42100.448(9)(39)$ MHz. The errors are statistical and systematic uncertainties, respectively. Therefore, $\Delta_1 = 42184.268(40)$ MHz plus the uncertainty from the hyperfine shift of the upper level (~ 100 kHz), $\Delta_1 = 42184.268$ (~ 100) MHz.

We can then check our isotope shift measurement by using the mass shift and charge radius of ^3He , which has been measured very precisely in [Shiner, 1995] to be 1.9506(14) fm, and by using the formula for the 2^3S_1 - 3^3P_0 isotope shift in [Marin, 1995]:

$$\text{IS}(2^3\text{S}_1-3^3\text{P}_0) = 42184.284 \text{ MHz} + 3.93(\langle r_c^2 \rangle_{\text{He3}}^{1/2} - 1.95) \text{ MHz/fm}. \quad (8.3)$$

Therefore, we obtain

$$\Delta_1 = \text{IS}(2^3\text{S}_1-3^3\text{P}_2) = 42184.286(5) + 0.013 = 42184.299(5) \text{ MHz},$$

where the isotope shift for the 2^3S_1 - 3^3P_2 transition must include the 13 kHz difference of the fine structure interval ν_{02} (3^3P_0 - 3^3P_2) between the two isotopes. The result agrees with the former measurements at the 100 kHz level. However, this work and the work by Marin *et al.* both rely on the theoretical calculation to extract the hyperfine shift. Thus a better determination of the hyperfine splittings is strongly desired.

Table 8.3: Comparison of the ^3He - ^4He isotope shift in the absence of HFS.

IS in the absence of HFS	This work	Shiner + Drake	Marin
Δ_1 in MHz	42184.268(100)*	42184.299(5)	42184.321(165)

*The uncertainty is dominated by the hyperfine shift correction.

8.4 Systematic Uncertainty Summary

In conclusion, the ^4He fine structure measurement agrees well with the theoretical calculation. The ^3He - ^4He isotope shift is consistent with the former but less precise measurement, and also with the theoretical prediction using the well-known ^3He charge radius. This adds to our confidence in the accuracy of the ^6He measurement. The systematic uncertainty from the trap effect is quoted to be 40 kHz, which is the standard deviation of thirty ^4He fine structure measurements under different trap conditions. These include the heating and cooling effect by changing the laser power, and the residual Zeeman shift by changing the field gradient of the MOT by a factor of two. Other effects include uneven background due to the change of the AOM diffraction efficiency associated with the frequency scan, the stability of the frequency counter, and the calibration of the voltage-frequency conversion of the VCO, and are listed in Table 8.4.

Table 8.4: Summary of the systematic uncertainties.

Source of systematic effect	Error (kHz)	Comments
Trap effect	40	By changing trap conditions.
Uneven background	20	Fit line center with and without background subtraction.
Counter calibration	9	Counter stability < 0.2 ppm.
AOM calibration	0.3	Negligible, mainly due to temperature fluctuations.
Total	45.6	

Chapter 9

Results and Discussion

In this chapter, the detection and spectroscopy of the individual trapped ${}^6\text{He}$ atoms are discussed. The method is identical to the ${}^3\text{He}$ - ${}^4\text{He}$ isotope shift measurement except that the loading rate of ${}^6\text{He}$ is much lower. In practice, in order to accumulate enough photon statistics, about 150 ${}^6\text{He}$ atoms were required to make a 100 kHz determination of the resonance line center, and typically this took several hours with a trapping efficiency of 2×10^{-8} and the ${}^6\text{He}$ production rate of $3\times 10^6/\text{s}$. Therefore, the long-term frequency stability of the iodine lock is critical. If there is a slow frequency drift in the reference laser, it will mimic the isotope shift when we switch between the isotopes. The switching between the measurements of ${}^4\text{He}$ and ${}^6\text{He}$ must be made as frequently as possible so that the effect could be minimized.

Two experimental runs were performed in April and May 2004. Nineteen data points of the isotope shift between ${}^4\text{He}$ and ${}^6\text{He}$ were accumulated, and each data point had a statistical uncertainty between 100 to 200 kHz. The measured isotope shift, 43194.772(33)(46) MHz gave the field shift of $-1.430(58)$ MHz by subtracting the theoretical calculation of the mass shift. Based on this result and the well-known charge radius of ${}^4\text{He}$, the root-mean-square charge radius of ${}^6\text{He}$ was determined to be 2.054(14) fm. This result can be compared with values predicted by various theories and models of

nuclear structure. Furthermore, other effects, which were not considered carefully by theoretical treatments in the past, may be important at this level of precision, *e.g.* the nuclear polarizability, the interpretation of the proton size, and the pion-exchange current. These will be discussed in this chapter.

9.1 Single ${}^6\text{He}$ Atom Detection

The ${}^6\text{He}$ atom has an identical atomic structure as that of ${}^4\text{He}$, and the detection of ${}^6\text{He}$ is straightforward. The average trap lifetime of ${}^6\text{He}$ was about 0.4 sec, which was a combination of the collisional loss and the nuclear decay. This lifetime was considerably shorter than the trap lifetime of ${}^4\text{He}$ (approximately 0.6 sec). When the ${}^7\text{Li}$ nuclear beam was on the target, significant increase of the background counts of the PMT was observed from 150 cps to 250 cps. The source of the nuclear-beam-induced background is not clear, but it could be due to the bremsstrahlung effect of the fast moving electrons from

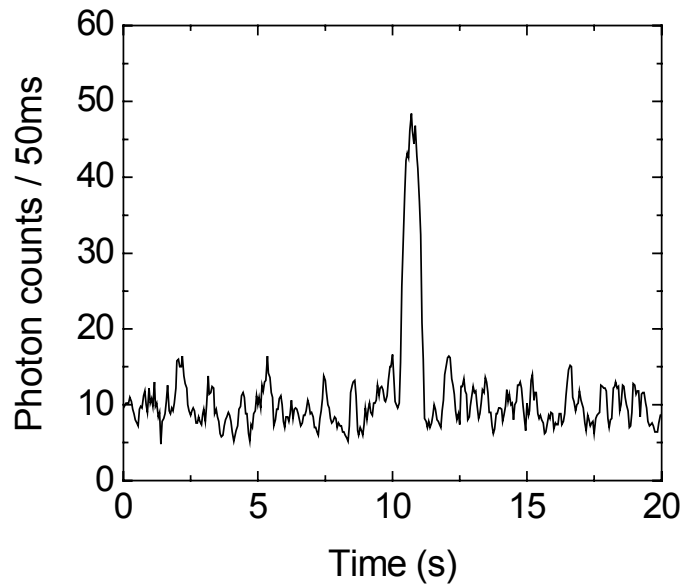


Figure 9.1: Fluorescence signal of a single trapped ${}^6\text{He}$ atom.

the decay of neutrons or other radioactive nuclei produced. The shielding with lead, stainless steel and polyethylene plates around the PMT helped decrease the nuclear-beam-induced background. Some unusual spikes associated with the nuclear beam were also observed. However, the duration of these spikes were very short (< 10 ms), and they could be excluded by applying a cut on the lifetime in the trap.

Figure 9.1 shows a single atom signal with the blue laser frequency fixed and tuned approximately to the resonance of ${}^6\text{He}$. The blue light and the trapping light were kept in the detection mode. A single ${}^6\text{He}$ atom could be clearly identified with S/N of approximately 10 in a 50 ms integration time. To further confirm the detection of ${}^6\text{He}$, the detuning of the trapping light was varied while the loading rate was recorded as a function of the trap detuning frequency as shown in Figure 9.2. The observed behavior confirms the production and identification of the ${}^6\text{He}$ atoms.

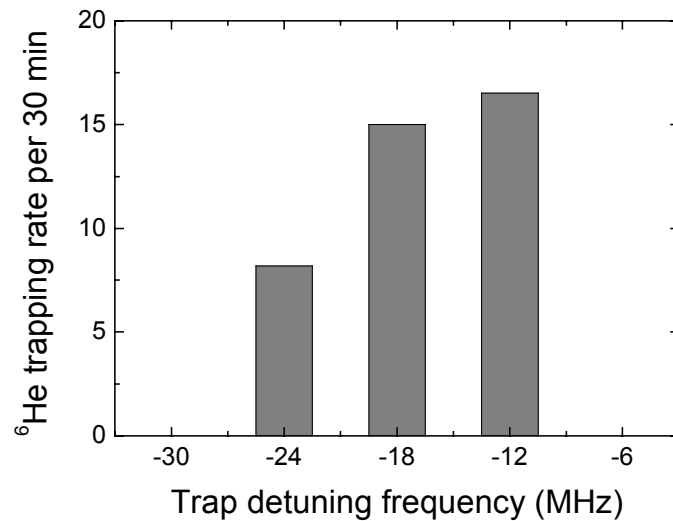


Figure 9.2: Trap loading rate vs. MOT laser detuning frequency. Note: in this test the MOT light and the transverse cooling light had the same frequency. The maximum loading rate occurred at a MOT detuning frequency of about -10 MHz. While in later experiments, the laser frequency for trapping and transverse cooling were controlled independently, and the maximum loading rate occurred at a MOT detuning frequency of about -20 MHz.

9.2 Analysis of the Resonance Line Shape

The ${}^6\text{He}$ atom exhibits more inertia to the heating and cooling effect from the probe laser than that for ${}^4\text{He}$. The Doppler width of ${}^6\text{He}$ atoms is smaller compared to that of ${}^4\text{He}$ at the same temperature. Therefore, if there is an asymmetry in the line shape, it causes a possible systematic error in the determination of the line center. The typical spectrum of ${}^4\text{He}$ and ${}^6\text{He}$ were fit using a Gaussian profile as shown in Figure 9.3. The residual of the fit was symmetric about the center frequency, and the reduced chi-square of the fit was close to unity. The fit using a Voigt profile gave very similar result at the center frequency. The individual fit differed by less than 10 kHz compared with the Gaussian fit, and no bias in the isotope shift from the choice of the fitting function was observed.

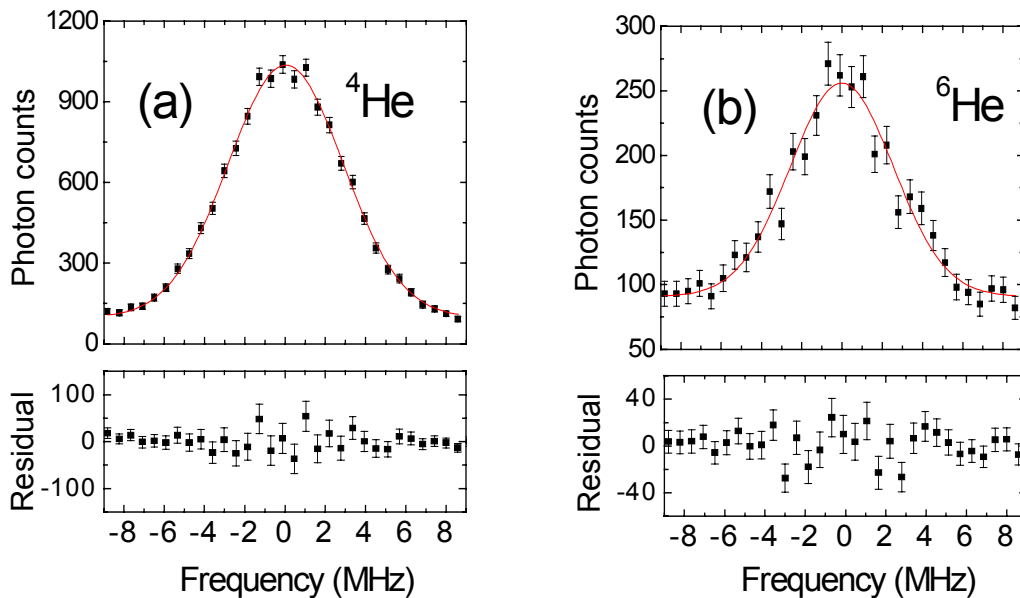


Figure 9.3: (a) The ${}^4\text{He}$ spectrum accumulated with approximately 1000 atoms in 5 minutes. The curves represent Gaussian fits. The fit gives a statistical error of 0.029 MHz at the center frequency, and a FWHM of 6.8 MHz. (b) The ${}^6\text{He}$ spectrum accumulated with approximately 150 atoms in one hour. The Gaussian fit gives a statistical error of 0.111 MHz in the center frequency, and a FWHM of 6.2 MHz.

9.3 Determination of ^4He – ^6He Isotope Shift

The combined results from the April and May runs in 2004 are shown in Figure 9.4. The two results are in excellent agreement with one another. The final result of the isotope shift is based on the weighted average of the 19 data points. Each data point is the average of the scan-up and scan-down results. The scatter of the 19 data points is not purely statistical. As we expected, the fluctuation of the iodine lock also contributed to the scatter of the data points. The error bars shown in Figure 9.4 include the estimated uncertainties from the iodine lock. As a measure of the iodine lock uncertainty, we added 70 to 100 kHz for the April run, and 20 kHz for the May run so that the reduced chi-square of the constant fit was close to unity. This agrees with our expectation of the iodine lock stability. From April to May, the iodine spectrometer was upgraded, and the S/N was improved by approximately a factor of five. This was achieved by increasing the laser intensity of the pump beam in the iodine spectroscopy using an additional laser injection-locked to DL1 (see section D.2 and Figure D.1).

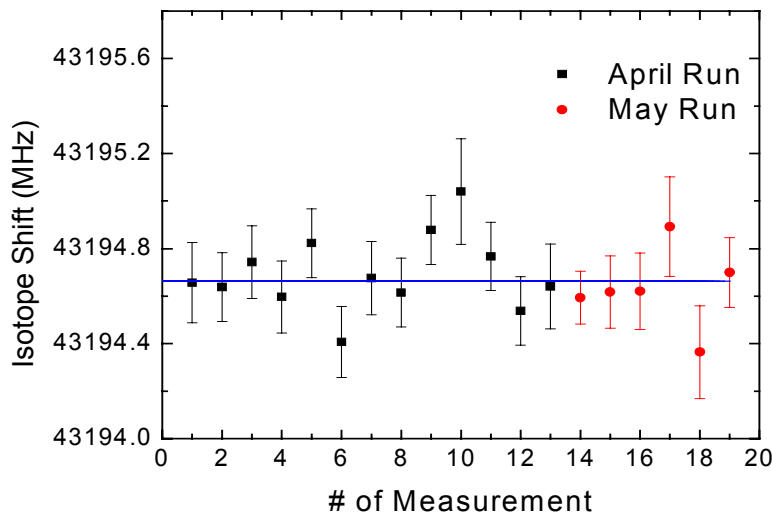


Figure 9.4: Determination of the isotope shift. The uncertainty of the constant fit of the 19 data points is 0.033 MHz, and the reduced chi-square is 0.9.

The final result of the isotope shift including the uncertainties is listed in Table 9.1. The recoil correction is described in Eq. 8.2. From this results and Eq. 3.16(b), we conclude the field shift is $-1.430(58)$ MHz, and the difference between the mean-square charge radii $\langle r_c^2 \rangle_{\text{He6}} - \langle r_c^2 \rangle_{\text{He4}} = 1.418(58) \text{ fm}^2$. With the previously determined charge radius of ${}^4\text{He}$ $1.673(1)$ fm by muonic atom spectroscopy [Borie, 1978], the root-mean-square charge radius of ${}^6\text{He}$ from this measurement is then $2.054(14)$ fm [Wang, 2004]. The uncertainties of the measured ${}^6\text{He}$ charge radius from various sources are summarized in Table 9.2. This result does not assume any proton and neutron distributions inside the nucleus, and is model-independent. Using the consistent but less accurate ${}^4\text{He}$ radius $1.676(8)$ fm from electron scattering [Sick, 1982] to avoid the controversy of the muonic atom result, the charge radius of ${}^6\text{He}$ becomes $2.056(16)$ fm, or increases slightly by 0.1%.

Table 9.1: Summary of the isotope shift with uncertainties.

Item	Magnitude (MHz)	Error (MHz)
Measured frequency difference	43194.662	Listed below
Statistical uncertainty		0.033
Systematic uncertainty		0.046
Recoil correction	0.110	< 0.001
Final isotope shift	43194.772	0.056
Field shift	-1.430	0.058

Table 9.2: Summary of the uncertainties of the measured ${}^6\text{He}$ charge radius.

Source	Uncertainty (fm)	Percentage (%)
Spectroscopy	0.0135	0.66
Statistical	0.008	0.39
Systematic	0.011	0.54
Mass shift	0.004	0.19
${}^4\text{He}$ charge radius	0.0008	0.04
Total	0.014	0.68

9.4 Point-Proton Radius of ${}^6\text{He}$ and Comparison with Theories

In the nuclear theories using meson-exchange models, the distributions of protons and neutrons are calculated while treating both as point-like particles. By definition, the point-proton mean-square radius is the mean expectation value of the square of the position vector of the individual protons:

$$\langle r_{pt}^2 \rangle = \frac{1}{Z} \sum_{i=1}^Z \langle 0 | r_i^2 | 0 \rangle, \quad (9.1)$$

where r_i is the position of the i th proton measured from the center of mass, and $|0\rangle$ is the ground-state wave function of the nucleus. However, the charge radius we measured from the isotope shift includes the contribution from the charge density of the individual protons and neutrons, and is defined as

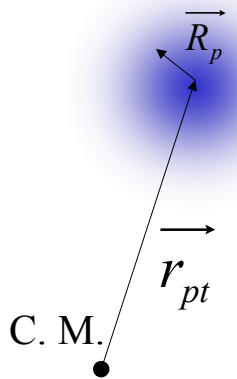
$$\langle r_c^2 \rangle = \int \langle 0 | r^2 | 0 \rangle d^3 \vec{r} = \frac{1}{Ze} \int r^2 \rho(\vec{r}) d^3 \vec{r}, \quad (9.2)$$

where $\rho(\vec{r})$ is the charge density including all sources. Assuming no nuclear-medium modification effects, the point-proton radius is related to the charge radius by the following relation (see Figure 9.5):

$$\langle r_c^2 \rangle = \langle r_{pt}^2 \rangle + \langle R_p^2 \rangle + N/Z \langle R_n^2 \rangle + \frac{3}{4M_p^2}, \quad (9.3)$$

where $\langle R_p^2 \rangle^{1/2}$ is the rms charge radius of proton, 0.895(18) fm derived from electron scattering [Sick, 2003]. The quantity $\langle R_n^2 \rangle$ is the mean-square charge radius of neutron, $-0.120(5)$ fm² measured by the transmission of low energy neutrons through heavy elements Bi and Pb [Kopecky, 1995 and 1997]. The additional term, $\frac{3}{4M_p^2}$, is the

Darwin-Foldy correction of the proton radius (see section 9.5). We can then derive the



The total charge is normalized to one.

$$\begin{aligned}
 \langle r_c^2 \rangle &= \int r^2 \rho(\vec{r}) d^3 \vec{r} = \int (\vec{r}_{pt} + \vec{R}_p)^2 \rho(\vec{R}_p) d^3 \vec{R}_p \\
 &= \int r_{pt}^2 \rho(\vec{R}_p) d^3 \vec{R}_p + \int R_p^2 \rho(\vec{R}_p) d^3 \vec{R}_p + \text{cross term} (= 0) \\
 &= \langle r_{pt}^2 \rangle + \langle R_p^2 \rangle
 \end{aligned}$$

Figure 9.5: Contribution to the total charge radius due to the proton charge distribution. The cross term vanishes by symmetry. This derivation can also be applied to neutrons with additional normalization factor N/Z . Note: Eq. 9.3 does not assume any distribution of the point neutrons, which is clear in this derivation because of the zero net charge of neutrons.

point-proton radius of ${}^6\text{He}$ from this measurement to be 1.904(18) fm. In order to compare the theoretical results with this measurement, the calculated point-proton radius in various theoretical models are converted to the charge radius using Eq. 9.3.

Table 9.3 and Figure 9.6 list the theoretical and experimental values of the charge radius of ${}^6\text{He}$. The two earlier experimental results are from the nuclear collision experiments. As mentioned in Chapter 2, the interpretation of these data requires models to describe the proton and neutron distribution. The value obtained in this work represents the first model-independent determination of the ${}^6\text{He}$ charge radius. It disagrees with the former measurements, and reflects the fact that the model assumptions are inadequate. Most of the cluster models underpredict the radius, and may indicate the necessary modification of the α core inside the ${}^6\text{He}$ nucleus. The Monte Carlo calculation based on AV18+IL2 agrees very well with our result while that using AV18+UIX exceeds the data, but still shows improvement over the result using the two-nucleon potential AV18 alone.

Table 9.3: The ${}^6\text{He}$ nuclear charge radius (in fm) from experimental and theoretical results. Eq. 9.3 is used for the conversion between charge radius and point-proton radius.

Experiments	$\langle r_c^2 \rangle^{1/2}$	$\langle r_{pt}^2 \rangle^{1/2}$	Comments
[Tanihata, 1992]	1.89(4)	1.72(4)	Reaction collision
[Alkhazov, 1997]	2.03(11)	1.88(12)	Elastic scattering
This work, 2004	2.054(14)	1.904(18)	Atomic isotope shift
Theories			
[Csótó, 1993]	1.95(1)	1.793	$\alpha+n+n$, $t+t$
[Funada, 1994]	2.03(1)	1.88	$\alpha+n+n$, AV14 for α -n
[Varga, 1994]	1.96(1)	1.80	$\alpha+n+n$
[Wurzer, 1997]	1.95(1)	1.79	$\alpha+n+n$, $t+t$
[Esbensen, 1997]	2.03(1)	1.88	$\alpha+n+n$, Fermi potential, zero-range n-n
[Navrátil, 2001]	1.92(1)	1.763	No-core shell model + CD-Born
[Pieper, 2001b]	2.06(1)	1.91(1)	AV18+ IL2 three-body potential
	2.12(1)	1.97(1)	AV18 + UIX three-body potential
	2.20(1)	2.06(1)	AV18 two-nucleon potential

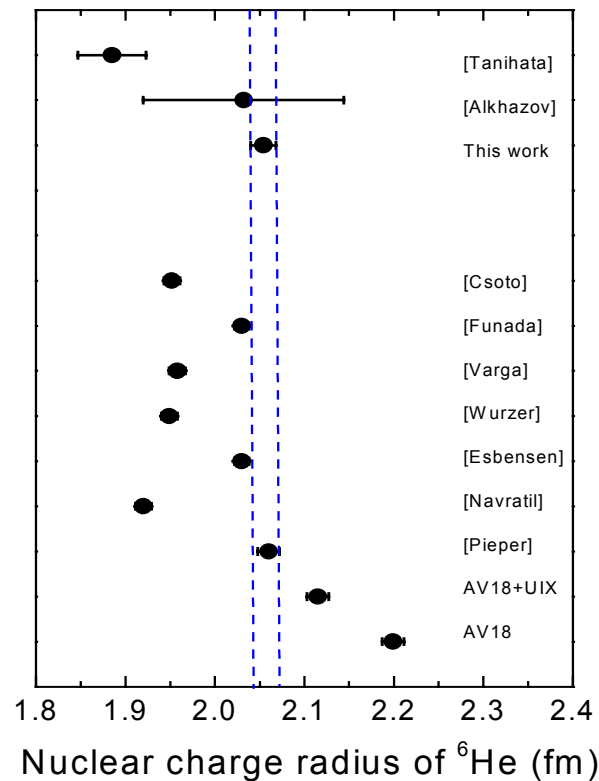


Figure 9.6: Comparison of ${}^6\text{He}$ nuclear charge radius between experiments and theories.

9.5 Darwin-Foldy Correction of the Proton Radius

As shown in Eq. 9.3, the point-proton radius must be derived from the charge radius in order to compare with the theories. One of the required parameters is the rms charge radius of proton, 0.895(18) fm from the electron scattering experiment [Sick, 2003]. However, as pointed out by Friar *et al.* [Friar, 1997b], the interpretation of the proton radius must be carefully addressed. The charge radius is derived from the Sachs form

factor, $\langle r_c^2 \rangle = -6 \frac{dG_E(q^2)}{dq^2} \Big|_{q^2=0}$ as shown in section 2.1. However, due to the recoil

effect, the quantity that affects the scattering cross section is actually

$$\frac{G_E^2(q^2)}{1 + \frac{q^2}{4M_p^2}} \equiv \tilde{G}_E^2(q^2). \quad (9.4)$$

At low q^2 , one may derive $\langle \tilde{r}_c^2 \rangle \equiv -6 \frac{d\tilde{G}_E(q^2)}{dq^2} \Big|_{q^2=0} = \langle r_c^2 \rangle + \frac{3}{4M_p^2}$. (9.5)

The additional term, $\frac{3}{4M_p^2} = 0.0331 \text{ fm}^2$, is called the Darwin-Foldy correction. It is conventionally not considered as part of the proton structure. However, even at $q^2 = 0$, this term does not vanish, and it indicates a more profound physical origin than the recoil effect. This effect was first studied by C.G. Darwin [Darwin, 1928] as a ‘‘Darwin term’’ in the Dirac equation of electrons in the presence of external field. It was also pointed out by Foldy [Foldy, 1958] as the ‘‘Zitterbewegung’’, and is also called Foldy’s ‘‘dancing motion’’. From a quantum mechanical viewpoint, this effect can be thought of as the interference between the particle and anti-particle states. Using the uncertainty principle, the scale where the virtual particles are produced is related to the momentum exchange,

and the energy of the virtual photon should be large enough ($\sim M_p c^2$) to produce the particle and anti-particle pairs:

$$\Delta r \approx \frac{\hbar}{\Delta p} = \frac{\hbar}{(E/c)} \approx \frac{\hbar}{(M_p c^2/c)} = \frac{1}{M_p} \quad \text{and} \quad \langle r^2 \rangle \approx \frac{1}{M_p^2}. \quad (9.6)$$

This is generally called the Darwin-Foldy correction of the proton radius. With the addition of the Darwin-Foldy term, the charge radius of proton is increased from 0.895(18) fm to 0.913(18) fm. This must be taken into account when we derive the point-proton radius of a nucleus from its charge radius. Without the Darwin-Foldy correction of the proton radius, the point-proton radius of ${}^6\text{He}$ is 1.912(18) fm instead of 1.904(18) fm.

Due to the large uncertainty of the measured proton radius, it may be more appropriate to compare the following quantity between the experiments and the theories:

$$\langle r_c^2 \rangle_{\text{He6}} - \langle r_c^2 \rangle_{\text{He4}} = \langle r_{pt}^2 \rangle_{\text{He6}} - \langle r_{pt}^2 \rangle_{\text{He4}} + \langle R_n^2 \rangle. \quad (9.7)$$

First, this eliminates the uncertainty of the proton radius when we make the conversion between charge radius and point-proton radius. Only the charge radius of the neutron is included. The argument in Eq. 9.6 also leads to the *Zitterbewegung* for the neutron. Since the neutron has no net charge, this dancing motion does not contribute directly to the charge radius. However, the motion of the magnetic moment of the neutron does add to the charge distribution due to relativistic effect. In fact, the interpretation of the neutron charge radius has been controversial and is worth noting here. In a spin-1/2 system, the Sachs form factors, $G_E(q^2)$ and $G_M(q^2)$, can be written as a linear combination of two Lorentz invariant form factors, the Dirac form factor $F_1(q^2)$, and the Pauli form factor $F_2(q^2)$. In the case of neutron:

$$G_E^n(q^2) = F_1^n(q^2) - \frac{q^2}{4M_n^2} F_2^n(q^2) \quad \text{and} \quad G_M^n(q^2) = F_1^n(q^2) + F_2^n(q^2). \quad (9.8)$$

The form factors, $F_1^n(q^2)$ and $F_2^n(q^2)$, represent the intrinsic charge and anomalous magnetic moment distribution of the neutron. Using Eq. 2.7, one can immediately write the neutron charge radius as

$$\langle R_n^2 \rangle = -6 \left. \frac{dF_1^n(q^2)}{dq^2} \right|_{q^2=0} + \frac{3}{2M_n^2} F_2^n(0). \quad (9.9)$$

The second term in Eq. 9.9 is called the ‘‘Foldy Term’’, which is from the anomalous magnetic moment of the neutron, and can contribute to the charge radius due to the following reasons. The *Zitterbewegung* of the neutron causes its magnetic moment to oscillate in space. From relativistic electrodynamics, the moving magnetic moment can produce an electric moment. Therefore, the Foldy term is present in the neutron through the large anomalous magnetic moment. Eq. 9.9 can then be written as

$$\langle R_n^2 \rangle = \langle R_n^2 \rangle_{intrinsic} + \langle R_n^2 \rangle_{Foldy}. \quad (9.10)$$

The measured radius, $\langle R_n^2 \rangle = -0.120(5) \text{ fm}^2$, is very close to the value from the Foldy term alone, $\langle R_n^2 \rangle_{Foldy} = -0.1266 \text{ fm}^2$. This leaves very little room for $\langle R_n^2 \rangle_{intrinsic}$.

However, as demonstrated by Bawin and Coon [Bawin, 1999] by incorporating the Dirac and Pauli form factors into the Dirac equation, the Foldy term is cancelled exactly by a contribution from the Dirac form factor, $F_1^n(q^2)$. The same conclusion was made using a relativistic quark model [Isgur, 1999], and it shows the Foldy term is cancelled as long as the total charge of the constituent quarks is zero. Therefore, the measured mean square

neutron charge radius from $\langle R_n^2 \rangle = -6 \left. \frac{dG_E^n(q^2)}{dq^2} \right|_{q^2=0}$ may still represent $\langle R_n^2 \rangle_{intrinsic}$,

and is consistent with the negative pion cloud picture of the neutron. The measured value of the neutron charge radius [Kopecky, 1995, and 1997] is the result of the total charge

operator of the neutron, including all possible effects. Therefore, it can be used directly in Eq. 9.3 and Eq. 9.7 without any correction.

Most cluster models actually use a simplified three-body system to describe the ${}^6\text{He}$ nucleus, and calculate the mean distance between the α core and the two neutrons, which is proportional to this quantity, $\langle r_{pt}^2 \rangle_{\text{He6}} - \langle r_{pt}^2 \rangle_{\text{He4}}$ (see Eq. 9.13). The result is shown in Table 9.4 and Fig 9.7, and it does not change our conclusion made in section 9.4.

Table 9.4: Difference in ms nuclear charge radius between ${}^6\text{He}$ and ${}^4\text{He}$, $\langle r_c^2 \rangle_{\text{He6}} - \langle r_c^2 \rangle_{\text{He4}}$ (in fm^2).

Experiments	
[Tanihata, 1992]	0.18(17)
[Alkhazov, 1997]	1.19(46)
This work, 2004	1.418(58)
Theories	
[Csóto, 1993]	1.115(5)
[Funada, 1994]	1.317(5)
[Varga, 1994]	0.463(5)
[Wurzer, 1997]	1.068(5)
[Esbensen, 1997]	1.313(5)
[Navrátil, 00,01]	0.900(15)
[Pieper, 2001b]	1.426(38)
AV18+UIX	1.687(39)
AV18	1.874(41)

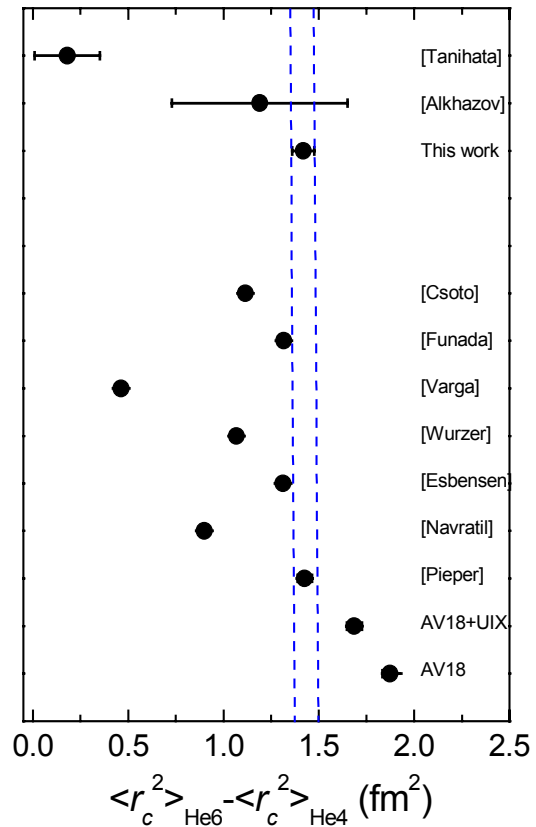


Figure 9.7: The difference in the mean-square charge radius between ${}^6\text{He}$ and ${}^4\text{He}$.

9.6 Neutron-Halo Structure

The point-proton radius of ${}^6\text{He}$ derived from this measurement, 1.904(18) fm, can be compared with the point-nucleon radius (matter radius) obtained from the scattering experiments: 2.33(4) fm [Tanihata, 1992] and 2.30(7) fm [Alkhazov, 1997]. Since the point-nucleon radius includes the distribution from both neutrons and protons, a significant difference between the point-proton and point-nucleon radii directly reveals the neutron-halo structure of the ${}^6\text{He}$ nucleus. The increase of the point-nucleon radius is due to the larger spatial extent of the neutrons. The root-mean-square point-neutron radius can also be derived to be 2.50(5) fm using the following relation:

$$\langle r_n^2 \rangle = [(N+Z)\langle r_m^2 \rangle - Z\langle r_{pt}^2 \rangle]/N = (6\langle r_m^2 \rangle - 2\langle r_{pt}^2 \rangle)/4, \quad (9.11)$$

where N and Z are the numbers of neutrons and protons inside the nucleus respectively, $\langle r_n^2 \rangle$ is the mean-square point-neutron radius, $\langle r_{pt}^2 \rangle$ is the mean-square point-proton radius, and $\langle r_m^2 \rangle$ is the mean-square point-nucleon radius obtained from [Tanihata, 1992] and [Alkhazov, 1997]. Therefore, the difference between the point-neutron and point-proton radii is 0.60(5) fm. This difference was also reported in [Tanihata, 1992] and [Alkhazov, 1997] to be 0.87(6) fm and 0.61(21) fm respectively.

In order to further estimate the thickness of the neutron halo, we can use the simplified description of the ${}^6\text{He}$ nucleus as an α core and two valence neutrons. The mean-square radius of the valence neutrons, $\langle r_n^2 \rangle_v$, can be written as

$$\langle r_n^2 \rangle_v = 2\langle r_n^2 \rangle - \langle r_{pt}^2 \rangle, \quad (9.12)$$

by assuming that the two neutrons in the α core has the same distribution as that of the protons. The thickness of the neutron halo can be defined as the difference between the core radius and the valence-neutron radius, and is about 1.1 fm. The rms distance

between the α core and the center of mass of the valence neutrons, $\langle R^2 \rangle_{\alpha-2n}^{1/2}$ can also be derived using

$$\langle R^2 \rangle_{\alpha-2n} = 9(\langle r_{pt}^2 \rangle_{\text{He6}} - \langle r_{pt}^2 \rangle_{\alpha}). \quad (9.13)$$

If we assume the radius of the α core inside the ${}^6\text{He}$ is the same as that of a free α particle, $\langle r_{pt}^2 \rangle_{\alpha}^{1/2} = 1.45$ fm [Pieper, 2001b], the value is $\langle R^2 \rangle_{\alpha-2n}^{1/2} = 3.70(8)$ fm. The results of the model-independent extraction of the point-proton and point-neutron radii of ${}^6\text{He}$ are summarized in Table 9.5.

Table 9.5: Summary of various parameters for the proton and neutron distribution of the ${}^6\text{He}$ nucleus.

Radius	$\langle r_c^2 \rangle^{1/2}$	$\langle r_{pt}^2 \rangle^{1/2}$	$\langle r_m^2 \rangle^{1/2}$	$\langle r_n^2 \rangle^{1/2}$	$\langle r_n^2 \rangle_v^{1/2}$
Value (fm)	2.054(14)	1.904(18)	2.32(3)	2.50(5)	2.98(8)

9.7 Nuclear-Structure Correction

In addition to the nuclear-size effect, the electromagnetic property of the nucleus may also play a role in the isotope shift. In an atomic bound system, the nucleus “seen” by the electrons is actually different from a free nucleus because the interaction between the electrons and the nucleus may also change the charge and magnetic moment distribution inside the nucleus. As one may expect this effect is directly related to the electric polarizability and the paramagnetic susceptibility of the nucleus in the presence of the EM field produced by the electrons. Another effect is from the virtual-photon exchange, and causes higher-order corrections in the Lamb shift. These effects have been studied in detail in the hydrogen-deuterium isotope shift measurement [Friar, 1997a]. The polarizability of the deuteron is calculated to be $0.6328(17)$ fm³, and the total correction

due to the nuclear polarizability is 18.58(7) kHz in the 1S–2S H–D isotope shift. However, no calculations have been performed for the helium isotopes.

The effect can be estimated by comparison between the 1S–2S transition of H–D and the 2S–3P transition of ^4He – ^6He . The proton and the ^4He nucleus have very small polarizabilities because they are very tightly bound. Then the contribution is mainly from the deuteron and ^6He . The energy shift is negative because the electrons polarize the nucleus, and the induced dipoles provide more attraction. This effect scales approximately in proportion to the total transition frequency. As a result, the effect in the case of ^6He is about 31% of that in deuterium, (121nm/389nm), presuming both have the same polarizability. A more careful evaluation by G.W.F. Drake taking into account the Z^3/n^3 scaling and proper matrix elements gives the ratio of 32.19% [Drake, 2004b]. The total effect on ^4He – ^6He can then be estimated as

$$\delta\nu = 7.08 \text{ kHz} \times \frac{\alpha_E(^6\text{He}) - \alpha_E(^4\text{He})}{\alpha_E(^2\text{H})}, \quad (9.14)$$

where α_E is the electric polarizability, and the contribution from paramagnetic susceptibility is negligible. For deuterium, the contribution from paramagnetic susceptibility is less than 2% of that from electric polarizability [Friar, 1997a].

The electric polarizability can be derived using perturbation theory as

$$\alpha_E = \frac{2\alpha}{3} \sum_{N \neq 0} \frac{|\langle N | \vec{D} | 0 \rangle|^2}{E_N - E_0}, \quad (9.15)$$

where $\vec{D} = e\vec{r}$ is the electric dipole operator, E_N is the energy of the N th excited state $|N\rangle$, and E_0 is the energy of the ground state $|0\rangle$. A calculation by [Esbensen, 2004] gives $\alpha_E = 0.68 - 0.74 \text{ fm}^3$ by summing all the excited states including the continuum in

Eq. 9.15 using a nuclear model of ${}^6\text{He}$. On the other hand, the polarizabilities can also be expressed in terms of the photo-absorption cross section $\sigma_\gamma(\omega)$ known as the Baldin-Lapidus sum rule [Baldin, 1960]:

$$\alpha_E + \beta_M = \frac{1}{2\pi^2} \int_0^\infty \frac{\sigma_\gamma(\omega)}{\omega^2} d\omega, \quad (9.16)$$

where β_M is the paramagnetic susceptibility, and ω is the photon energy. The photo-absorption cross section, $\sigma_\gamma(\omega)$, has been calculated by Bacca *et al.* [Bacca, 2002] using various potential models. From this result of $\sigma_\gamma(\omega)$, the integration of Eq. 9.16 and neglecting β_M gives $\alpha_E({}^6\text{He}) \approx 0.8 \text{ fm}^3$, with the photon energy integrated from the two-neutron separation energy (0.97 MeV) to a cutoff energy of 80 MeV. Although the estimation of α_E depends on the nuclear models of ${}^6\text{He}$, it appears to be a relatively small correction of approximately 10 kHz. If we use a correction of 10 kHz, the value of the ${}^6\text{He}$ charge radius is shifted from 2.054 fm to 2.056 fm (or by 0.1%).

9.8 Meson-Exchange-Current Correction

The final effect is the meson-exchange current (MEC), which contributes to the total charge density, but it is not taken into account by the point-proton distribution of the nucleus. Again, it should be noted that this issue arises only when we try to convert the charge radius to the point-proton radius in order to compare it with the theories, and does not change the measured charge radius. The mesons, *e.g.* π^\pm , mediating the strong forces between the nucleons also carry electric charges. Therefore, the total charge operator must include the pion-exchange effect, and more precisely should also contain the Δ as

well as higher isobar states as indicated in Figure 1.2. Clearly, this effect is model-dependent, and strongly related to the treatment of the meson-exchange nuclear models. In the very precise measurement of the H–D isotope shift, the MEC contribution to the charge radius of deuterium has been investigated. The result is $\langle r_c^2 \rangle_{\text{MEC}} = 0.0135 \text{ fm}^2$ [Kohno, 1983] using the Paris model including π , ρ , and ω exchange, and 0.0159 fm^2 [Friar, 1997b]. This small effect accounts for about 0.2% of the deuterium charge radius or equivalently 20 kHz in the 1S–2S transition frequency. In the case of helium, this effect has not been studied due to its smallness. However, it is expected to be different between ^4He and ^6He because in the case of ^6He , the charged mesons are mediated through a larger distance from the α core to the valence neutrons. Therefore, a correction is needed. Further theoretical studies on this problem are required to compare with the present result.

Chapter 10

Conclusion and Outlook

The charge radius of the neutron-halo nucleus, ${}^6\text{He}$, has been determined to an accuracy of less than 1% by using high-resolution laser spectroscopy. Combined with the matter radius of ${}^6\text{He}$ obtained from the scattering experiments, the neutron-halo structure of ${}^6\text{He}$ is confirmed in a model-independent measurement for the first time. The *ab initio* quantum Monte Carlo calculations have been proved to be successful in describing the system, and have shown the importance of the three-nucleon forces. However, in order to set more stringent constraints on the parameter space of the models, the corrections described in Chapter 9 must be performed to derive the point-proton radius of ${}^6\text{He}$ for comparison. The predictions from the cluster models are all less than the measured value, and this may indicate that the assumption that the α core is unchanged inside the ${}^6\text{He}$ nucleus is inadequate.

The setup and measurement can be improved in the near future to perform a measurement of less than 0.5% by further investigation of the systematic effects. However, in order to compare the result with the theories, a better-determined value of the proton radius is desired. The charge radius of the most neutron-rich ${}^8\text{He}$ nucleus can also be measured by the same technique described in this work. Due to the low production rate and shorter lifetime of ${}^8\text{He}$, the trapping efficiency must be improved to

overcome the additional experimental difficulties. The trap spectroscopy method can also be applied to various short-lived isotopes, and probe the exotic structure of nuclei far from stability.

10.1 Conclusion

The spectroscopy of short-lived ${}^6\text{He}$ atoms was performed, and the charge radius was determined model-independently for the first time. This measurement demonstrates the power of the single atom optical trap technique in precision spectroscopy. The results are

$$\langle r_c^2 \rangle_{\text{He6}} - \langle r_c^2 \rangle_{\text{He4}} = 1.418(58) \text{ fm}^2$$

$$\text{and } \langle r_c^2 \rangle_{\text{He6}}^{1/2} = 2.054(14) \text{ fm}.$$

The point-proton radius of ${}^6\text{He}$ is derived to be 1.904(18) fm without nuclear-medium corrections. The thickness of the neutron halo is estimated to be 1.1 fm by comparing the radii between the protons and the valence neutrons in the ${}^6\text{He}$ nucleus.

In order to compare the theoretical calculations with the measured ${}^6\text{He}$ charge radius, all corrections described in Chapter 9, particularly the meson-exchange-current correction, must be performed. The precision of the experimental test of the theoretical models is limited without these corrections. The comparison with the quantum Monte Carlo results, however, already indicates the importance of the three-nucleon potential, and it confirms the nature that two-nucleon potential alone underbinds the nuclei. For example, the ${}^6\text{He}$ charge radius predicted by the AV18 potential is larger than the measured value by as much as 8% or 9σ .

The cluster models all underpredict the nuclear charge radius of ${}^6\text{He}$. Partly, this can be explained by the larger radius of the α core inside the ${}^6\text{He}$ nucleus than that of a

free α particle. This increase of the α core radius as calculated in [Pieper, 2001b], is approximately 4% from ${}^4\text{He}$ to ${}^6\text{He}$, and 8% to ${}^8\text{He}$. This effect is due to the interaction between the core and the valence neutrons by the long-range attractive force, and might also arise from the charge-exchange process, in which charge can be transferred from the core to the valence neutrons. For this reason, the calculation using cluster models should include the modified radius of the α core, and this increases the calculated ${}^6\text{He}$ charge radius by about 0.04 ~ 0.05 fm. Furthermore, the interaction between the neutron and the α core inside the ${}^6\text{He}$ nucleus may be different from the free n- α interaction. If so, the potential obtained by parameterizing the n- ${}^4\text{He}$ scattering data should not be applied directly in the ${}^6\text{He}$ system. These effects may explain the underprediction of the ${}^6\text{He}$ charge radius by cluster models.

10.2 Outlook

The isotope and optical trap method can also be used to measure the charge radius of ${}^8\text{He}$ ($t_{1/2} = 119$ ms). ${}^8\text{He}$ is the most neutron-rich nucleus and of considerable theoretical interest. The isotope shift between ${}^8\text{He}$ and ${}^4\text{He}$ was calculated by [Drake, 2001] to be

$$\text{IS}(2^3\text{S}_1-3^3\text{P}_2) = 64702.41(7) \text{ MHz} + 1.008(\langle r_c^2 \rangle_{\text{He4}} - \langle r_c^2 \rangle_{\text{He8}}) \text{ MHz/fm}^2. \quad (10.1)$$

The 70 kHz uncertainty of the mass shift is due to the 7 keV uncertainty from the mass determination of the ${}^8\text{He}$ nucleus. On the spectroscopy side, the measurement is identical with the technique we have used for ${}^6\text{He}$ except that the isotope shift is larger (32 GHz in IR), which is too high for both the fast photodiode detector and the frequency counter in our current setup. As a result, the reference laser at 778 nm can then be locked to a different iodine line, which has been mapped and shown in Figure 10.1. The shorter

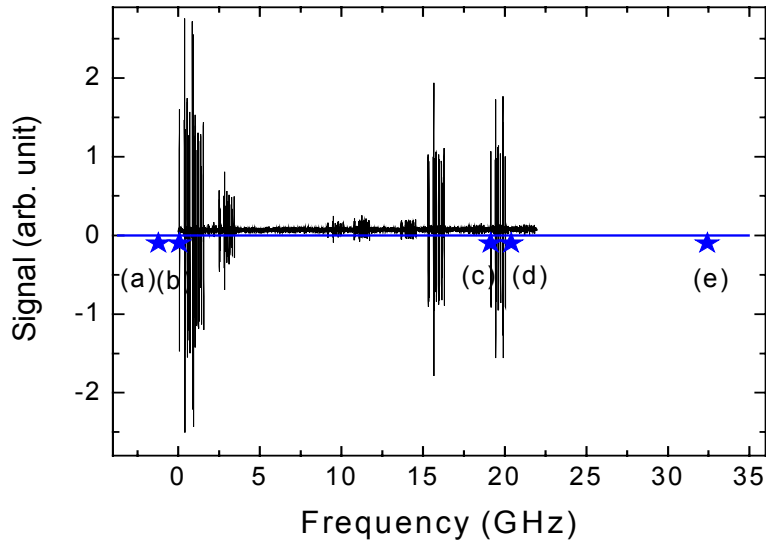


Figure 10.1: The labels (a) and (d) indicate the relative frequency positions for ^4He and ^6He , and (b) is the reference laser position used in the $^{4,6}\text{He}$ IS measurement. (e) is the position for ^8He , and (c) is the proposed position for the $^{4,8}\text{He}$ IS measurement.

lifetime of ^8He also limits the photon statistics. A factor of five more atoms must be collected and measured in order to get the same experimental precision as the ^6He measurement. The reactions for producing ^8He are currently under investigation at ANL. In order to make a 100 kHz measurement, about 500 ^8He atoms are required, and the minimum extraction rate at the discharge source chamber is about $10^5/\text{s}$ in a ten-day run. Therefore, the discharge source and the whole setup must be moved as close to the target as possible to reduce the transport time (currently ~ 1 sec). Other sites capable of producing sufficient ^8He include ISAC at TRIUMF, and ISOLDE at CERN. Both sites have demonstrated a production rate of $10^5/\text{s}$, and are possible facilities for performing the spectroscopic measurement of ^8He in the near future. To increase the trapping efficiency, a technique based on the stimulated emission force can be applied to the

transverse cooling and slowing. This technique is not limited by the photon scattering rate of spontaneous emission, and can exert larger force on atoms [Cashen, 2001].

Due to the unique selectivity and high sensitivity, the laser is a powerful tool to probe the nuclear structure of short-lived isotopes [Otten, 1989]. For example, two-photon spectroscopy for the lithium isotopes at GSI [Ewald, 2004] is aimed to measure the charge radius of the halo nucleus ${}^6\text{Li}$, and collinear laser spectroscopy at ISOLDE measures the possible proton-halo nucleus, ${}^7\text{Li}$ [Geithner, 2002]. Due to modern development of the cooling and trapping of neutral atoms, atom traps are also used for precision measurement, such as parity-nonconservation effects of alkali atoms [Sprouse, 2002], and β - ν angular correlation in nuclear β decays to test Standard Model [Crane, 2001], and [Scielzo, 2004].

Based on the technique of atom trap trace analysis (ATTA), we demonstrated the ultra-sensitive spectroscopic measurement at the single-atom level. This technique has also been applied to rare isotope detection. For example, ${}^{81}\text{Kr}$ (isotopic abundance ~ 1 ppt) was used to date ancient ground water [Sturchio, 2004], and ${}^{41}\text{Ca}$ from biomedical samples (isotopic abundance ~ 1 ppb) can be used to monitor the bone loss rate [Moore, 2004]. These results approach or even exceed the sensitivity of the conventional accelerator mass spectrometry (AMS) while maintaining a compact and low-cost setup. In the future, with the powerful source of short-lived isotopes from the Rare Isotope Accelerator (RIA), ATTA could also provide opportunities for measurements of other rare isotopes far from nuclear stability.

Appendix A

Helium Energy Levels

The valence electrons of the noble gases form a closed shell, so the ground-state noble gas has no electronic spin and orbital angular momentum. When one of the outer electrons is excited, the core no longer has a closed shell, and possesses spin $\frac{1}{2}$. Without the presence of nuclear spin, four angular momenta are coupled. These are the spin (s) and orbital (l) angular momentum of the excited electron and the spin (S) and orbital (L) angular momentum of the core. They couple to form the total angular momentum of the system according to the coupling rule:

$$\begin{aligned}\vec{j} &= \vec{L} + \vec{S} \\ \vec{K} &= \vec{j} + \vec{l} \\ \vec{J} &= \vec{K} + \vec{s}.\end{aligned}$$

The notation of this state is then denoted by $^{2S+1}L_{jnl}[K]_J$, where n is the principle quantum number of the excited electron. Another conventional notation called the Russell-Saunders notation $n^{2S+1}L_J$ can also be used to describe the noble gases, and will be used through this thesis. Here, S is the total spin of the outer electron and the core, instead of the spin of the core alone.

^4He and ^6He nuclei have no nuclear spin, so they do not possess any hyperfine structures. To use the Russell-Saunders notation, we first need to know the vector sum of the spin of the outer electron and the core. The orientation of the spin direction between

the outer electron and the core may be parallel or anti-parallel. Thus it may form a spin-0 (singlet) or a spin-1 (triplet) system. The optical transition of the triplet 2^3S_1 state to the ground state 1^1S_0 is both angular momentum and spin forbidden. As a result, the lifetime of this metastable state can be very long (2.3 hours) without any collisional perturbations. Figure A.1 shows the singlet and triplet states of helium. The energy level of the metastable triplet state 2^3S_1 is 19.82 eV higher than the ground state, and consequently it is difficult to excite with lasers. One way to produce metastable helium is particle bombardment, in which high-energy electrons or atoms collide with the helium atoms, and a small fraction of helium atoms can be excited to the metastable state.

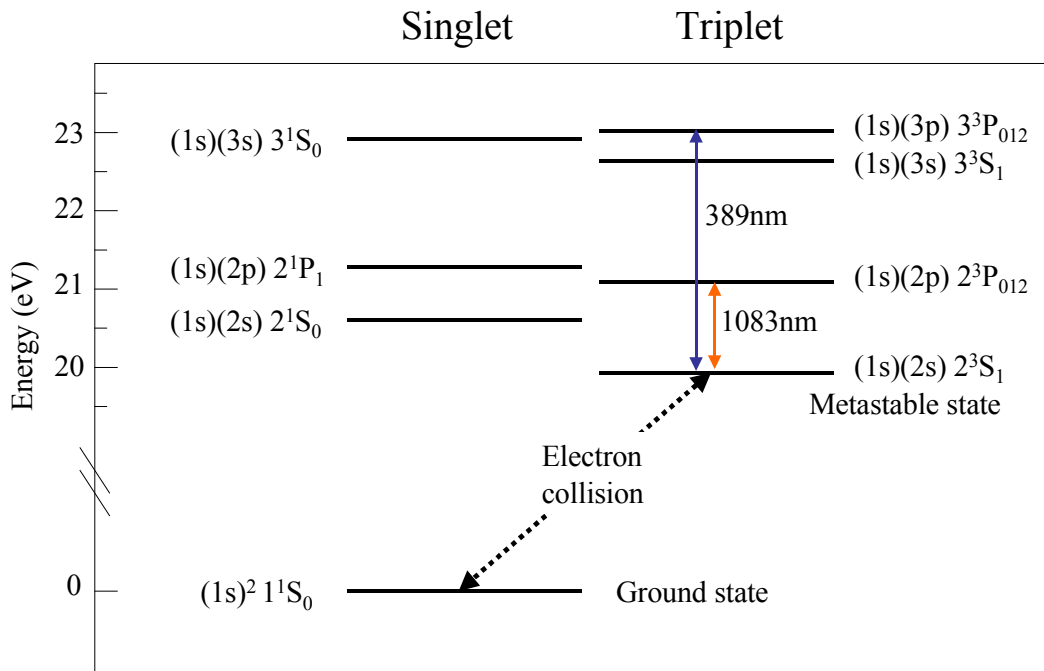


Figure A.1: Energy level diagram of singlet and triplet states of helium.

Appendix B

Laser Cooling and Trapping of Neutral Atoms

B.1 Basic Concepts

In a two-level atomic system interacting with external light field, an atom can be promoted to an excited state by absorbing a photon if the light frequency is tuned to the transition frequency between the two levels. The atom in the excited state will then emit a photon and return to the ground state by two processes. One is stimulated emission, which returns a photon back to the light field in the same direction and at the same frequency as the absorbed photon. Thus no momentum transfer is made during the absorption-emission cycle. Another process is the spontaneous emission, in which the direction of the emitted photon is random and isotropic on average. Therefore, after many absorption-emission cycles, the emitted photons carry no net momentum away, while the absorption process adds momentum into the system $\Delta\vec{p} = N\hbar\vec{k}$, where N is the number of cycles and k is the wave number of the photon. As a result, the spontaneous emission process generates an average force $\vec{F} = \dot{N}\hbar\vec{k} = n_e\Gamma\hbar\vec{k}$, where n_e and Γ are the excited state population and decay rate respectively. By solving the optical Bloch equation, the ground state and excited state populations can be calculated, and the spontaneous radiation force is

$$\vec{F} = \frac{\hbar \vec{k} \Gamma s}{2[1 + s + (2\Delta_L / \Gamma)^2]}, \quad (\text{B.1})$$

where s is the saturation parameter given by $s = I / I_0$, the ratio of laser intensity over the saturation intensity $I_0 = \frac{\pi \hbar c \Gamma}{3 \lambda^3}$, and the laser detuning, Δ_L , is the difference between the laser frequency and the resonance frequency multiplied by 2π . In the case of metastable helium, Γ is $1.02 \times 10^7/\text{s}$ for $2^3\text{S}_1 - 2^3\text{P}_2$ transition at 1083 nm, and a resonant ($\Delta_L = 0$), intense laser light ($s \gg 1$) will decelerate the atomic beam of ^4He by as much as $4.7 \times 10^5 \text{ m/s}^2$. While the atoms are moving, the Doppler effect must be considered. The radiation force becomes velocity-dependent. The non-conservative force can be used for decreasing the velocity space of the atom, and this process is called the Doppler cooling. Moreover, when the atomic transition is not simply between two levels, additional optical pumping will be required for the deceleration process.

The minimum temperature of the atom that can be achieved in the Doppler cooling is called the Doppler limit. In the cooling process, there is actually a heating mechanism taking place, which limits the final achievable temperature. The heating process can be thought of as a fluctuation of the momentum transfer. In momentum space, each spontaneous emission represents a random walk in an arbitrary direction with finite size $\hbar k$. Even if the average momentum reaches zero, the spread of the momentum will be non-zero. The Doppler cooling limit is given by $T_D = \hbar \Gamma / 2k_B$, when the laser detuning $\Delta_L = -\Gamma/2$. For ^4He , $T_D = 39 \mu\text{K}$, which corresponds to a rms velocity $v_D = 0.28 \text{ m/s}$. For a multi-level atomic system, experiments and theories have shown that a temperature below the Doppler cooling limit is possible [Lett, 1988, and Dalibard, 1989].

In addition, with the combination of laser polarization gradient and magnetic field, it is also possible to cool the atoms below the Doppler limit as described in detail by Metcalf and Straten [Metcalf, 1999]. The fundamental lowest laser-cooling limit will then become the single photon recoil, which will cause fluctuation of the atom's momentum. It can be expressed as $T_r = \hbar^2 k^2 / 2Mk_B$, where M is the atomic mass. For ${}^4\text{He}$, $T_r = 4 \mu\text{K}$, which corresponds to a rms velocity $v_r = 0.1 \text{ m/s}$.

B.2 Transverse Cooling

As shown in Eq. B.1, the resonant laser light has a radiation force on atoms, and can be used to deflect and decrease the divergence angle of the atomic beam. Considering two counter-propagating laser beams interacting with an atomic beam perpendicularly, the atom with transverse velocity v will “feel” the force:

$$F(v) = \frac{\hbar k \Gamma s}{2\{1 + s + 4[(\Delta_L - kv) / \Gamma]^2\}} - \frac{\hbar k \Gamma s}{2\{1 + s + 4[(\Delta_L + kv) / \Gamma]^2\}}. \quad (\text{B.2})$$

The velocity dependence of the force comes from the fact that the moving atoms actually have a different resonant frequency due to the Doppler shift. Note that Eq. B.2 is only valid when $s \ll 1$. When the light intensity is too high, one of the laser beam actually changes the ground state and excited state population, and the total force is not a simple linear superposition of the two forces from the two laser beams. When $kv \ll \Delta_L$, this formula can be approximated as

$$F(v) = \frac{8\hbar k^2 s \Delta_L v}{\Gamma [1 + 4(\Delta_L / \Gamma)^2]^2} = -\beta v. \quad (\text{B.3})$$

Since the laser frequency used for transverse cooling is red-detuned ($\Delta_L < 0$), the coefficient β is positive. This corresponds to a damping force proportional to the atom's transverse velocity. This non-conservative viscous force will cool the atoms, and is called optical molasses. The one-dimensional description of the transverse cooling can also be generalized to two dimensions. However, a more complex analysis will be needed because the atom only spends half of its time interacting with the laser beams in each dimension.

B.3 Zeeman Slowing

The radiation force can also be used to decelerate an atomic beam. For a resonant laser light, the maximum deceleration is $\vec{a}_{\max} = \hbar\vec{k}\Gamma/2M$. For finite laser intensity, the deceleration becomes $\vec{a} = (1 + 1/s)(\hbar\vec{k}\Gamma/2M)$, where s is the laser intensity in terms of the saturation intensity, $s = I/I_s$. Therefore, the distance required to decelerate the atoms from initial velocity v_i to final velocity v_f is

$$\Delta z = \frac{v_i^2 - v_f^2}{2a} = \frac{M(v_i^2 - v_f^2)}{\hbar k\Gamma} (1 + 1/s). \quad (\text{B.4})$$

One of the problems in the deceleration of an atomic beam is that the slowing of the atom's velocity also changes the Doppler shift, and the atoms fall out of resonance after a few absorption/emission cycles. One method to solve the problem is the Zeeman slowing technique, in which a spatially changing magnetic field provides the Zeeman shift to compensate the Doppler shift. The condition is

$$\hbar kv(z) = \hbar\Delta_L + \Delta\mu B(z). \quad (\text{B.5})$$

In Eq. B.5, $\Delta\mu$ is the difference of magnetic moment between the upper and lower levels, and can be expressed as $\Delta\mu = (g_e m_e - g_g m_g)\mu_B$, where $g_{e,g}$ is the Lande g-factor of the excited and ground state, $m_{e,g}$ is the magnetic quantum number, and μ_B is the Bohr magneton. For the helium $2^3S_1(m_g = +1)$ to $2^3P_2(m_e = +2)$ transition, $\Delta\mu = +1\mu_B$. So from Eq. B.4 and Eq. B.5, we can derive the required magnetic field:

$$B(z) = B_0 + B_1 \sqrt{1 - z/z_0}, \quad (\text{B.6})$$

$$\text{where } B_0 = \frac{\hbar\Delta_L}{\mu_B}, \quad B_1 = \frac{\hbar k v_i}{\mu_B}, \quad z_0 = \frac{m v_i^2}{\hbar k \Gamma} (1 + 1/s).$$

In practice, the laser intensity has to be slightly larger than the theoretical minimum value to maintain the safety margin for the fluctuation of the deceleration force, which may come from the instability of the laser power or the magnetic field. For the $2^3S_1(m_J = +1)$ to $2^3P_2(m_J = +2)$ transition, a circular polarized σ^+ laser beam is used. During many optical pumping cycles, the atoms are spin-polarized in the $m_J = +1$ ground state, and only make cycling transition between $2^3S_1(m_J = +1)$ and $2^3P_2(m_J = +2)$ states as shown in Figure B.1.

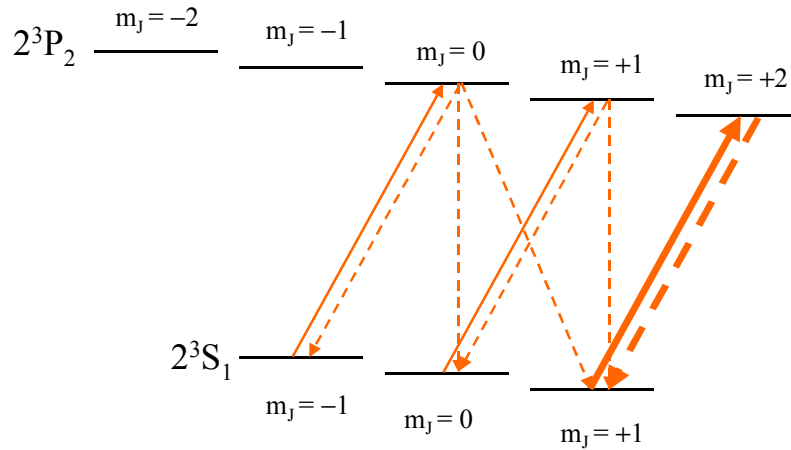


Figure B.1: Optical pumping of the slowing light. The σ^+ light only drives $\Delta m_J = +1$ transitions, while the atoms in excited states can decay to all $\Delta m_J = 0, \pm 1$ states.

B.4 Magneto-Optical Trap

The MOT provides a larger trap depth than magnetic or electric dipole traps, and is widely used to produce large numbers of cold atoms. The working principle is illustrated in Figure B.2 using a simplified two-level system with excited state magnetic sublevels $m_j = 0, \pm 1$. The constant magnetic field gradient near the center shifts the energy level of the excited state linearly proportional to the coordinate. When the atom is at the right side

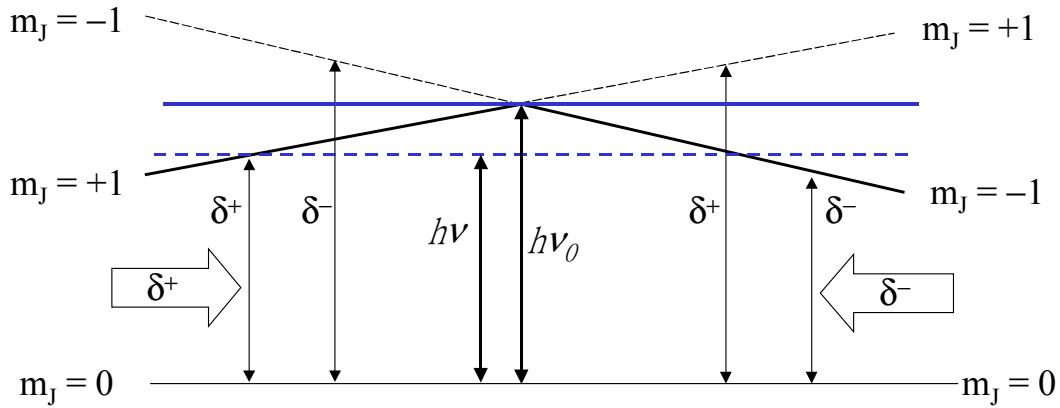


Figure B.2: Energy level diagram in the presence of magnetic field and the laser detuning in the MOT.

of the trap center, it absorbs the σ^- light more effectively than the σ^+ light because the $m_j = -1$ sublevel is lower in energy due to Zeeman shift, and the laser light is red-detuned. The imbalance of the light force from both sides pushes the atom back to the center of the trap, and this position-dependent restoring force forms the trapping potential. In addition to trapping, the MOT can also cool the atoms in velocity space. Considering the effect from both Doppler shift and Zeeman shift, the radiation force of the counter-propagating laser light can be written as

$$F(x, v) = \frac{\hbar k \Gamma s}{2\{1 + s + 4[(\Delta_L - kv - \frac{\mu_B}{\hbar} \frac{\partial B}{\partial x} x) / \Gamma]^2\}} - \frac{\hbar k \Gamma s}{2\{1 + s + 4[(\Delta_L + kv + \frac{\mu_B}{\hbar} \frac{\partial B}{\partial x} x) / \Gamma]^2\}}, \quad (\text{B.7})$$

for atoms with velocity v and position x in a constant magnetic field gradient $\partial B / \partial x$. The large laser detuning will lead to a larger range of the trap potential and larger capture velocity as shown in Figure B.3. However, this will also lead to smaller trapping force due to the far-off resonant laser frequency. In a typical helium MOT, the laser detuning is large ($\sim -10 \Gamma$) to increase the trapping efficiency, and high laser intensity ($\sim 100 I_s$) is used to compensate the reduced force of the far-detuned laser light.

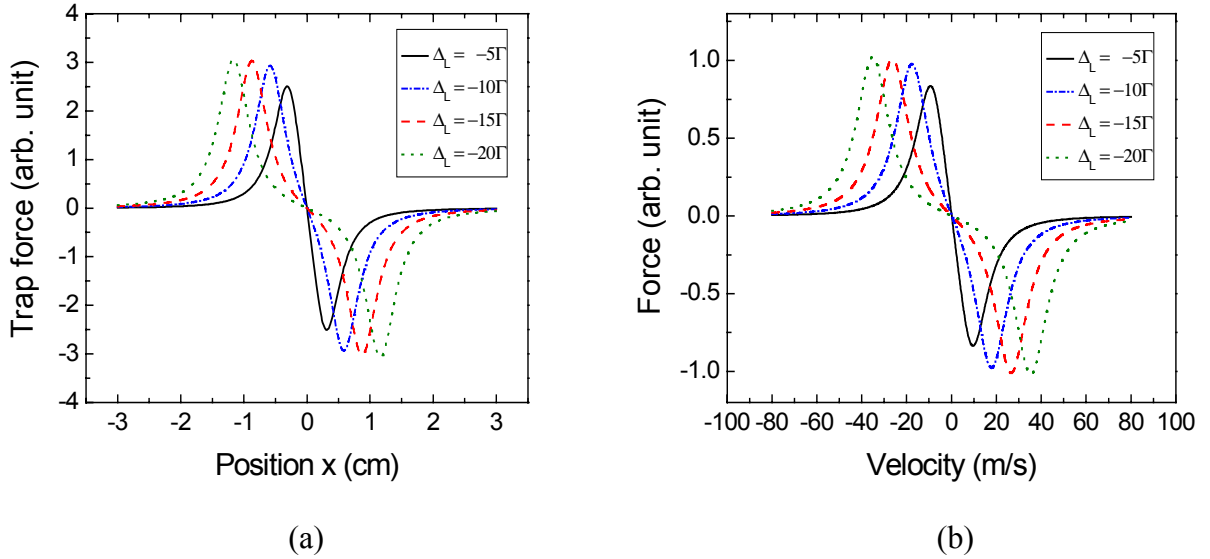


Figure B.3: Position and velocity dependence of the trap force for various values of laser detuning. B field gradient = 20 Gauss/cm, $s = 100$, $v = 0$ in (a), and $x = 0$ in (b).

Appendix C

Frequency Doubling Using a Nonlinear Crystal

A continuous-wave laser source below 500 nm can be generated by frequency doubling using nonlinear crystals. A nonlinear crystal is a material that has nonlinear response in induced polarization to an applied electric field. When the incident light travels into this material, the oscillating electric field may cause the polarization of this material to oscillate at a rate that is twice the incoming light frequency. As a result, the oscillating electric dipoles inside the material can produce “frequency-doubled” radiation. One problem of this process is that the frequency-doubled light usually travels at a different velocity from the original light because of the dispersion of the media. Without a coherent conversion process, the generated second harmonic light will undergo destructive interference because the waves immediately move out of phase. This problem can be solved by a phase matching technique. When the following condition is satisfied, the second harmonic can be generated coherently, and increase the conversion efficiency:

$$V_{\text{fundamental}}^{\perp} = V_{\text{second-harmonic}}^{\parallel} \quad (\text{C.1})$$

where V is the velocity of the light waves inside the crystal. The symbols \perp or \parallel represents the direction of the electric field of the light that is perpendicular or parallel to some specific axis of the crystal. The crystals typically used for second harmonic

generation at near-IR are lithium borate (LBO), beta barium borate (BBO), and lithium iodate (LiIO_3). The comparison for the performance of these crystals can be found in [Bourzeix, 1993]. Here we chose the LBO crystal because it has less sensitivity to the phase matching angle and has a high efficiency. A ring cavity was used to circulate the laser power and to enhance the conversion efficiency. To lock the cavity length to the desired laser frequency, the Pound-Drever-Hall locking technique was used [Drever, 1983]. As shown in Figure C.1, the laser light was phase modulated and a photodiode detected the reflected light of the cavity. The detected signal was demodulated by a RF mixer and served as the error signal to control the PZT voltage and lock the cavity length. Typically, two mW of blue light was produced out of the 300 mW input light at 778 nm.

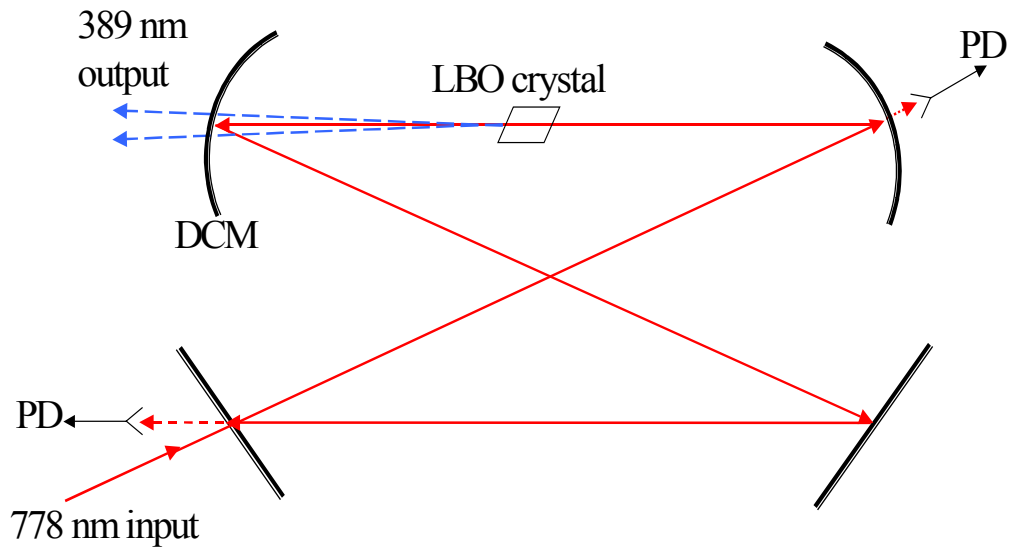


Figure C.1: Geometry of the doubling ring cavity. The crystal is cut at Brewster's angle to minimize the reflection loss. DCM: dichroic curved mirror, which allows the recirculation of the 778 nm light but passes the 389 nm light; PD: photodiode detector.

Appendix D

Frequency-Modulation Spectroscopy

D.1 Basic Concepts

Frequency-modulation (FM) spectroscopy is a very sensitive method to probe weak absorption. It was first investigated by G. C. Bjorklund [Bjorklund, 1980], and has been widely used to detect rare species of atoms and molecules. The basic concept of FM spectroscopy is to modulate the laser light at high frequency ($> \text{MHz}$) so that the typical noise from the laser intensity fluctuation falls off rapidly (the so-called $1/f$ noise). Lock-in techniques can then be used at this high frequency.

The modulation of the laser light can be achieved fairly easily for diode lasers using current modulation or by electro-optical modulators (EOM). When the laser light passes through the EOM crystal driven by an RF field, the phase of the laser light is modulated due to the electro-optical properties of the crystal. The wave function of the light can then be expressed as

$$\begin{aligned} E &= A \cos[\omega t + m \cdot \sin(\omega_{RF} t)] \\ &= A [J_0(m) \cdot \cos(\omega t) + J_1(m) \cos(\omega + \omega_{RF})t + J_1(m) \cos(\omega - \omega_{RF})t] \\ &+ A [J_2(m) \cos(\omega + 2\omega_{RF})t + J_2(m) \cos(\omega - 2\omega_{RF})t] \\ &+ \dots \text{higher - order terms,} \end{aligned} \quad (\text{D.1})$$

where ω is the optical frequency of the laser light, ω_{RF} is the frequency of the applied RF field, J is the Bessel function, and m is the modulation index related to the RF field

strength. We can then find from Eq. D.1 that the output light has three frequency components, ω , $\omega \pm \omega_{RF}$ if high-order contributions are neglected. The carrier and each of the two side bands will produce a beat signal at a frequency of ω_{RF} . When the intensities of the two side bands are equal, the two beat signals cancel perfectly. However, when there is a spectroscopic feature, *e.g.* absorption, the perfect cancellation between the two side bands is destroyed and a frequency component at ω_{RF} is then present in the beat signal. This signal can be sent to a phase-sensitive detector referenced to the same frequency ω_{RF} for demodulation. The spectroscopic feature can be atomic absorption, or reflection of a FPI. Therefore, this method can lock the laser frequency to atomic transitions or the cavity resonance mode.

D.2 Iodine Spectroscopy

An iodine spectrometer was used as the frequency standard at 778 nm in this experiment. FM spectroscopy was used to detect the weak iodine absorption signal. The setup of the saturation spectroscopy using pump-probe configuration is shown in Figure D.1. The probe beam, partial light of DL1 used as the frequency standard, passed the EOM and produced two side bands at ± 15 MHz. Typically the probe beam was 8 mW and the pump beam was 30 mW. Both beams had a diameter of about 2 mm. The pump beam was frequency-shifted by 40 MHz and chopped at 25 kHz by an AOM. The probe beam, which carried the spectroscopic information of the iodine cell, was overlapped with the pump beam and was detected by a fast photodetector. The signal from the fast photodetector was first demodulated by a doubly-balanced mixer referenced to the same RF sources for the EOM at 15 MHz. The IF output of the mixer was then sent to a lock-in

amplifier. The output of the lock-in amplifier was recorded. Figure D.2 shows the dispersive signal when the laser frequency was scanned over a spectroscopic feature. It is worth noting that the relative phase between the local oscillator (LO) and the RF output of the fast photodetector is important for the line shape of the FM saturation absorption signal. When the RF and LO inputs of the mixer are in phase, it probes the absorption feature of the iodine vapor. On the other hand, if the two inputs are out of phase by 90 degree, it probes the dispersion feature of the media. Figure D.2 shows the different line shapes while the relative phase between the RF and LO inputs of the mixer was changed by varying the cable length. Generally, the linewidth of the absorption signal is narrower than the dispersion signal, while the dispersion signal is immune to the Doppler background and the imbalance between the two side bands. The mathematical descriptions of the line shape can be found in [Supplee, 1994].

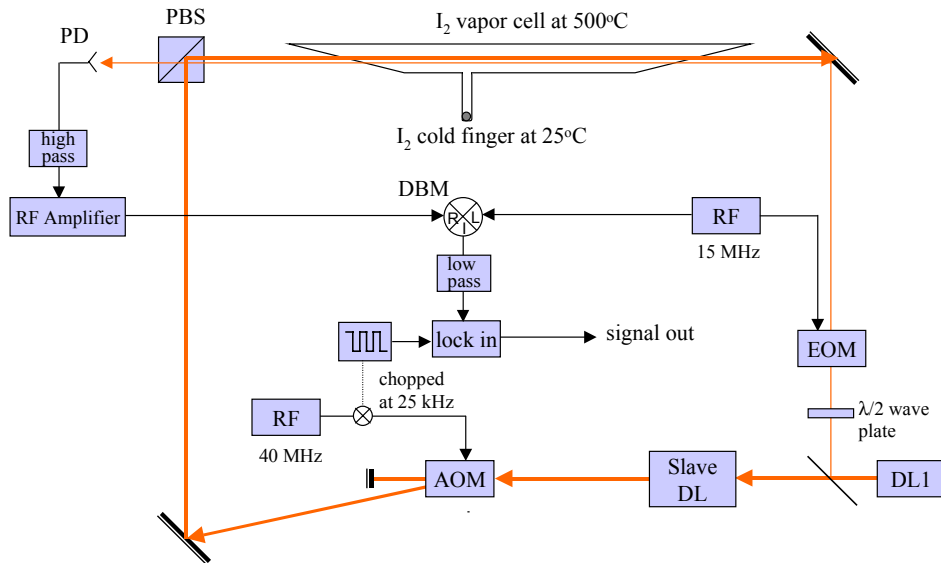


Figure D.1: Schematic diagram of the iodine saturation spectroscopy. PBS: polarizing beam splitter; DBM: doubly-balanced mixer; PD: photodiode detector.

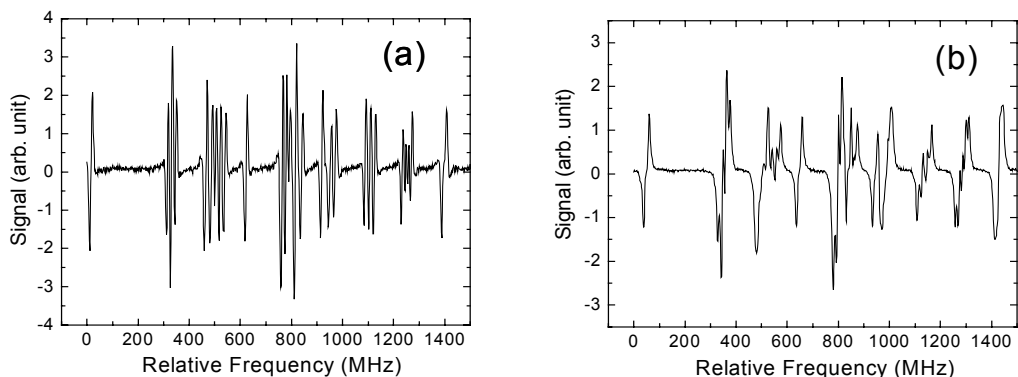


Figure D.2: Line shape of the iodine spectrum. (a) absorption, (b) dispersion.

The absorption signal can then be used to lock the laser frequency or the cavity length. The best signal was achieved by choosing the proper cable length to match the phase between RF and LO, and by putting appropriate laser power into the side bands (typically 30 ~ 40% of the total power). The noise was minimized by careful alignment of the laser polarization along the axis of the EOM to decrease possible amplitude modulation, and by slightly misaligning the direction of the pump beam so that any reflection from the surface of the EOM crystal could not enter the detector. It is important to maintain the proper temperature and pressure of the iodine vapor. A cold finger containing the solid iodine was stabilized at a temperature of about 25°C, which corresponds to a vapor pressure of about 300 mTorr. This is essential for a sub-Doppler spectroscopy. Moreover, because the transition at 778 nm is not from the ground state, the whole glass cell containing the iodine vapor was heated up to 500°C to increase the Boltzmann population of the excited-state molecules.

References

- Adams, C.S., E. Riis, A.I. Ferguson, and W.R.C. Rowley, Precision measurement of the $2^3S \rightarrow 3^3P$ transition in 4He , Phys. Rev. A **45**, R2667-R2670 (1992).
- Ajzenberg-Selove, A., Energy levels of light nuclei $A = 5-10$, Nucl. Phys. A **413**, 1-168 (1984).
- Alkhozov, G.D. *et al.*, Nuclear matter distributions in ^6He and ^8He from small angle p -He scattering in inverse kinematics at intermediate energy, Phys. Rev. Lett. **78**, 2313-2316 (1997).
- Amroun, A., V. Breton, J.-M. Cavedon, B. Frois, D. Goutte, F.P. Juster, Ph. Leconte, J. Martini, Y. Mizuno, X.-H. Phan, S.K. Platchkov, I. Sick, and S. Williamson, ^3H and ^3He electromagnetic form factors, Nucl. Phys. A **579**, 596-626 (1994).
- Audi, G., and A.H. Wapstra, The 1995 update to the atomic mass evaluation, Nucl. Phys. A **595**, 409-480 (1995).
- Bacca, S., M.A. Marchisio, N. Barnea, W. Leidemann, and G. Orlandini, Phys. Rev. Lett. **89**, 052502 (2002).
- Baldin, A.M., Polarizability of nucleons, Nucl. Phys. **18**, 310-317 (1960).
- Bawin, M., and S.A. Coon, Neutron charge radius and the Dirac equation, Phys. Rev. C **60**, 025207 (1999).
- Bjorklund, G.C., Frequency-modulation spectroscopy: a new method for measuring weak absorptions and dispersions, Opt. Lett. **5**, 15-17 (1980).
- Borie, E., and G.A. Rinker, Improved calculation of the muonic-helium Lamb shift, Phys. Rev. A **18**, 324-326 (1978).
- Bourzeix, S., M.D. Plimmer, F. Nez, L. Julien, and F. Biraben, Efficient frequency doubling of a continuous wave titanium:sapphire laser in an external enhancement cavity, Opt. Comm. **99**, 89-94 (1993).
- Bumiller, F.A., F.R. Buskirk, J.N. Dyer, and W.A. Monson, Elastic electron scattering from ^6Li and ^7Li at low momentum transfer, Phys. Rev. C **5**, 391-395 (1972).

- Bushaw, B.A., W. Nörtershäuser, G. Ewald, A. Dax, and G.W.F. Drake, Hyperfine splitting, isotope shift, and level energy of the 3S states of $^{6,7}\text{Li}$, Phys. Rev. Lett. **92**, 043004 (2003).
- Cadman, R.V. *et al.*, Evidence for a three-nucleon-force effect in proton-deuteron elastic scattering, Phys. Rev. Lett. **86**, 967-970 (2001).
- Carboni, G., G. Gorini, G. Torelli, L. Palffy, F. Palmonari, and E. Zavattini, Precise measurement of the $2S_{1/2}-2P_{3/2}$ splitting in the $(\mu^{-4}\text{He})^{+}$ muonic ion, Nucl. Phys. A **278**, 381-386 (1977).
- Carlson, J., Green's function Monte Carlo study of light nuclei, Phys. Rev. C **36**, 2026-2033 (1987).
- Carlson, J., and R. Schiavilla, Structure and dynamics of few-nucleon systems, Rev. Mod. Phys. **70**, 743-841 (1998).
- Cashen, M., O. Rivoire, V. Romanenko, L. Yatsenko, and H. Metcalf, Strong optical forces in frequency-modulated light, Phys. Rev. A **64**, 063411 (2001).
- Castilleja, J., D. Livingston, A. Sanders, and D. Shiner, Precise measurement of the $J=1$ to $J=2$ fine structure interval in the 2^3P state of helium, Phys. Rev. Lett. **84**, 4321-4324 (2000).
- Chen, C.Y., Y.M. Li, K. Bailey, T.P. O'Connor, L. Young and Z.-T. Lu, Ultrasensitive isotope trace analysis with a magneto-optical trap, Science **286**, 1139-1141 (1999).
- Chen, C.Y., K. Bailey, Y.M. Li, T.P. O'Connor, Z.-T. Lu, X. Du, L. Young, and G. Winkler, Beam of metastable krypton atoms extracted from a rf-driven discharge, Rev. Sci. Instr. **72**, 271-271 (2001).
- Coon, S.A., and H.K. Han, Reworking the Tucson-Melbourne three-nucleon potential, Few Body Syst. **30**, 131-141 (2001).
- Crane, S.G, S.J. Brice, A. Goldschmidt, R. Guckert, A. Hime, J.J. Kitten, D.J. Vieira, and X. Zhao, Parity violation observed in the beta decay of magnetically trapped ^{82}Rb atoms, Phys. Rev. Lett. **86**, 2967-2970 (2001).
- Csótó, A., Neutron halo of ^6He in a microscopic model, Phys. Rev. C **48**, 165-171 (1993).
- Dalibard, J., and C. Cohen-Tannoudji, Laser cooling below the Doppler limit by polarization gradients: simple theoretical models, J. Opt. Soc. Am. B **6**, 2023-2045 (1989).
- Darwin, C.G., The wave equations of the electron, Proc. Roy. Soc. (London) A **118**, 654-680 (1928).

- Drake, G.W.F., High precision theory of atomic helium, *Phys. Script.* **T83**, 83-92 (1999).
- Drake, G.W.F., private communication, (2001).
- Drake, G.W.F., Helium. Relativity and QED, *Nucl. Phys. A* **737c**, 25-33 (2004a).
- Drake, G.W.F., private communication, (2004b).
- Drever, R.W.P, J.L. Hall, F.V. Kowalski, J. Hough, G.M. Ford, A.J. Munley, and H. Ward, Laser phase and frequency stabilization using an optical resonator, *Appl. Phys. B* **31**, 97-105 (1983).
- Egelhof, P. *et al.*, Nuclear-matter distributions of halo nuclei from elastic proton scattering in inverse kinematics, *Eur. Phys. J. A* **15**, 27-33 (2002).
- Esbensen, H., G.F. Bertsch, and K.Hencken, Application of contact interactions to Borromean halos, *Phys. Rev. C* **56**, 3054-3062 (1997).
- Esbensen, H., private communication, (2004).
- Ewald, G., W. Nörtershäuser, A. Dax, S. Götze, R. Kirchner, H.-J. Kluge, T. Kühl, R. Sanchez, A. Wojtaszek, B.A. Bushaw, G.W.F. Drake, Z.-C. Yan, and C. Zimmermann, Nuclear charge radius of $^{8,9}\text{Li}$ determined by laser spectroscopy, *Phys. Rev. Lett.* **93**, 113002 (2004).
- Foldy, L., Neutron-electron interaction, *Rev. Mod. Phys.* **30**, 471-481 (1958).
- Friar, J.L., G.L. Payne, V.G.J. Stoks and J.J.de Swart, Triton calculations with the new Nijmegen potentials, *Phys. Lett. B* **311**, 4-8 (1993).
- Friar, J.L., G.L. Payne, High-order nuclear-polarizability corrections in atomic hydrogen, *Phys. Rev. C* **56**, 619-630 (1997a).
- Friar, J.L., J. Martorell, and D.W.L. Sprung, Nuclear sizes and the isotope shift, *Phys. Rev A* **56**, 4579-4586 (1997b).
- Fujita, J., and H. Miyazawa, Pion theory of three-body forces, *Prog. Theo. Phys.* **17**, 360-365 (1957).
- Funada, S., H. Kameyama, and Y. Sakuragi, Halo structure and soft dipole mode of the ^6He nucleus in the $\alpha+n+n$ cluster model, *Nucl. Phys. A* **575**, 93-117 (1994).
- Geithner, R.W., Nuclear moments and differences in mean square charge radii of short-lived neon isotopes by collinear laser spectroscopy, Ph.D. Thesis, <http://cds.cern.ch/>, CERN-THESIS-2002-030 (2002).

- George, M.C., L.D. Lombardi, and E.A. Hessels, Precision microwave measurement of the 2^3P_1 - 2^3P_0 interval in atomic helium: a determination of the fine-structure constant, Phys. Rev. Lett. **87**, 173002 (2001).
- Hauser, P., H.P. von Arb, A. Bianchetti, H. Hofer, F. Kottmann, CH. Lüchinger, R. Schaeren, F. Studer, and J. Unternährer, Search for the $2S$ - $2P$ energy difference in muonic ^4He ions, Phys. Rev. A **46**, 2363-2377 (1992).
- Isgur, N., Interpreting the neutron's electric form factor: rest frame charge distribution or Foldy term?, Phys. Rev. Lett. **83**, 272-275 (1999).
- Huber, A., Th. Udem, B. Gross, J. Reichert, M. Kourogi, K. Pachucki, M. Weitz, and T.W. Hänsch, Hydrogen-deuterium $1S$ - $2S$ isotope shift and the structure of the deuteron, Phys. Rev. Lett. **80**, 468-471 (1998).
- Jung, P., Diffusion of implanted helium in Si and SiO_2 , Nucl. Instr. Meth. Phys. Res. B **91**, 362-365 (1994).
- Kievsky, A., M. Viviani and S. Rosati, Study of bound and scattering states in three-nucleon systems, Nucl. Phys. A **577**, 511-527 (1994).
- King, W.H., Isotope shifts in atomic spectra, Plenum Press, New York, (1984).
- Kohno, M., Mesonic and relativistic corrections to the deuteron charge radius and quadrupole moment, J. Phys. G **9**, L85-L89 (1983).
- Kopecky, S., P. Riehs, J.A. Harvey, and N.W.Hill, New measurement of the charge radius of the neutron, Phys. Rev. Lett. **74**, 2427-2430 (1995).
- Kopecky, S., J.A. Harvey, N.W. Hill, M. Krenn, M. Pernicka, P. Riehs, , and S. Steiner, Neutron charge radius determination from the energy dependence of the neutron transmission of liquid ^{208}Pb and ^{209}Bi , Phys. Rev. C **56**, 2229-2237 (1997).
- Kramer, P.B., and F.M. Pipkin, New measurement of the fine structure in the 3^3P state of ^4He , Phys. Rev. A **18**, 212-223 (1978).
- Lett, P.D., R.N. Watts, C.I. Westbrook, W.D. Phillips, P.L. Gould, and H.J. Metcalf, Observation of atoms laser cooled below the Doppler limit, Phys. Rev. Lett. **61**, 169-171 (1988).
- Lyman, E.M., A.O. Hanson, and M.B. Scott, Scattering of 15.7-Mev electrons by nuclei, Phys. Rev. **84**, 626-634 (1951).
- Machleidt, R., F. Sammarruca, and Y. Song, Nonlocal nature of the nuclear force and its impact on nuclear structure, Phys. Rev. C **53**, R1483-R1487 (1996).

- Mamyrin, B.A., G.S. Anufriev, I.L. Kamenskiy, and I.N. Tolstikhin, Determination of the isotopic composition of atmospheric helium, *Geochem. Int.* **7**, 498-505 (1970).
- Marin, F., F. Minardi, F.S. Pavone, M. Inguscio, and G.W.F. Drake, Hyperfine structure of the 3^3P state of ^3He and isotope shift for the $2^3S-3^3P_0$ transition, *Z. Phys. D* **32**, 285-293 (1995).
- Melnikov, K., and T. van Ritbergen, Three-loop slope of the Dirac form factor and the 1S Lamb shift in hydrogen, *Phys. Rev. Lett.* **84**, 1673-1676 (2000).
- Metcalf, H.J., and P. van der Straten, *Laser cooling and trapping*, Springer, New York, (1999).
- Meyer, H.O., T.J. Whitaker, R.E. Pollock, B. von Przewoski, T. Rinckel, J. Doskow, J. Kuroś-Żolnierczuk, P. Thörngren-Engblom, P.V. Pancella, T. Wise, B. Lorentz, and F. Rathmann, Axial observables in dp breakup and the three-nucleon force, *Phys. Rev. Lett.* **93**, 112502 (2004).
- Minardi, F., G. Bianchini, P. Cancio Pastor, G. Giusfredi, F.S. Pavone, and M. Inguscio, Measurement of the helium $2^3P_0-2^3P_1$ fine structure interval, *Phys. Rev. Lett.* **82**, 1112-1115 (1999).
- Moore, I.D., K. Bailey, J. Greene, Z.-T. Lu, P. Mueller, T.P. O'Connor, Ch. Geppert, K.D.A. Wendt, and L. Young, Counting individual ^{41}Ca atoms with a magneto-optical trap, *Phys. Rev. Lett.* **92**, 153002 (2004).
- Müller, P. *et al.*, Towards measuring the charge radius of ^6He and ^8He , *Nucl. Instr. Meth. Phys. Res. B* **204**, 536-539 (2003).
- Mueller, P., L.-B. Wang, G.W.F. Drake, K. Bailey, Z.-T. Lu, and T.P. O'Connor, Fine structure of the $1s3p^3P_J$ level in atomic ^4He : theory and experiment, Preprint (physics/0407114), (2004).
- Navrátil, P., G.P. Kamuntavičius, and B.R. Barrett, Few-nucleon systems in a translationally invariant harmonic oscillator basis, *Phys. Rev. C* **61**, 044001 (2000).
- Navrátil, P., J.P. Vary, W.E. Ormand, and B.R. Barrett, Six-nucleon spectroscopy from a realistic nonlocal Hamiltonian, *Phys. Rev. Lett.* **87**, 172502 (2001).
- Nogga, A., D. Hüber, H. Kamada and W. Glöckle, Triton binding energies for modern NN forces and the π - π exchange three-nucleon force, *Phys. Lett. B* **409**, 19-25 (1997).
- Otten, E.W., *Investigation of short-lived isotopes by laser spectroscopy*, Harwood, New York, (1989).

- Pieper, S., V.R. Pandharipande, R.B. Wiringa, and J. Carlson, Realistic models of pion-exchange three-nucleon interactions, *Phys. Rev. C* **64**, 014001 (2001a).
- Pieper, S., and R.B. Wiringa, Quantum Monte Carlo calculations of light nuclei, *Annu. Rev. Nucl. Part. Sci.* **51**, 53-90 (2001b).
- Pudlinger, B.S., V.R. Pandharipande, J. Carlson, and R.B. Wiringa, Quantum Monte Carlo calculations of $A \leq 6$ nuclei, *Phys. Rev. Lett.* **74**, 4396-4399 (1995).
- Riisager, K., M.J.G. Borge, H. Gabelmann, P.G. Hansen, L. Johannsen, B. Jonson, W. Kurcewicz, G. Nyman, A. Richter, O. Tengblad, K. Wilhelmsen, and ISOLDE Collaboration, First observation of beta-delayed deuteron emission, *Phys. Lett. B* **235**, 30-33 (1990).
- Robilotta, M.R., and M.P. Isidro Filho, Two-pion exchange three-nucleon potential and D-waves in trinucleon systems, *Nucl. Phys. A* **451**, 581-604 (1986).
- Rosner, S.D., and F.M. Pipkin, Hyperfine structure of the 2^3S_1 state of ^3He , *Phys. Rev. A* **1**, 571-586 (1970).
- Scielzo, N.D., S.J. Freedman, B.K. Fujikawa, and P.A. Vetter, Measurement of the β - ν correlation using magneto-optically trapped ^{21}Na , *Phys. Rev. Lett.* **93**, 102501 (2004).
- Sick, I., Precise nuclear radii from electron scattering, *Phys. Lett. B* **116**, 212-214 (1982).
- Sick, I., and D. Trautmann, On the rms-radius of the deuteron, *Phys. Lett. B* **375**, 16-20 (1996).
- Sick, I., On the rms-radius of the proton, *Phys. Lett. B* **576**, 62-67 (2003).
- Shiner, D., R. Dixon, and V. Vedantham, Three-nucleon charge radius: a precise laser determination using ^3He , *Phys. Rev. Lett.* **74**, 3553-3556 (1995).
- Sprouse, G.D., S. Aubin, E. Gomez, J.S. Grossman, L.A. Orozco, M.R. Pearson, and M. True, Atomic probes of electromagnetic and weak interactions with trapped radioactive atoms, *Eur. Phys. J. A* **13**, 239-242 (2002).
- Stoks, V.G.J., R.A.M. Klomp, C.P.F. Terheggen, and J.J.de Swart, Construction of high-quality NN potential models, *Phys. Rev. C* **49**, 2950-2962 (1994).
- Sturchio, N.C. *et al.*, One million year old groundwater in the Sahara revealed by krypton-81 and chlorine-36, *Geophys. Res. Lett.* **31**(5), L05503 (2004).
- Supplee, J.M., E.A. Whittaker, and W. Lenth, Theoretical description of frequency modulation and wavelength modulation spectroscopy, *Appl. Opt.* **33**, 6294-6302 (1994).

- Tanihata, I., H. Hamagaki, O. Hashimoto, Y. Shinda, N. Yoshikawa, K. Sugimoto, O. Yamakawa, and T. Kobayashi, Measurements of interaction cross sections and nuclear radii in the light p -shell region, Phys. Rev. Lett. **55**, 2676-2679 (1985).
- Tanihata, I., T. Kobayashi, O. Yamakawa, S. Shimoura, K. Ekuni, K. Sugimoto, N. Takahashi, T. Shimoda, and H. Sato, Measurement of interaction cross sections using isotope beams of Be and B and isospin dependence of the nuclear radii, Phys. Lett. B **206**, 592-596 (1988).
- Tanihata, I., D. Hirata, T. Kobayashi, S. Shimoura, K. Sugimoto, and H. Toki, Revelation of thick neutron skins in nuclei, Phys. Lett. B **289**, 261-266 (1992).
- Varga, K., Y. Suzuki, and Y. Ohbayasi, Microscopic multicluster description of the neutron-rich helium isotopes, Phys. Rev. C **50**, 189-195 (1994).
- Wang, L.-B., P. Mueller, R.J. Holt, Z.-T. Lu, T.P. O'Connor, Y. Sano, and N.C. Sturchio, Laser spectroscopic measurement of helium isotope ratios, Geophys. Res. Lett. **30**, 1592-1595 (2003).
- Wang, L.-B., P. Mueller, K. Bailey, G.W.F. Drake, J.P. Greene, D. Henderson, R.J. Holt, R.V.F. Janssens, C.L. Jiang, Z.-T. Lu, T.P. O'Connor, R.C. Pardo, K.E. Rehm, J.P. Schiffer, and X.D. Tang, Laser spectroscopic determination of the ${}^6\text{He}$ nuclear charge radius, Phys. Rev. Lett. **93**, 142501 (2004).
- Wieder, I., and W.E. Lamb Jr., Fine structure of the 2^3P and 3^3P states in helium, Phys. Rev. **107**, 125-134 (1957).
- Wieman, C.E., and L. Hollberg, Using diode lasers for atomic physics, Rev. Sci. Instr. **62**, 1-20 (1991).
- Wiringa, R.B., V.G.J. Stoks, and R. Schiavilla, Accurate nucleon-nucleon potential with charge-independence breaking, Phys. Rev. C **51**, 38-51 (1995).
- Wurzer, J., and H.M. Hofmann, Structure of the helium isotopes ${}^4\text{He}$ - ${}^8\text{He}$, Phys. Rev. C **55**, 688-698 (1997).
- Yan, Z.-C., and G.W.F. Drake, High-precision calculations of the Zeeman effect in the 2^3P_J , 2^1P_1 , 2^3S_1 , and 3^3P_J states of helium, Phys. Rev. A **50**, R1980-R1983 (1994).
- Yang, D.-H., P. McNicholl, and H. Metcalf, Precision measurement of the crossing between the $(J,M)=(0,0)$ and $(1,1)$ sublevels and fine-structure splittings in 3^3P helium, Phys. Rev. A **33**, 1725-1729 (1986).
- Yukawa, H., On the interaction of elementary particles, Proc. Phys. Math. Japan **17**, 48 (1935).

Vita

Li-Bang Wang was born in Tainan, Taiwan, where he attended the Provincial Tainan First High School. After graduation, he studied at National Taiwan University in Taipei, where he was awarded the Dr. Paul C.W. Chu Fellowship for Material Science, and received his B.S. degree in physics. He had served in Taiwan Army as a tank commander, and served as a full-time teaching assistant of the laboratory physics in Taiwan University before starting his doctoral study at the University of Illinois at Urbana-Champaign. In 2000, he was involved in the parity violation experiment to test Standard Model in simple atomic systems. In fall 2001, he began the project of measuring the nuclear charge radius of ${}^6\text{He}$ at Argonne National Laboratory as described in this thesis.

Publications:

- Laser spectroscopic determination of the ${}^6\text{He}$ nuclear charge radius, L.-B. Wang *et al.*, Phys. Rev. Lett. **93**, 142501 (2004).
- Fine structure of the $1s3p\,{}^3P_J$ level in atomic ${}^4\text{He}$: theory and experiment, P. Mueller *et al.*, submitted to Phys. Rev. Lett. (2004).
- Searches for stable strangelets in ordinary matter: overview and a recent example, Z.-T. Lu *et al.*, Nucl. Phys. A, in press (2004).
- Search for anomalously heavy isotopes of helium in the earth's atmosphere, P. Mueller *et al.*, Phys. Rev. Lett. **92**, 022501 (2004).
- Laser spectroscopic measurement of helium isotope ratios, L.-B. Wang *et al.*, Geophys. Res. Lett. **30**, 1592 (2003).
- Towards measuring the charge radius of ${}^6\text{He}$ and ${}^8\text{He}$, P. Mueller *et al.*, Nucl. Instr. Meth. Phys. Res. B **204**, 536 (2003).